# DEVELOPMENT AND APPLICATIONS OF A FLAT TRIANGULAR ELEMENT FOR THIN LAMINATED SHELLS

By
P. Mohan

A DISSERTATION SUBMITTED TO THE FACULTY OF
VIRGINIA POLYTECHNIC INSTITUTE AND STATE UNIVERSITY
IN PARTIAL FULFILLMENT OF THE REQUIREMENTS FOR THE DEGREE OF
DOCTOR OF PHILOSOPHY
IN
AEROSPACE ENGINEERING

Rakesh K. Kapania, Chairman

Raymond H. Plaut

Eric R. Johnson

Efstratios Nikolaidis

Owen Hughes

November, 1997
Blacksburg, Virginia

# DEVELOPMENT AND APPLICATIONS OF A FLAT TRIANGULAR ELEMENT FOR THIN LAMINATED SHELLS

by
P. Mohan
Committee Chair: Rakesh K. Kapania
Aerospace Engineering

## (ABSTRACT)

Finite element analysis of thin laminated shells using a three-noded flat triangular shell element is presented. The flat shell element is obtained by combining the Discrete Kirchhoff Theory (DKT) plate bending element and a membrane element similar to the Allman element, but derived from the Linear Strain Triangular (LST) element. Though this combination has been employed in the literature for linear static analysis of laminated plates, the results presented are not adequate to ascertain that the element would perform well in the case of static and dynamic analysis of general shells. The element is first thoroughly tested for linear static analysis of laminated plates and shells and is extended for free vibration, thermal, and geometrically nonlinear analysis.

The major drawback of the DKT plate bending element is that the transverse displacement is not explicitly defined within the interior of the element. Hence obtaining the consistent mass matrix or the derivatives of the transverse displacement that are required for forming the geometric stiffness matrix is not straight forward. This problem is alleviated by borrowing shape functions from other similar elements or using simple displacement fields. In the present research, free vibration analysis is performed both by using a lumped mass matrix and a so called consistent mass matrix, obtained by borrowing shape functions from an existing element, in order to compare the performance of the two methods. The geometrically nonlinear analysis is performed using an updated Lagrangian formulation employing Green strain and Second Piola-Kirchhoff (PK2) stress measures. A linear displacement field is used for the transverse displacement in order to compute the derivatives of the transverse displacement that are required to compute the geometric stiffness or the initial stress matrix.

Several numerical examples are solved to demonstrate the accuracy of the formulation for both small and large rotation analysis of laminated plates and shells. The results are compared with those available in the existing literature and those obtained using the commercial finite element package ABAQUS and are found to be in good agreement. The element is employed for two main applications involving large flexible structures.

The first application is the control of thermal deformations of a spherical mirror segment, which is a segment of a multi-segmented primary mirror used in a space telescope. The feasibility of controlling the surface distortions of the mirror segment due to arbitrary thermal fields, using discrete and distributed actuators, is studied. This kind of study was required for the design of a multi-segmented primary mirror of a next generation space telescope.

The second application is the analysis of an inflatable structure, being considered by the US Army for housing vehicles and personnel. The tent structure is made up of membranes supported by arches stiffened by internal pressure. The updated Lagrangian formulation of the flat shell element has been developed primarily for the nonlinear analysis of the tent structure, since such a structure is expected to undergo large deformations and rotations under the action of environmental loads like the wind and snow loads. The wind load is modeled as a nonuniform pressure load and the snow load as lumped concentrated loads. Since the direction of the pressure load is assumed to be normal to the current configuration of the structure, it changes as the structure undergoes deformation. This is called the follower action. As a result, the pressure load is a function of the displacements and hence contributes to the tangent stiffness matrix in the case of geometrically nonlinear analysis. The thermal load also contributes to the system tangent stiffness matrix. In the case of the thermal load, this contribution is similar to the initial stress matrix and hence no additional effort is required to compute this contribution. In the case of the pressure load, this contribution (called the pressure stiffness) is in general unsymmetric and its determination is not straightforward, but can be systematically derived from the principle of virtual work. The follower effects of the pressure load have been included in the updated Lagrangian formulation of the flat shell element and have been validated using standard examples in the literature involving deformation-dependent pressure loads. The element can be used to obtain the nonlinear response of the tent structure under wind and snow loads.

# Acknowledgment

I would like to express my deep sense of gratitude to my advisor, Dr. Rakesh K. Kapania for providing me with the technical guidance for the entire period of my research.

I would like to thank Dr. Jakubowski for giving me an opportunity to pursue my research in the area of smart structures.

I would like to thank my committee members, Dr. Plaut, Dr. Johnson, Dr. Nikolaidis and Dr. Hughes, for reading my thesis and giving valuable suggestions.

I would also like to thank Dr. Plaut, Dr. Johnson, Daniel Hammerand and Jing Li for the valuable discussions I had with them during the course of my research.

The support provided for my research by NASA and the Army Reaearch Office, through the grants NAGW-4241 and DAAH04-95-1-0175, is greatly appreciated.

This acknowledgment will not be complete without expressing my gratitude to my parents, without whose support I could not have been successful in all my endeavors.

# Contents

# List of Tables

# List of Figures

# Chapter 1

# Introduction

## 1.1 Background

The two most widely adopted approaches in the finite element analysis of general shells are 1) use of curved elements based on a suitable shell theory and 2) approximation of the curved structure by an assemblage of flat shell elements.

The first application of the finite element method to the analysis of shells consisted of replacing the curved shape with an assemblage of flat elements obtained by combining independent plate bending and membrane formulations. The membrane-bending coupling was brought about as a result of anisotropic material properties and the transformation of the element stiffness matrix evaluated in a local element coordinate system to a global Cartesian coordinate system. This was soon followed by attempts to develop curved elements which give a better approximation to the actual shell curvature. However some difficulties exist in deriving the force-displacement relationships of curved shell elements. Some of the problems associated with the development of curved shell elements are discussed by Meek and Tan [1] and the references therein. These difficulties can be eliminated, at the expense of introducing an approximation to the curved geometry, using an assemblage of flat elements. Intuitively, as the size of the flat subdivision decreases it would seem that convergence to the correct solution should occur, and indeed experience shows that such a convergence can be obtained.

Flat shell elements are more attractive than the curved shell elements as they can be readily built by combining existing plate and membrane elements. The tedious task of computing the element curvatures as required in the case of a curved shell element is completely avoided in a flat shell formulation. The formulation is extremely simple and easy to code. The cost of the stiffness formulation for a flat shell element is expected to be much less than that for a curved shell element. Hence flat shell elements are more suitable for nonlinear analysis, as the stiffness matrix will have to be evaluated and factorized several times during a nonlinear analysis. The choice of the membrane and plate bending elements that are combined to obtain a flat shell element depends on many factors like in-plane rotational singularity, shear locking and spurious zero-energy modes.

In-plane rotational singularity occurs in the case of a flat shell element when the membrane formulation does not include an in-plane rotational degree of freedom or the drilling degree of freedom. The degrees of freedom normally found in a plate bending element are a transverse displacement and out-of-plane rotations. A flat shell element formed by combining a plate bending element and a membrane element which has only in-plane displacements as degrees of freedoms can still exhibit an in-plane rotational degree of freedom at a node in a global Cartesian co-ordinate system. This occurs when all the elements sharing the node are not coplanar and the local coordinate system of the elements does not coincide with the global Cartesian co-ordinate system. This is due to the transformation of the element stiffness matrix computed in a local element co-ordinate system to the global Cartesian co-ordinate system. If all the elements sharing a node are coplanar and the local co-ordinate system of the elements coincides with the global Cartesian co-ordinate system, the absence of in-plane rotational degree of freedom will result in a singular stiffness matrix. This problem can be alleviated by associating a fictitious stiffness to the in-plane rotational degree of freedom of the element, but there is no physical reasoning for the use of such fictitious stiffness.

Shear locking is a phenomenon attributed to the predominance of the transverse shear energy over the bending energy. Due to the presence of a parameter in the transverse shear strain energy that is inversely proportional to the thickness of the element, the transverse shear energy becomes very large compared to the bending energy as the thickness of the element becomes very small and hence results in an overly stiff solution. In other words the bending energy becomes very small or negligible compared to the shear energy, resulting in spurious modes and incorrect results. The shear locking problem can be avoided by completely neglecting the shear strain energy and applying discrete Kirchhoff constraints. This has the effect of relating the shell normal rotations in terms of the transverse displacement and its derivatives (or slopes) at discrete locations (usually at the corner and mid-side nodes) and thus eliminating the shell normal rotations at these locations. In order that the element can be used for both thick and thin shells, a shear stiffness multiplication factor can be used such that a proper balance between the bending and transverse shear energy is maintained in both thick and thin regimes. The shear locking can also be avoided by using a reduced integration scheme to compute the stiffness corresponding to the transverse shear energy, since such a scheme results in a softer element. As mentioned above, the major drawback of using reduced integration is the creation of spurious zero-energy modes which will have to be removed using some stabilization techniques, resulting in a complex formulation.

An element without any of the above mentioned problems is certainly desirable, as these problems have dramatic influence on the correctness of the results, and also the formulation could become complicated due to the additional effort required to alleviate these problems. Membrane and plate bending elements without any of the above mentioned problems have been successfully developed and hence they can be combined to obtain a reliable flat shell element. Due to the extreme simplicity of both the membrane and plate bending formulations and the availability of high speed parallel computers, the element development cost and the computational cost of the analysis are expected to be less than those of curved shell elements, and hence flat shell elements seem to be promising candidates for economic and yet accurate analysis of large structures, especially for nonlinear analysis.

The literature on membrane and plate bending elements is so vast that any attempt to provide a comprehensive review will be futile. Only those elements that are of historic importance and those that have been widely used in the existing literature are discussed in the following sections. Further, the discussion is limited to triangular elements.

## 1.2 Literature Survey

### 1.2.1 Triangular Membrane Elements

The CST (Constant Strain Triangle) and the (LST) Linear Strain Triangle [2] have been predominantly used with suitable plate bending elements. The CST element is the simplest membrane element one could possibly think of. It has three corner nodes with two in-plane displacements per node and the variation of the dispacements within the element is linear. The LST element has three corner and three mid-side nodes with two in-plane displacements per node and the displacements vary quadratically within the element. Though it is well known that the performance of the LST element is superior to that of the CST element, the later has been used in the majority of the flat shell elements that are found in the existing literature, since the nodal degrees of freedom of the CST element can be easily matched with many three node plate bending elements. The drawback of both the CST and the LST elements is the absence of a drilling degree of freedom, and hence they suffer from in-plane rotational singularity as mentioned in the previous section.

The first successful triangular membrane element with drilling degrees of freedom was introduced by Allman [3]. This element, popularly known as the Allman triangle can, be considered as a subset of a more general formulation later proposed by Allman [4]. In this later formulation the in-plane displacements are represented by a cubic polynomial in area coordinates. If the third order terms are dropped, this element reduces to the well known Allman triangle. The latter formulation [4] is not so popular, probably due to the complexity of the interpolation functions. The formulation of the Allman triangle is extremely simple, but it suffers from a peculiar singularity which occurs when all the nodal displacements are zero and the nodal rotations are identical. In most of the problems encountered in structural mechanics, this singularity is automatically removed due to the application of kinematic boundary conditions, unlike complex stabilization schemes that are required to remove the spurious zero energy modes that are created due to the use of reduced order integration.

Cook [5] showed that the Allman triangle can be derived from the LST element using a simple transformation which relates the mid-side displacements in terms of the corner displacements and rotations. Since the stiffness matrix of the LST element is available in many standard textbooks, it is easier to obtain the stiffness matrix of the Allman element from that of the LST element using the transformation of Cook [5] than to obtain the stiffness matrix from the shape functions originally proposed by Allman [3].

Another successful triangular membrane element with vertex rotations was developed by Bergan and Felippa [6] using the free formulation originally suggested by Bergan and Nygard [7]. In the free-formulation, the element stiffness matrix is derived by expressing the requirements of the standard patch test in terms of a set of constraints imposed on the element stiffness matrix, without the need for a variational principle. The patch test is a check which ascertains whether a patch of elements subject to a state of constant strain reproduces exactly the constitutive behavior of the material and results in correct stresses (Zienkiewicz and Taylor [8]). If it does, then the finite element model represents the real material behavior and in the limit, as the size of the elements decreases, would reproduce exactly the behavior of the real structure (Zienkiewicz and Taylor [8]). The patch test was originally proposed in the historic work by Bazeley *et al.* [9], which is discussed in the next section.

Carpenter *et al.* [10] presented a membrane element with degrees of freedom and displacement field identical to that of the Allman triangle [3], but they used a one-point integration scheme to compute the element stiffness matrix. As a result of the reduced order integration, the element exhibits spurious zero energy modes which were removed by Fish and Belytschko [11] using a stabilization scheme. This was done by adding terms to the strain-displacement relations of the one-point integrated Allman element such that the spurious modes were not activated.

Cook [12] presented a more straightforward stabilization scheme, in which two matrices are added to the stiffness matrix of the one-point integrated Allman element. The first, denoted as $[k_1]$, was originally proposed by Zienkiewicz [13] to suppress the in-plane rotational singularity. The second, denoted as $[k_2]$, is derived based on the idea originally proposed by MacNeal and Harder [14]. The physical basis on which these two matrices are derived and how the spurious modes are suppressed by these matrices is not clearly explained in the existing literature. The membrane element stabilized using the two matrices $[k_1]$ and $[k_2]$ was denoted by Cook [12] as T1.

Cook [12] also presented membrane elements obtained by subdividing T1 into 3, 4 and 16 elements denoted as T2, T3 and T4, respectively. He assessed the performance of these four elements for a cantilever beam under in-plane forces. He compared the deflections and stresses obtained from the finite element model with those obtained using beam theory. The finite element mesh used (both regular and irregular) was very coarse with only 8 elements. The elements with subdivisions did not show marked improvement over T1 in the case of the regular mesh, whereas there was some improvement in the case of the irregular mesh. This is not surprising since the aspect ratio of the elements used in the irregular mesh greatly improves when subdivided. The results presented do not show any superiority of the elements T2, T3 and T4, as such an irregular mesh with elements of very poor aspect ratio may not be used if accurate results will have to be obtained. Cook [12] did not compare the performance of the new elements with that of the Allman triangle, especially for finer meshes. He also remarked that the cost of generating the elements with subdivisions is at least 2.5 times that of T1 and expressed concern regarding the computational expense of the elements T2, T3 and T4.

The element T1 might be a better choice than the Allman triangle since it is softer and not computationally very expensive, but a drawback of the stabilization scheme proposed by Cook [12] is the use of arbitrary multiplication factors which are problem dependent. Values for these factors were selected by Cook [12] based on how accurately the displacements at certain nodes were predicted. Such a trial and error process of determining the factors may be very expensive when the problem size is very large and might be less economical than using the Allman triangle [3] with a finer mesh.

Cook [15] presented derivatives of the CST element, obtained by adding supplementary stiffness matrices such that the resulting element has vertex rotations. He presented seven elements named E1 to E7, out of which E3 is the Allman triangle and E7 is the CST element. As in the case of the formulations presented earlier by Cook [12], the new elements required three arbitrary parameters, except of course the elements E3 and E7. The results presented by Cook [15] for a swept panel using a fine mesh do not indicate any marked improvement of performance of the new elements over the Allman triangle (E3). He found that when the element E2 was combined with the well known Discrete Kirchhoff Theory (DKT) plate bending element of Batoz *et al.* [16], for certain values of the parameters, better results were obtained for plane problems whereas very poor results were obtained for many standard shell tests (Scordelis-Lo roof, Pinched cylinder and Hemispherical shell). Cook [15] also found that the elements E1-E6 gave overly stiff results in the case of the hemispherical shell. Cook [15] came to a conclusion that the goal of developing a flat triangular element that works well for both plane and shell problems had not been achieved. This is probably an understatement since successful flat triangular shell elements had been developed by then. A review of flat triangular shell elements is presented later in this Chapter.

The above mentioned membrane formulations are all based on displacement models. Cook [17] presented a plane triangular element with rotational d.o.f., formulated using the assumed-stress hybrid method, which is based on independent prescriptions of stresses within the element and displacements on the element boundary. Membrane elements based on a hybrid formulation have also been presented by Allman [18], Yunus *et al.* [19] and Cazzani and Atluri [20]. Hughes and Brezzi [21] investigated variational principles that permit independent interpolations for the displacement and rotational fields. Membrane elements based on this principle were presented by Ibrahimbegovic [22] and Iura and Atluri [23]. In a three part series, Alvin *et al.* [24], Felippa and Militello [25] and Fellipa and Alexander [26] presented high performance membrane triangular elements with vertex rotations formulated using advanced element construction techniques, namely, Extended Free Formulation (EFF) and Assumed Natural Deviatoric Strain (ANDES) formulation.

Some of the above mentioned membrane elements are known to give more accurate results than the Allman element even for coarse meshes. The same accuracy may be obtained using the Allman element by using a finer mesh without much demand on the computational time due to the simplicity of the formulation. This is probably the main reason for the popularity of the Allman element in spite of the availability of other membrane elements which can outperform the Allman element.

### 1.2.2 Triangular Plate Bending Elements

The choice for a three-noded plate bending element is not as limited as is the case for a three-noded membrane element. Early attempts to develop three-noded plate bending elements with 9 degrees of freedom (transverse displacement and two out-of-plane rotations per node) using interpolation functions in Cartesian coordinates were unsuccessful. For example, combining the terms $x^2y$ and $xy^2$ results in a singular coefficient matrix for some orientations of the element. In addition to this problem, the elements derived using such displacement functions do not satisfy the continuity of the normal slope along inter-element boundaries. This non-conformity was believed to be the stumbling block in the development of triangular plate bending elements until the introduction of the first successful non-conforming element by Bazeley *et al.* [9]. They used the area coordinates instead of the Cartesian coordinates and derived cubic displacement functions in terms of the nodal transverse displacements and normal rotations. The element was non-conforming since the normal slope along the element edges is parabolic, which cannot be uniquely represented by the corner connections. They derived a conforming element by adding certain rational functions to the shape functions developed for the non-conforming element such that normal rotations along the edges now varied linearly, thereby fulfilling the continuity of the normal rotations. The main drawback of this conforming element is the requirement of a 16 point numerical integration scheme.

Bazeley *et al.* [9] found that even for fairly coarse meshes the non-conforming type solution was superior to that of the conforming type solution. They also found that for some mesh configurations the non-conforming element did not show convergence to the exact solution. They came to the conclusion that a necessary and sufficient condition for the convergence of a non-conforming element is that the element should be capable of exhibiting a state of constant strain in the limit as the element size is made infinitesimal. This has evolved into what is called the "patch test", which can be interpreted as a check to ascertain whether a patch of elements subject to a constant strain reproduces exactly the constitutive behavior of the material and results in correct stresses. Though this test would have to be passed when the size of the patch is infinitesimal, the standard practice is to apply the test to a patch of elements of finite size. The patch test is administered in several forms. For details the reader is directed to Ref. [8] and the references therein.

Morley [27] presented a non-conforming triangular element with a quadratically varying displacement field expressed in terms of the corner deflections and the normal slopes at the mid-sides. Morley found that this element gave satisfactory values of bending moments, but gave overly soft values for the deflections even for finer meshes. Several attempts have been made to develop successful conforming and non-conforming triangular elements. Some of them have been summarized by Yang [2], with a brief description of each formulation. A catalog of triangular plate bending elements developed prior to 1984 is given by Hrabok and Hrudey [28].

Batoz *et al.* [16] studied several three-noded triangular plate bending elements with 9 degrees-of-freedom, two rotations and a translation per node. They came to a conclusion that the Discrete Kirchhoff Theory (DKT) element based on the displacement formulation and the Hybrid Stress Model (HSM) element are the most efficient and reliable three-node plate bending elements for the analysis of thin plates.

In the case of the DKT element the shear strain energy is completely neglected, but the formulation proceeds first by assuming that the shear deformations are present and the strain energy is expressed in terms of the normal rotations. Due to the presence of only the first derivatives of the normal rotations in the expression for the strain energy, the shape functions used to describe the normal rotations have to satisfy only the $C^o$ continuity. The normal rotations are first expressed in terms of the nodal values at the corner and mid-side nodes using the standard quadratic shape functions in area coordinates. The normal rotations at the corner and mid-side nodes are then eliminated by applying the discrete Kirchhoff constraints. Though the element is non-conforming, it passes the patch test and hence converges to the exact solution as the mesh is refined.

The HSM element is based on the hybrid stress or mixed method which was used to overcome the difficulties that are encountered in displacement models due to the conformity requirements. The HSM element has a linear distribution of bending moment in the interior, a cubic displacement variation along the edges and a linear normal slope variation along the edges. The nodal degrees of freedom of both the DKT and HSM elements are the same. The DKT element has gained popularity over the HSM element since the formulation of the HSM element is cumbersome, involving more complicated algebraic manipulations. Alternative explicit formulation for the DKT element and the FORTRAN code for computing the stiffness matrix are given by Jeyachandrabose and Kirkhope [29].

Subsequent to the historic work by Batoz *et al.* [16] there has been increased interest in developing more efficient triangular plate bending elements. Jeyachandrabose and Kirkhope [30] constructed an efficient three-noded triangular plate bending element which closely resembles the DKT element presented by Batoz *et al.* [16]. In the DKT formulation of Batoz *et al.* [16] the Kirchhoff hypothesis is introduced only on the corner and mid-side nodes of the element. In the formulation by Jeyachandrabose and Kirkhope [30] the Kirchhoff hypothesis is also introduced at the centroid of the element. This required an approximation for the normal rotations using seven shape functions. Since the transverse displacement $w$ is not uniquely defined in the interior of the element proposed by Jeyachandrabose and Kirkhope [30], as is the case with the DKT element [16], calculation of the derivatives of $w$ at the centroid is carried out by borrowing shape functions from existing elements. In order to soften the element, two different smoothing techniques are used, giving two new elements. FORTRAN listings are also given by Jeyachandrabose and Kirkhope [30] for computing the element stiffness matrices.

Tessler and Hughes [31] presented a three-noded non-conforming shear deformable element called MIN3, based on the Reissner-Mindlin theory. In the formulation of the MIN3 element the transverse displacements are expressed in terms of the standard quadratic basis in area coordinates. The shell normal rotations are assumed to vary linearly over the element. The transverse displacements at the mid-side nodes are eliminated by imposing a constraint that the shear strain is continuous along the element edges. This kind of anisoparametric interpolation and the use of a suitable shear correction factor results in an element which has the correct rank and does not suffer from shear locking even when full numerical integration is used. The element is applicable for both thick and thin plates.

Meek and Tan [32] presented a discrete Kirchhoff triangular element with loof nodes (6 Gauss points, 2 on each side). In their plate bending element the transverse displacement is expressed in terms of the standard quadratic basis in area coordinates using the corner and mid-side nodal values. The rotations of the shell normal $\beta_x$ and $\beta_y$ about a local Cartesian coordinates $y$ and $x$, respectively, are interpolated in terms of the values at the loof nodes. However, the normal rotations are not expressed using the standard quadratic basis in area coordinates, due to the existence of a linear combination of the basis called the neutral function which is zero at all the loof nodes. The existence of such neutral functions in rectangular elements had been observed by Gopalacharyulu [33] and Irons [34] and they suggested that the singularity can be eliminated by expanding the basis by adding an extra node. For a rectangular element with loof nodes, Irons [34] suggested that the centroid be used as the extra node and also presented an expanded basis. Meek and Tan [32] used an expanded basis by adding a cubic term to the standard quadratic basis in area coordinates. They also chose the centroid as the additional node. The normal rotations $(\beta_x, \beta_y)$ at the loof nodes and the centroid are eliminated in terms of the rotations of the shell normal about the edges at the loof nodes by imposing Kirchhoff assumptions at discrete points. Due to the presence of fourth order terms, a seven point Gauss quadrature rule is required to numerically integrate the element stiffness matrix of their element. As a result, nonlinear analysis of large structures using their element might be computationally very expensive. Though their element passes the patch test, it was found to exhibit good convergence only in the case of uniformly distributed loads and poor performance under concentrated loads.

Dhatt *et al.* [35] presented a six node discrete Kirchhoff element called DKTP whose formulation is similar to that of the well known DKT element. Though the interpolations used for the transverse displacement and the normal rotations in the DKTP element are one order higher than those used in the DKT element, the accuracy of the DKTP element was found to be of the same order as that of the DKT element. Dhatt *et al* [35] have mentioned that this is because in both formulations the rotation of the normal to the undeformed mid-surface of the element about the element edges is assumed to vary linearly along the edges.

Felippa and Bergan [36] presented a triangular plate bending element based on the free formulation. They modified the cubic terms of the nine term polynomial in area coordinates given by Bazeley *et al.* [9] so that the resulting element passes the patch test. Since the free formulation is based on the underlining principles of the patch test, elements derived using this principle are guaranteed to pass the patch test and do not have to undergo the patch test. Specht [37] presented another modified version of the basis first used by Bazeley *et al.* [9] by imposing the condition that the integrated jumps of the displacement and its normal derivative along the element boundaries is zero. This is also called the interpolation test for plate bending problems. The modified version has fourth order terms in place of the cubic terms given by Bazeley *et al.* [9]. These shape functions in explicit form are given by Zienkiewicz and Taylor [8] and hence can be readily incorporated into a computer code.

### 1.2.3 Flat Triangular Shell Elements

No one particular plate bending or membrane element has been claimed to be the best for the analysis of general shells. The CST, LST, Allman triangle, DKT, MIN3 and the Morley's triangle have been widely used in the flat shell formulations that are available in the existing literature. Flat shell elements based on mixed formulations and other unconventional methods like the natural mode method and free-formulation have also been successfully developed. The majority of the flat shell formulations available in the literature have been developed primarily for non-linear analysis since a non-linear analysis using flat shell elements is expected to be more economical than that using curved shell elements. The updated Lagrangian formulation (ULF) has been predominantly used in the non-linear flat shell formulations available in the existing literature.

In an updated Lagrangian formulation all the variables are referred to a known configuration, the reference configuration, which is continuously updated during the solution process. During the deformation process a large portion of the total deformation of the structure is made up of rigid body motions. If the rigid body modes are removed from the total displacements, the resulting deformational translations and rotations are very small and hence a linearized incremental formulation [39] can be used. In a linearized incremental formulation the stresses are computed using linear strain-displacement relations. The tangent stiffness matrix contains only the linear stiffness matrix and the initial stress matrix. The stiffness matrices resulting from the nonlinear terms in the strain-displacement relations are neglected, resulting in a very economical analysis. If the rigid body modes are not removed all nonlinear terms in the strain displacement relations will have to be considered for computing the stresses and the tangent stiffness matrix.

A three node flat triangular shell element was introduced by Argyris *et al.* [40] for nonlinear elastic stability problems. This formulation, denoted as the "natural mode technique", is based on decomposing the displacements into rigid body and straining modes, which are naturally exhibited by any structure undergoing deformation.

Horrigmoe and Bergan [41] presented flat triangular and quadrilateral shell elements based on a hybrid stress model for static analysis of isotropic plates and shells. They employed a linearized updated Lagrangian formulation in which the rigid body modes are removed from the total displacements. The initial stress matrix was obtained using a lower order interpolation than that used for the linear stiffness matrix.

Chen [42] presented a three node flat triangular shell element obtained by combining CST and Morley's plate bending element for elasto-plastic analysis of isotropic plates and shells. Chen used the Von Karman theory of large deflection and adopted the Lagrangian description to describe the deformation of the element. Chen presented numerical examples that involved only small rotations. Peric and Owen [43] presented a thin shell formulation identical to that of Chen [42] for elasto-plastic analysis of isotropic plates and shells, but presented numerical examples involving large rotations.

Bathe and Ho [44] presented a three node flat triangular shell element for static analysis of isotropic plates and shells by combining the DKT [16] and CST elements. They used a linearized updated Lagrangian formulation in which the undeformed coordinates are used to obtain the strain-displacement matrices for all times. The membrane stresses and internal forces are computed from total displacements as was done by Horrigmoe and Bergen [41], whereas the curvatures and the bending moments are computed from incremental displacements and updated at the end of each increment. Bathe and Ho also used a linear displacement field to compute the initial stress matrix. Due to the use of a linearized incremental formulation without removing the rigid body rotations from the total or incremental displacements, their formulation is restricted to small incremental rotations.

The above mentioned restriction in the formulation of Bathe and Ho [44] was overcome by Hsiao [45] by removing the rigid body modes from the total displacements, in two stages. In the first stage the undeformed element is rotated to an intermediate position by applying an out-of-plane rotation about a fixed axis. The element is transformed to its final configuration by applying an in-plane rotation to the intermediate configuration. Both the membrane and bending internal force vectors and the membrane stresses are obtained from the total deformational translations and rotations.

Peng and Crisfield [46] also presented a three node flat triangular shell element identical to that of Chen [42] , but they removed the rigid body modes from the total displacements using a procedure similar to that used by Hsiao [45], thereby enabling the use of very large load increments.

Meek and Tan [47] presented a flat triangular shell element for static analysis of isotropic plates and shells by combining the LST element and the discrete Kirchhoff plate bending element with loof nodes [32]. Due to the presence of fourth order terms in the plate bending formulation, a seven point Gauss quadrature rule is required to numerically integrate the element stiffness matrix of their element. As a result, nonlinear analysis of large structures using their element might be computationally very expensive.

Recently Poulsen and Damkilde [48] presented a flat triangular shell element by combining the LST element and a plate bending element with loof nodes similar to that of Meek and Tan [32]. The two major differences between the plate bending elements of Meek and Tan [32] and Poulsen and Damkilde [48] are 1) the seventh term in the expanded basis used by Meek and Tan [32] is unsymmetric in area coordinates, whereas that used by Poulsen and Damkilde [48] preserves symmetry, 2) the basis used by Poulsen and Damkilde [48] to express the transverse displacement has a term $\xi_1\xi_2\xi_3$ in area coordinates called the bubble function, in addition to the standard quadratic basis, with the centroid as the additional node. Such a basis was expected to give better load distribution and improved results for nonlinear analysis. The final degrees of freedom are the same in both the formulations and the condensation was done by Poulsen and Damkilde [48] as was done by Meek and Tan [32]. Both Meek and Tan [47] and Poulsen and Damkilde [48] have not presented any shell problems involving large rotations to demonstrate the performance of the formulation for such problems.

Fafard *et al.* [49] presented a six node flat triangular shell element called DLTP for static analysis of isotropic plates and shells. Their flat shell element is obtained by combining the six node discrete Kirchhoff theory plate bending element (DKTP) of Dhatt *et al.* [35]

and the well known LST element. Fafard *et al.* [49] presented two updated Lagrangian formulations. The first, termed ULF1, is a total Lagrangian formulation within each step, with the configuration at the beginning of the step taken as the reference configuration for the next step. The second, termed ULF2, is a fully updated Lagrangian formulation with the estimated configuration at the end of each iteration taken as the reference configuration for the next iteration. In ULF1, all nonlinearities are considered in the computation of stresses and the tangent stiffness matrix. In ULF2 a linearized incremental formulation is used but the stresses are computed using nonlinear strain-displacement relations as in ULF1. Fafard *et al.* [49] studied the importance of using lower order interpolations for the transverse displacement ($w$) to compute the nonlinear terms in the Green-Lagrange strains and the initial stress matrix. They found that a linear interpolation for $w$ is preferable with DLTP and that the DCT element (combination of the DKT and CST elements), which gives an over stiff solution when a cubic interpolation is used for $w$, could be made softer by using a linear interpolation for $w$. Fafard *et al.* [49] also found that in the case of ULF2 the solution failed to converge when very large initial increments were used.

The majority of the flat shell elements mentioned above use either the CST or the LST elements to represent the membrane action. Hence those flat shell elements suffer from in-plane rotational singularity. Though the singularity can be removed by associating a fictitious stiffness with the in-plane rotational degree of freedom, the presence of drilling degrees of freedom is considered essential for the analysis of shells, and elements with such drilling degrees of freedom have been found to exhibit improved membrane response and also a reduced sensitivity to element distortion [50].

Madenci and Barut [51] presented a flat shell element for static analysis of composite structures, obtained by combining the flat triangular membrane and bending elements developed by Bergan and Felippa [6] and Felippa and Bergan [36], respectively, which are based on the free-formulation originally suggested by Bergan and Nygard [7]. Madenci and Barut [51] employed an updated Lagrangian formulation in which the rigid body modes are removed using the procedure given by Hsiao [45]. The presence of in-plane rotational degrees of freedom in the formulation of Madenci and Barut [51] eliminates the in-plane rotational singularity.

Oral and Barut [52] presented a shear-flexible flat shell element for large deflection and instability analysis of isotropic plates and shells by combining the Allman triangular element and the MIN3 plate bending element of Tessler and Hughes [31]. They employed an updated Lagrangian formulation in which the rigid body modes are removed from the total displacements using the procedure given by Hsiao [45].

In all the above mentioned flat shell elements except that of Bathe and Ho [44], Fafard *et al*. [49], Meek and Tan [47] and Poulsen and Damkilde [48], large rotations are handled by removing the rigid body modes from the total or incremental displacements. Several large rotation formulations based on isoparametric elements and a total Lagrangian formulation have been presented, in which the large rotations of the shell director are described by using the large rotation matrix parametrized by 3 rotation components (see Simo and Fox [53], Parisch [54], Ibrahimbegovic [55] for details) or by using nonlinear trigonometric functions parametrized by 2 rotation components (see Surana [56], Brank [57] for details).

Onate *et al*. [58] presented a triangular flat shell element for geometrically nonlinear analysis of isotropic shells. Their flat shell element is a combination of the LST element and a plate bending element (based on Reissner-Mindlin theory) with linear interpolation for the transverse displacement using corner nodes, and linear interpolation for the normal rotations and transverse shear strains using mid-side nodes. Their formulation is applicable for both thick and thin shell regimes. Onate *et al*. [58] have mentioned that their nonlinear formulation is based on Simo's shell theory. No details regarding the formulation as applied to the flat shell element are presented by Onate *et al*. [58] nor have they presented any examples involving large rotations to demonstrate the accuracy of the formulation.

The formulation of the flat shell element STRI3 of the commercial finite element package ABAQUS (combination of DKT and CST elements) is also based on a description of the motion of the shell director using the large rotation matrix (parametrized by 2 rotation components). Not much information is available in the existing literature regarding the formulation or the accuracy of the STRI3 element either for problems involving very large rotations.

## 1.3 Objective and Scope of Present Research

The primary aim of the present research is to develop an inexpensive thin shell element for two main applications involving thin large flexible structures : 1) control of thermal deformations of a spherical mirror segment used in an astronomical telescope and 2) analysis of large inflatable structures.

Flat shell elements are chosen for the analysis due to the advantages mentioned in section 1.1. A triangular element is an obvious choice since it can be used to model arbitrary geometries. Further triangular elements with only corner connections are desired, as data preparation becomes tedious in the case of an element with nodes at the mid-sides and interior. The flat shell element used in the present research is a combination of the DKT plate bending element of Batoz *et al.* [16] and a membrane element similar to the Allman element [3], but derived from the LST element using the transformation given by Cook [5]. A membrane element similar to the Allman element is chosen as it does not suffer from in-plane rotational singularity and has better membrane response than the CST element which has been predominantly used in the flat shell formulation available in the existing literature. The DKT element is chosen as it has been well established as an efficient and reliable thin plate bending element.

Carpenter *el al.* [10] combined the one-point integrated Allman element and the DKT plate bending element for linear analysis of isotropic shells. This underintegrated element gave better results compared to the fully integrated element, but the reduced order integration resulted in spurious zero energy modes. They claim that these spurious zero energy modes are of little consequence in most practical applications and far less troublesome than the in-plane rotational singularity. It is not well known under what circumstances the existence of spurious mode could be troublesome. Hence such elements may not always be reliable.

Fish and Belytschko [11] combined the stabilized, one-point integrated Allman element and the DKT plate bending element for linear static and buckling analysis of isotropic shells. They found that in the case of linear static analysis of the hemispherical shell the underintegrated element gave better results than the fully integrated element even for coarse meshes. They have shown results only up to a mesh of 128 elements which may not be sufficient enough to accurately model a hemispherical shell. The trend of the results presented by Fish and Belytschko [11] for linear static analysis shows that the element would over predict the results for finer meshes or in other words the underintegrated element is too soft. They have not fully established the convergence characteristics of the element. In the case of buckling analysis the derivatives of the transverse displacement that are required for computing the geometric stiffness matrix were obtained by integrating the curvature field.

In an attempt to soften the element, Fish and Belytschko [11] also employed a ont-point integration scheme to compute the geometric stiffness matrix. Nothing can be concluded regarding performance of such a geometric stiffness matrix in the case of nonlinear response of general shells, as they have presented results only for linear buckling analysis.

Chen [59] combined the DKT plate bending element and the membrane element of Allman [4] with cubic interpolation functions for the in-plane displacement fields, for linear analysis of isotropic shells. A 6-point integration scheme is required [59] to evaluate the stiffness matrix of the cubic membrane element of Allmanm [4]. In an attempt to improve the performance of the element, Chen [59] used a reduced order (four-point) scheme. Chen [59] compared the performance of the 4-point and 6-point integrated element with that of the CST element (in combination with the DKT plate bending element), for the Scordelis-Lo roof, pinched cylinder and the hemispherical shell problems. The 4-point integrated element showed rapid convergence compared to that of the 6-point integrated element and the CST element in the case of the Scordelis-Lo roof. In the case of the pinched cylinder the 4-point integrated element did not show any improvement over the 6-point integrated element and both gave over soft results. In the case of the hemispherical shell, the performance of the 4-point integrated element was superior to that of the 6-point integrated element, but the convergence was not as rapid as in the case of the CST element. Better performance of the CST element in the case of the hemispherical shell has also been noticed by Cook [15] and Carpenter *el al.* [10]. The reason for such superior performance of the CST element in the case of the hemispherical shell alone is not known.

Ertas *et al.* [60] presented a three-noded triangular flat shell element, termed AT/DKT, which is a combination of the DKT plate bending element and a membrane element similar to the Allman triangular element, but obtained from the LST element by applying the transformation given by Cook [5]. They compared the performance of the AT/DKT element for static analysis of anisotropic cantilever plates to that of the STRI3 element of ABAQUS. The results presented are all related to static analysis of flat plates. The results of AT/DKT and STRI3 presented by Ertas *et al.* [60] do not show excellent agreement and also have some sign errors. They are not sufficient to ascertain that the element would converge towards exact solutions in the case of static and dynamic response of composite shells.

In the present research, the flat shell element presented by Ertas *et al.* [60] is first rigorously tested for linear static response analysis of laminated plates and shells to verify its accuracy and determine the convergence characteristics, and is extended for free vibration, linear thermal/piezoelectric and geometrically nonlinear analysis which include snap-back, snap-through, thermal post buckling, dynamic buckling and the follower effects of the pressure loads (Kapania and Mohan [61], Mohan and Kapania [62], Mohan and Kapania [63]).

The major drawback of the DKT element is that the transverse displacement field is not explicitly defined in the interior of the element. Hence a consistent mass matrix and the derivatives of the transverse displacement that are required to obtain the geometric stiffness matrix (initial stress matrix) in the case of buckling and postbuckling analysis cannot be readily obtained. Free vibration analysis could be performed using a lumped mass matrix, but the analysis is expensive, especially if a large number of modes is required to be extracted, due to poor rate of convergence. In the present research, free vibration analysis is performed using both a lumped mass matrix and a so called consistent mass matrix, in order to compare the two methods. The consistent mass matrix is obtained using the nine term polynomial in area coordinates given by Specht [37] to represent the transverse displacement and the standard quadratic basis in area coordinates for the in-plane displacements. Unlike the lumped mass matrix, the rotary inertias are included in the consistent mass matrix.

In the case of thermal analysis the temperature variation along the thickness of the element and across the plane of the element is assumed to vary linearly in terms of the nodal temperatures. The formulation can be applied for the analysis of structures excited by an electric field by replacing the coefficients of thermal expansion by the electric field constants and the thermal field by the electric field, assuming a linear relation exists between the induced strain and the applied electric field in terms of the electric field constants. A structure with any number of actuators bonded or embedded in a substrate can be analyzed provided the overall thickness of the structure is small enough to neglect the shear deformations. The electro-thermo-mechanical coupling has not been included in formulation, but can be easily incorporated as most of the strain-displacement matrices required are already available.

The updated Lagrangian formulation employed in the present study is based on Green-Lagrange strain measures and PK2 (Second Piola-Kirchhoff) stress measures. Since the transverse displacement ($w$) is not explicitly defined over the interior of the DKT element, the determination of the derivatives of the transverse displacement ($w_{,x}, w_{,y}$) which are required to compute the initial stress matrix is not straightforward. The derivatives $(w_{,x}, w_{,y})$ are determined using a linear interpolation field for $w$ in terms of the nodal values. This kind of simpler interpolation for the transverse displacement has been widely used in many updated Lagrangian formulations in the existing literature that employ a flat shell element. The use of such linear interpolation for the displacement field to compute the geometric stiffness matrix is justified probably because most of the deformation of the element is made of rigid body rotations.

The element is first applied to study the control of thermal deformations of a spherical mirror segment (Kapania *et al.* [64]). This kind of study was required for the design of a next generation space telescope proposed by Jakubowski *et al.* [65], which employs a multi-segmented primary mirror. The feasibility of controlling the surface distortions of the mirror due to arbitrary thermal fields, using piezoelectric strips and force control actuators is studied using a finite element model of the mirror made up of the flat shell elements. In the case of the piezoelectric strips, the induced strain due to an externally applied voltage across the thickness of the strip bonded to the rear surface of the mirror, is used to control the surface distortions of the mirror. In the case of the force actuators the force exerted by the actuators normal to the rear surface of the mirror is used to control the surface distortions. The optimal voltages and the forces to be applied to the strips and actuators, respectively, are determined by minimizing the *rms* surface figure error of the mirror segment, which is a measure of the deviation of the deformed mirror surface from the desired surface. Since the piezoelectric strips have very light weight, a large number of such strips could be used without increasing the overall weight or stiffness of the mirror, unlike the force actuators which require a heavy backup structure which is not desirable for space applications. Since the piezoelectric strips are bonded to the rear surface of the mirror, they cannot be relocated. Hence a configuration of strips with predetermined locations will have to be used to control arbitrary surface distortions. A study is also conducted in order to compare the performance of a set of evenly placed strips and (near) optimally placed strips. The optimal locations of the piezoelectric strips are determined using a heuristic technique. Since the force actuators are used for both support and control, changing the locations of the actuators will result in different support configurations and hence different thermal deformations. In other words the problem does not remain the same by changing the locations of the actuators. Hence no attempt is made to determine the optimal locations.

The second application for which the element is intended to be used is the analysis of large inflatable structures which are expected to undergo large deformations. The updated Lagrangian formulation (Mohan and Kapania [62]) has been primarily developed to analyze large thin inflatable structures. When analyzing structures subject to pressure loads, the change in the direction of the pressure loads (follower action) should be taken into account in order to accurately compute the pressure load vector. As a result of the follower action, the pressure load vector is a function of the displacements and hence contributes to the tangent stiffness matrix as is the case with the thermal load. In the case of the thermal load, this contribution, is similar to the initial stress matrix and hence no additional effort is required to compute this contribution. In the case of the pressure load, this contribution called the pressure stiffness is in general unsymmetric and its determination is not straightforward but can be systematically derived from the principle of virtual work.

The literature on large deformation analysis, using the finite element method, of general shells under displacement-dependent pressure loads is very scarce. Hibbitt [66] presented a brief derivation of the load stiffness associated with some follower forces like pressure, centrifugal force, frictional drag and cable force using the principle of virtual work. Hibbitt showed that the pressure stiffness matrix can be split into two parts, a symmetric part corresponding to the interior and an antisymmetric part corresponding to the boundary of the structure, respectively. Hibbitt also showed that in the case of uniform pressure, with displacements prescribed on the boundaries, the pressure stiffness matrix becomes symmetric as the boundary terms vanish. When there are free boundaries, Hibbitt suggested that a symmetric pressure stiffness matrix defined as the average of the pressure stiffness matrix and its transpose could be used provided the elements near the free boundary are made very small. Neither details of the formulation nor any numerical examples are presented by Hibbitt.

Loganathan *et al.* [67], using a curved triangular shell element, presented linear buckling analyses of a thin circular arch and a cylindrical shell under uniform external pressure. They demonstrated that the inclusion of the pressure stiffness gave accurate values of the critical pressure.

Schweizerhof and Ramm [68] presented a total Lagrangian formulation applicable for isoparametric beam and shell elements, including the follower effects of the displacement dependent pressure loads. They considered two types of pressure loads: 1) space attached load for which the distribution of the load magnitude is a function of the coordinates in the deformed configuration; and 2) body attached load for which it is a function of the coordinates in the initial undeformed configuration. In both cases the pressure load acts normal to the deformed configuration. They showed that, for both types, the boundary terms of the pressure stiffness matrix are in general skew-symmetric, and the domain terms are always symmetric in the case of space attached loads, are symmetric for body attached uniform loads and are skew-symmetric for body attached nonuniform loads. They also outlined different types of boundary conditions under which the boundary terms are symmetric for both types of loads and suggested that the most efficient way to symmetrize the pressure stiffness matrix is to simply neglect the skew-symmetric terms. They came to interesting conclusions that flutter instability can only be detected using the unsymmetric pressure stiffness matrix, whereas in the case of static stability analysis the unsymmetric part has a minor influence on the critical load. They also remarked that the effect of totally neglecting the load/pressure stiffness matrix in determining the nonlinear response in some cases is only an increase in the number of equilibrium iterations. This statement is incorrect. From the author's experience, if the pressure stiffness matrix is totally neglected, the equilibrium iterations may not converge at all, especially in the regime of large rotations.

Yuan and Liang [69] presented the derivation of the pressure stiffness for a three-node axisymmetric shell element. Iwata *et al.* [70] presented a general form of the pressure stiffness matrix in a Cartesian coordinate system by relating, using the relationship given by Malvern [71], the area vector in the deformed configuration to that in the undeformed configuration. The derivation presented by Iwata *et al.* [70] does not distinguish clearly between the area elements in the deformed and undeformed configurations. They only presented results of a linear buckling analysis.

Gruttmann and Taylor [72] presented a membrane formulation including the pressure stiffness matrix. Their derivation of the pressure stiffness matrix is also based on relating the area vector in the deformed and undeformed configurations. Their pressure stiffness matrix turns out to be skew symmetric. They presented several numerical examples on the nonlinear response of rubber like membrane shells.

Christensen [73] studied the effects of pressure on the dynamics of structures stiffened due to high internal pressure such as the Space Shuttle solid rocket booster and the solid rocket motor. He presented a general formulation of the pressure stiffness for triangular and quadrilateral flat shell elements based on the assumption that the element deforms as a rigid body and hence used a linearly varying field for the translations. All the terms involving the nodal translational degrees of freedom in the expression for the pressure stiffness are neglected assuming that the nodal translations are much smaller than the element dimensions. This assumption may not be true in the case of problems involving large deformations. Christensen found that the natural frequencies of the rocket booster and motor, with the inclusion of the pressure stiffness, were in good agreement with those of the experimental results.

In the present research, large deformation analysis of general shells under deformation dependent pressure loads is performed using the updated Lagrangian formulation of the flat shell element (Mohan and Kapania [62]), by including the follower effects (Mohan and Kapania [63]). The pressure stiffness matrix and the deformation dependent pressure load vector are derived in a Cartesian coordinate system using the principle of virtual work. As in the case of the formulation by Christensen [73] and Schweizerhof and Ramm [68], the contribution of the rotational degrees of freedom to the pressure stiffness matrix and the pressure load vector is neglected. Unlike the formulation presented by Christensen [73], the displacement dependent terms in the pressure stiffness matrix and also in the pressure load vector are not neglected. Since the major part of the deformation of the element in the case of large deformation analysis is made up of rigid body motions, a linear interpolation field is assumed for the translational degrees of freedom as was done by Christensen [73]. A symmetric pressure stiffness matrix as proposed by Hibbitt [66] is employed in the present study.

The details of the finite element formulation are presented in Chapter 2. Several numerical examples on static, free vibration, thermal and geometrically non-linear analysis of laminated plates and shells are presented in Chapter 3 to demonstrate the validity of the present formulation. The first application of the element, namely the control of thermal deformation of a spherical mirror segment, is presented in Chapter 4.

The element is currently being used to analyze a large inflatable structure which is being considered by the US Army to be used as a transportable tent to accommodate Army vehicles and personnel. The tent is made up of arches stiffened by inflation and membranes that are connected to the arches and held under tension. A model of the tent structure made of two arches and a membrane is shown in (Fig. 1.1). The deformation of the tent under wind and snow loads is currently being studied. The results of the preliminary analysis are given in

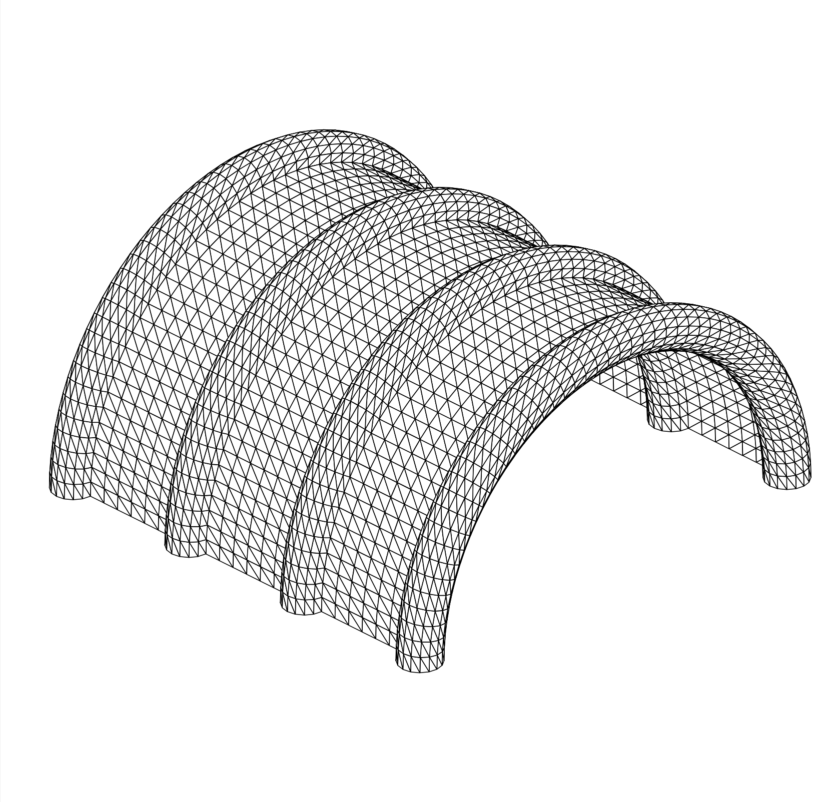

Figure 1.1: Tent structure

Chapter 5.

# Chapter 2

# Finite Element Formulation

The flat shell element used in this study is obtained by combining the Discrete Kirchhoff Theory (DKT) plate bending element of Batoz *et al.* [16] and a membrane element similar to the Allman triangle [3], but derived from the well known Linear Strain Triangular (LST) element. The derivation of the stiffness matrices in explicit form is not presented here. An elegant explicit formulation of the LST element is given by Subramanian and Bose [74]. An alternate explicit formulation of the DKT element along with a FORTRAN code are given by Jeyachandrabose [75]. A brief description of the LST and DKT elements is given first. Then the flat shell formulation and the solution techniques used are presented. Linear and non-linear formulations are dealt together. The updated Lagrangian formulation for a generally laminated structure is presented in detail, from which the governing equations for the linear analysis can be easily obtained. Only the solution techniques used to solve the system of non-linear equations are presented in detail since such techniques, though very widely used, have not been very well documented in the existing literature, especially in the case of thermal and pressure loads. Solution techniques like the subspace iteration and the derivation of the consistent mass matrix are not reproduced as they are well documented in many standard text books.

## 2.1 Membrane Formulation

The membrane element used in the present study has three nodes and three degrees of freedom at each node (two inplane displacements and an inplane rotation). The degrees of freedom of the membrane element are identical to those of the Allman triangular element, but the strain-displacement relations are derived from those of the LST element (which has three corner and three midside nodes and two inplane displacements at each node) by eliminating the midside displacements in terms of the corner displacements and rotations using the transformation suggested by Cook [5].

In the case of the LST element, the in-plane displacement fields $u$ and $v$ along the local $x$ and $y$ axes, respectively, are represented by the standard quadratic basis in area coordinates as follows

$$u = \sum_{i=1}^{6} P_i u_i, \qquad v = \sum_{i=1}^{6} P_i v_i \tag{2.1}$$

where $u_i$ and $v_i$ are the nodal values of the in-plane displacements and $P_i$ are the standard quadratic shape functions in area coordinates $\xi$ and $\eta$ given by

$$\{P\} = \left\{ \begin{array}{c} 2(1-\xi-\eta)(0.5-\xi-\eta) \\ \xi(2\xi-1) \\ \eta(2\eta-1) \\ 4\xi(1-\xi-\eta) \\ 4\xi\eta \\ 4\eta(1-\xi\eta) \end{array} \right\} \tag{2.2}$$

The local $x$-axis is taken along the side 1-2 of the element with the origin at node 1. The local $y$-axis is perpendicular to the local $x$-axis and lies in the plane passing through the three nodes. The shape functions in $\{P\}$ are arranged in such an order that the nodes 4, 5 and 6 are at the mid point of the sides 1-2, 2-3 and 3-1, respectively.

The normal and tangential displacements $u_n$ and $u_t$ along a typical element side 1-2 for example, as given by Allman [3] are,

$$u_n(s) = (1-\frac{s}{L_{12}})u_{n1} + \frac{s}{L_{12}}u_{n2} + \frac{s}{2}(1-\frac{s}{L_{12}})(\omega_2-\omega_1) \tag{2.3}$$

$$u_t = (1-\frac{s}{L_{12}})u_{t1} + \frac{s}{L_{12}}u_{t2} \tag{2.4}$$

where $s$ is the coordinate along edge 1-2, $L_{12}$ is the length of the edge 1-2, $u_{n1}, u_{t1}, u_{n2}, u_{t2}$ are the normal and tangential edge displacements at the nodes 1 and 2, respectively, $\omega_1$ and $\omega_2$ are the drilling degrees of freedom at nodes 1 and 2, respectively. The drilling degree of freedom $\omega$ is not exactly the true inplane rotation, but can be treated as the variation of the edge normal displacement $u_n$ with respect to the edge coordinate $s$ or in other words

$\omega = \partial u_n/\partial s$. The true inplane rotation about the normal to the plane of the element is given by

$$\Omega = \frac{1}{2}(\partial v/\partial x - \partial u/\partial y) \tag{2.5}$$

Using straightforward algebra, it can be shown that $\Omega$ and $\omega$ are related by

$$\Omega_i - \Omega_o = \frac{3}{4}(\omega_i - \omega_o) \tag{2.6}$$

where $\Omega_i$ are the true rotations at the vertices, $\Omega_0$ is the average value of the true nodal rotations, and $\omega_i$ and $\omega_0$ are the corresponding values of the drilling degree of freedom. The edge normal and tangential displacements $u_n$ and $u_t$ can be expressed as

$$u_n = u\ cos(\gamma_{12}) + v\ sin(\gamma_{12}) \tag{2.7}$$

$$u_t = -u\ sin(\gamma_{12}) + v\ cos(\gamma_{12}) \tag{2.8}$$

where $\gamma_{12}$ is the angle between the outward normal to the edge 1-2 and the positive direction of the local $x$-axis given by

$$cos(\gamma_{12}) = (y_2 - y_1)/L_{12}, \quad sin(\gamma_{12}) = (x_1 - x_2)/L_{12} \tag{2.9}$$

The midside displacements $u_4$ and $v_4$ can now be expressed in terms of the corner displacements and rotations as

$$u_4 = \frac{1}{2}u_1 + \frac{1}{2}u_2 + (y_1 - y_2)(\omega_1 - \omega_2)/8 \tag{2.10}$$

$$v_4 = \frac{1}{2}v_1 + \frac{1}{2}v_2 + (x_2 - x_1)(\omega_1 - \omega_2)/8 \tag{2.11}$$

Similar expressions can be obtained for the midside displacements of the other two edges. In the updated Lagrangian formulation discussed later in this section, the inplane strain-displacement relations are first obtained in terms of the degrees of freedom of the LST element, using the shape functions of the LST element and are expressed in terms of the degrees of the Allman element by eliminating the mid-side displacements using the expressions shown above. The shape functions proposed by Allman [5] are not used in any computations. The in-plane strain-displacement relations are presented later in this Chapter.

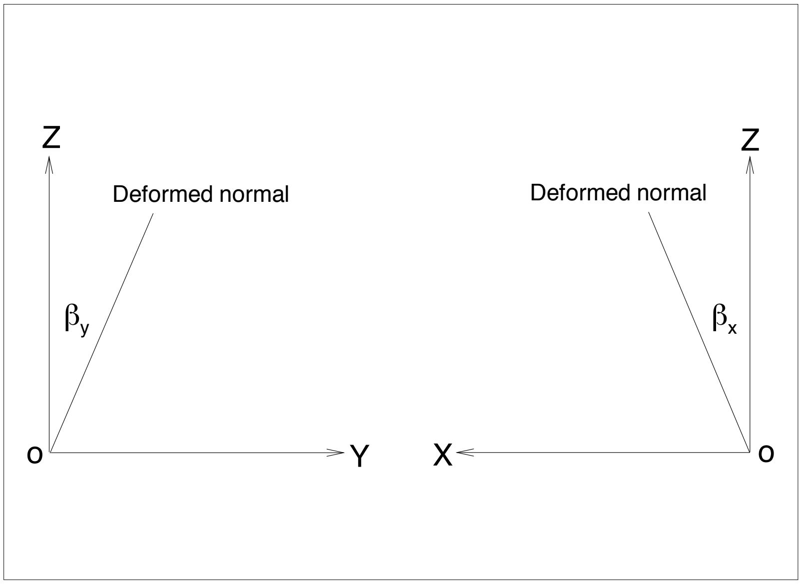

Figure 2.1: Positive directions of $\beta_x$ and $\beta_y$

## 2.2 Plate Bending Formulation

The formulation of the DKT plate bending element proceeds first by assuming that the transverse shear deformations are present. In other words the normal to the undeformed middle surface of the element remains straight after deformation, but is not necessarily normal to the deformed middle surface. With this assumption and considering that the rotations of the normal are small, the displacement components $u, v, w$ of any point $x, y, z$ in a local coordinate system can be expressed as

$$u = z\beta_x(x, y); \quad v = z\beta_y(x, y); \quad w = w(x, y) \tag{2.12}$$

where $\beta_x$ and $\beta_y$ are the rotations of the normal to the undeformed middle surface in the x-z and y-z planes, respectively. The positive senses of $\beta_x$ and $\beta_y$ are shown in Fig. 2.1. The bending strains (varying linearly through the thickness) can be expressed as

$$\{\epsilon_b\} = z\{\kappa\} \tag{2.13}$$

where $\{\kappa\}$ is the vector of curvatures given by

$$\{\kappa\} = \left\{ \begin{array}{c} \beta_{x,x} \\ \beta_{y,y} \\ \beta_{x,y} + \beta_{y,x} \end{array} \right\} \tag{2.14}$$

The transverse shear energy is neglected and the strain energy consisting only of the bending energy is expressed as

$$U = \frac{1}{2}\int_A \{\kappa\}^T[D]\{\kappa\}\;dA \tag{2.15}$$

where $A$ is the area of the undeformed middle surface of the element and $[D]$ is the standard matrix of elastic constants. Since the strain energy involves only the first derivatives of the normal rotations, the shape functions used to represent the normal rotations need to satisfy only C$^o$ continuity. Hence the normal rotations can be represented using the standard quadratic shape functions in area coordinates as

$$\beta_x = \sum_{i=1}^{6} \beta_{x_i} P_i \tag{2.16}$$

$$\beta_y = \sum_{i=1}^{6} \beta_{y_i} P_i \tag{2.17}$$

where $\beta_{x_i}$ and $\beta_{y_i}$ are the values of the normal rotations at the corners and mid point of element edges. The nodal degrees of freedom of the Kirchhoff plate elements in general are the transverse displacement $w$ and the slopes $\theta_x = w_{,y}$ and $\theta_y = -w_{,x}$. In order to derive the discrete equations of equilibrium in terms of the unknown nodal degrees of freedom of the element, the unknowns $\beta_{x_i}$ and $\beta_{y_i}$ should be expressed in terms of the nodal degrees of freedom $w_i$, $\theta_{x_i}$ and $\theta_{y_i}$. The 12 equations that relate the normal rotations at the corners and mid-sides to the degrees of freedom of the element are obtained by applying the discrete Kirchhoff assumptions which are explained in detail by Batoz *et al.* [16]. After applying the discrete Kirchhoff constraints, the normal rotations $\beta_x$ and $\beta_y$ can be expressed as

$$\beta_x \;=\; \frac{1}{2A}[H_x(\xi,\eta)]\{a_{dkt}\} \qquad\qquad \beta_y \;=\; \frac{1}{2A}[H_y(\xi,\eta)]\{a_{dkt}\} \tag{2.18}$$

where $\{a_{dkt}\}$ is the vector of nodal degrees of freedom of the DKT element given by $\{a_{dkt}\}^T = \{w_1\;\theta_{x_1}\;\theta_{y_1}\;w_2\;\theta_{x_2}\;\theta_{y_2}\;w_3\;\theta_{x_3}\;\theta_{y_3}\}$, and $[H_x]$ and $[H_y]$ are the vectors of shape functions given by Batoz *et al.* [16]. These shape functions have been reordered such that the nodes 4, 5 and 6 are at the midpoints of the sides 1-2, 2-3 and 3-1, respectively. This reordering has been done in order to match the order of the nodes with that of the LST element to avoid confusion while coding. The shape functions $[H_x]$ and $[H_y]$ after reordering are given by

$$H_x = \left\{ \begin{array}{c} 1.5(a_4P_4 \ - \ a_6P_6) \\ b_4P_4 \ + \ b_6P_6 \\ P_1 \ - \ c_4P_4 \ - \ c_6P_6 \\ 1.5(a_5P_5 \ - \ a_4P_4) \\ b_5P_5 \ + \ b_4P_4 \\ P_1 \ - \ c_5P_5 \ - \ c_4P_4 \\ 1.5(a_6P_6 \ - \ a_5P_5) \\ b_6P_6 \ + \ b_5P_5 \\ P_1 \ - \ c_6P_6 \ - \ c_4P_4 \end{array} \right\} \qquad H_y = \left\{ \begin{array}{c} 1.5(d_4P_4 \ - \ d_6P_6) \\ -P_1 \ + \ e_4P_4 \ + \ e_6P_6 \\ -b_4P_4 \ - \ b_6P_6 \\ 1.5(d_5P_5 \ - \ d_4P_4) \\ -P_1 \ + \ e_5P_5 \ + \ e_4P_4 \\ -b_5P_5 \ - \ b_4P_4 \\ 1.5(d_6P_6 \ - \ d_5P_5) \\ -P_1 \ + \ e_6P_6 \ + \ e_5P_5 \\ -b_6P_6 \ - \ b_5P_5 \end{array} \right\}$$

where

$$\begin{aligned} a_k &= -x_{ij}/l_{ij}^2 \\ b_k &= \tfrac{3}{4}x_{ij}y_{ij}/l_{ij}^2 \\ c_k &= (\tfrac{1}{4}x_{ij}^2 \ - \ \tfrac{1}{2}y_{ij}^2)/l_{ij}^2 \\ d_k &= -y_{ij}/l_{ij}^2 \\ e_k &= (\tfrac{1}{4}y_{ij}^2 \ - \ \tfrac{1}{2}x_{ij}^2)/l_{ij}^2 \\ l_{ij}^2 &= x_{ij}^2 \ + \ y_{ij}^2 \\ x_{ij} &= x_j - x_i \\ y_{ij} &= y_j - y_i \end{aligned}$$

where k = 4, 5, 6 corresponding to the sides $ij$ = 1-2, 2-3, 3-1, respectively, and $x_i, y_i$ are the nodal coordinates in the local coordinate system. As mentioned before, the derivation of the stiffness matrix in explicit form is not presented here. Only the shape functions of the LST and DKT elements are required to derive the governing non-linear equations of equilibrium of a generally laminated shell structure, which is presented in the next section.

## 2.3 Updated Lagrangian Formulation

### 2.3.1 Static analysis

The nonlinear equations of equilibrium governing the static response of a generally laminated structure are derived by applying the Principle of Virtual Work for a typical element using a local coordinate system as mentioned in section 2.1. It is assumed that a known equilibrium configuration $C_1$ at some time $t = t_1$ is available and that a new configuration $C_2$ at some time $t = t_2$ has to be determined. This is achieved by solving the nonlinear equations of equilibrium using the Newton-Raphson method, which is a standard iterative solution technique. Both $C_1$ and $C_2$ denote a local co-ordinate system. The Principle of Virtual Work can be expressed for a single element as follows:

$$\delta W_e = \delta W_i \tag{2.19}$$

where $\delta W_e$ is the virtual work done by external forces and $\delta W_i$ is the virtual work done by internal forces. The internal virtual work is given by

$$\delta W_i = \int_{C_1} \delta\{\epsilon\}^T \{s\}\, dV \tag{2.20}$$

where $V$ is the volume of the element in $C_1$, $\{\epsilon\}$ is the vector of incremental Green-Lagrange strains and $\{s\}$ is the vector of Second Piola-Kirchhoff (PK2) stresses. The PK2 stresses at any time $t_1 < t < t_2$ during the solution process can be decomposed as

$$\{s\} = \{\sigma\} + \{\Delta s\} \tag{2.21}$$

where $\{\sigma\}$ is the vector of Cauchy stresses in $C_1$ at time $t = t_1$ and $\{\Delta s\}$ is the vector of incremental PK2 stresses. The basic difference between the Cauchy stresses and the PK2 stresses is that the Cauchy stresses are measured in the current configuration, whereas the PK2 stresses are measured in the reference configuration. The term "current configuration" is used to denote any configuration between $C_1$ and $C_2$ obtained during the solution process. The incremental Green-Lagrange strains and PK2 stresses in any layer $k$ of a laminated structure are related by the constitutive equations given by

$$\{\Delta s\} = [\bar{Q}_k]\{\epsilon\} \tag{2.22}$$

where $[\bar{Q}_k]$ is the standard matrix of elastic constants transformed to the local element coordinate system and is given by

$$[\bar{Q}]_k = \begin{bmatrix} c^2 & s^2 & -2cs \\ s^2 & c^2 & 2cs \\ cs & -cs & c^2 - s^2 \end{bmatrix} \begin{bmatrix} q_{11} & q_{12} & 0 \\ q_{12} & q_{22} & 0 \\ 0 & 0 & q_{66} \end{bmatrix} \begin{bmatrix} c^2 & s^2 & -2cs \\ s^2 & c^2 & 2cs \\ cs & -cs & c^2 - s^2 \end{bmatrix}^T \tag{2.23}$$

where $q_{11} = E_1/(1 - \nu_{12}\nu_{21})$, $q_{12} = \nu_{12}E_2/(1 - \nu_{12}\nu_{21})$, $q_{22} = E_2/(1 - \nu_{12}\nu_{21})$, $q_{66} = G_{12}$, $c = cos(\theta)$, $s = sin(\theta)$ and $E_1, E_2, \nu_{12}, G_{12}$ are the properties in the principal material directions of the $k^{th}$ layer and $\theta$ is the angle which the $E_1$ direction of the $k^{th}$ layer makes with the local $x$-axis, measured counter clock wise from the local $x$-axis.

At the end of the current step ($t = t_2$) the PK2 stresses in $C_1$, computed using Eqs. 2.21 and 2.22, are converted to Cauchy stresses in $C_2$ by a series of transformations involving the deformation gradient tensor and the rotation tensor (Kleiber [76]), but for small strains it can be shown (Farfard *et al.* [49] ) that at the end of the current step the PK2 stresses computed in $C_1$ are equal to the Cauchy stresses in $C_2$.

Assuming that the thickness of the structure and the incremental rotations are moderate, the variation of strain through the thickness can be expressed as

$$\{\epsilon\} \;=\; \{e\} \;+\; z\;\{\kappa\}\; -\{\;\epsilon^0\} \tag{2.24}$$

where $\{e\}$, $\{\kappa\}$ and $\{\epsilon^0\}$ are the vectors of incremental membrane strains, bending strains and thermal strains, respectively, and are given by

$$\{e\} \;=\; \left\{ \begin{array}{c} u_{,x} + 1/2(u_{,x}^2 + v_{,x}^2 + w_{,x}^2) \\ v_{,y} + 1/2(u_{,y}^2 + v_{,y}^2 + w_{,y}^2) \\ u_{,y} + v_{,x} + u_{,x}u_{,y} + v_{,x}v_{,y} + w_{,x}w_{,y} \end{array} \right\} \tag{2.25}$$

$$\{\kappa\} \;=\; \{\beta_{x,x}\;\beta_{y,y}\;\beta_{x,y} + \beta_{y,x}\}^T \tag{2.26}$$

$$\{\epsilon^0\} \;=\; \{\alpha_x\;\alpha_y\;\alpha_{xy}\}_k^T \Delta T \tag{2.27}$$

where $u, v, w$ are the incremental displacements of the mid-plane of the element, $\beta_x$ and $\beta_y$ are the incremental rotations of the normal to the undeformed mid-plane in the local $x - z$ and $y - z$ planes, respectively, $\Delta T$ is the prescribed temperature increment, and $\alpha_x, \alpha_y$ and $\alpha_{xy}$ are the coefficients of thermal expansion with respect to the element local coordinate system for the $k^{th}$ layer given by

$$\left\{ \begin{array}{c} \alpha_x \\ \alpha_y \\ \alpha_{xy} \end{array} \right\}_k = \left[ \begin{array}{ccc} c^2 & s^2 & -cs \\ s^2 & c^2 & cs \\ 2cs & -2cs & c^2 - s^2 \end{array} \right]_k \left\{ \begin{array}{c} \alpha_1 \\ \alpha_2 \\ \alpha_{12} \end{array} \right\}_k \tag{2.28}$$

where $\alpha_1, \alpha_2$ and $\alpha_{12}$ are the coefficients of thermal expansion with respect to the principal material directions of the $k^{th}$ layer. The internal virtual work can now be expressed as

$$\delta W_i \;=\; \int_{C_1} \delta\{\epsilon\}^T\{s\}\; dV \;=\; \int_{C_1} \Big(\delta\{e\}^T\{N\} \;+\; \delta\{\kappa\}^T\{M\}\Big)\; dA \tag{2.29}$$

where $A$ is the area of the mid-plane of the element in $C_1$, and $\{N\}$ and $\{M\}$ are the force and moment resultants, respectively:

$$\{N, M\} \;=\; \int_{-\frac{h}{2}}^{\frac{h}{2}} \{s\}(1, z)\; dz \tag{2.30}$$

where $h$ is the thickness of the laminate. Using Eqs. 2.21 and 2.22, the force and moment resultants can be decomposed as

$$\{N\} = \{N_1\} + \{\Delta N^m\} - \{\Delta N^0\} \tag{2.31}$$

$$\{M\} = \{M_1\} + \{\Delta M^m\} - \{\ \Delta M^0\} \tag{2.32}$$

where $\{N_1\}$, $\{M_1\}$ are the force and moment resultants in $C_1$ at time $t = t_1$, $\{\Delta N^m\}$, $\{\Delta M^m\}$ are the incremental force and moment resultants due to mechanical stresses and $\{\Delta N^0\}$, $\{\Delta M^0\}$ are the incremental force and moment resultants due to thermal stresses:

$$\{N_1, M_1\} \;=\; \int_{-\frac{h}{2}}^{\frac{h}{2}} \{\sigma\}(1, z)\; dz \tag{2.33}$$

$$\{\Delta N^m\} \;=\; \int_{-\frac{h}{2}}^{\frac{h}{2}} [\bar{Q}_k]\; (\{e\} + z\{\kappa\})\; dz \;=\; [A]\{e\} \;+\; [B]\{\kappa\} \tag{2.34}$$

$$\{\Delta M^m\} \;=\; \int_{-\frac{h}{2}}^{\frac{h}{2}} [\bar{Q}_k]\; (\{e\} + z\{\kappa\})z\; dz \;=\; [B]\{e\} \;+\; [D]\{\kappa\} \tag{2.35}$$

$$\{\Delta N^0, \Delta M^0\} \;=\; \int_{-\frac{h}{2}}^{\frac{h}{2}} [\bar{Q}_k]\; \{\epsilon^0\}\; (1, z)\; dz \tag{2.36}$$

where $[A], [B], [D]$ are the standard matrices of elastic constants. In the present study all the area integrals are evaluated using a 3 point integration scheme in area coordinates (Yang [2]). The integral over the thickness is computed by summing the contribution from each layer of the laminate. The first variation of the membrane strains can be expressed as

$$\{\delta e\} \;=\; \left\{ \begin{array}{c} \delta u_{,x} + u_{,x}\delta u_{,x} + v_{,x}\delta v_{,x} + w_{,x}\delta w_{,x} \\ \delta v_{,y} + u_{,y}\delta u_{,y} + v_{,y}\delta v_{,y} + w_{,y}\delta w_{,y} \\ \delta u_{,y} + \delta v_{,x} + u_{,x}\delta u_{,y} + u_{,y}\delta u_{,x} + v_{,x}\delta v_{,y} + v_{,y}\delta v_{,x} + w_{,x}\delta w_{,y} + w_{,y}\delta w_{,x} \end{array} \right\} \tag{2.37}$$

The above equation can be rearranged as

$$\{\delta e\} \;=\; [G_1]\{\delta u_{,x}\; \delta u_{,y}\; \delta v_{,x}\; \delta v_{,y}\; \delta w_{,x}\; \delta w_{,y}\}^T \tag{2.38}$$

where

$$[G_1] = \begin{bmatrix} 1+u_{,x} & 0 & v_{,x} & 0 & w_{,x} & 0 \\ 0 & u_{,y} & 0 & 1+v_{,y} & 0 & w_{,y} \\ u_{,y} & 1+u_{,x} & 1+v_{,y} & v_{,x} & w_{,y} & w_{,x} \end{bmatrix} \tag{2.39}$$

The in-plane displacements $u$ and $v$ can be expressed in terms of the nodal quantities as

$$\begin{Bmatrix} u \\ v \end{Bmatrix} = \begin{bmatrix} \{P\}^T & 0 \\ 0 & \{P\}^T \end{bmatrix} \{a_{lst}\} \tag{2.40}$$

where $\{a_{lst}\}$ is the vector of nodal degrees of freedom of the LST element given by $\{a_{lst}\} = \{u_1, u_2, u_3, u_4, u_5, u_6, v_1, v_2, v_3, v_4, v_5, v_6\}$ and $\{P\}$ is the vector of quadratic shape functions in area co-ordinates given by Eq. 2.2. The derivatives of the in-plane displacements are given by

$$\begin{Bmatrix} u_{,x} \\ u_{,y} \\ v_{,x} \\ v_{,y} \end{Bmatrix} = \begin{bmatrix} \{P_{,x}\}^T & 0 \\ \{P_{,y}\}^T & 0 \\ 0 & \{P_{,x}\}^T \\ 0 & \{P_{,y}\}^T \end{bmatrix} [T_{lst}]\{a\} = [B_{lst}]\{a\} \tag{2.41}$$

where $\{P_{,x}\}$ and $\{P_{,y}\}$ are the vectors of derivatives of the shape functions with respect to the local $x$ and $y$ co-ordinates, respectively, and are given by

$$\{P_{,x}\} = \frac{1}{2A}\Big(b_2\{P_{,\xi}\} + b_3\{P_{,\eta}\}\Big) \tag{2.42}$$

$$\{P_{,y}\} = \frac{1}{2A}\Big(c_2\{P_{,\xi}\} + c_3\{P_{,\eta}\}\Big) \tag{2.43}$$

where $2A = b_2c_3 - c_2b_3, b_2 = y_3 - y_1, b_3 = y_1 - y_2, c_2 = x_1 - x_3, c_3 = x_2 - x_1$. The matrix $[T_{lst}]$ is used to express the nodal degrees of the LST element $\{a_{lst}\}$ in terms of the nodal degrees of freedom of the shell element $\{a\}$ as $\{a_{lst}\} = [T_{lst}]\{a\}$, where $\{a\}^T = \{u_1, v_1, w_1, \theta_{x_1}, \theta_{y_1}, \theta_{z_1}, u_2, v_2, w_2, \theta_{x_2}, \theta_{y_2}, \theta_{z_2}, u_3, v_3, w_3, \theta_{x_3}, \theta_{y_3}, \theta_{z_3}\}$. The transformation matrix $[T_{lst}]$ is given by

$$[T_{lst}] = \begin{bmatrix} 1 & 0 & 0 & 0 & 0 & 0 & 0 & 0 & 0 & 0 & 0 & 0 & 0 & 0 & 0 & 0 & 0 & 0 \\ 0 & 0 & 0 & 0 & 0 & 0 & 1 & 0 & 0 & 0 & 0 & 0 & 0 & 0 & 0 & 0 & 0 & 0 \\ 0 & 0 & 0 & 0 & 0 & 0 & 0 & 0 & 0 & 0 & 0 & 0 & 1 & 0 & 0 & 0 & 0 & 0 \\ 0.5 & 0 & 0 & 0 & 0 & b_3/8 & 0.5 & 0 & 0 & 0 & 0 & -b_3/8 & 0 & 0 & 0 & 0 & 0 & 0 \\ 0 & 0 & 0 & 0 & 0 & 0 & 0.5 & 0 & 0 & 0 & 0 & b_1/8 & 0.5 & 0 & 0 & 0 & 0 & -b_1/8 \\ 0.5 & 0 & 0 & 0 & 0 & -b_2/8 & 0 & 0 & 0 & 0 & 0 & 0 & 0.5 & 0 & 0 & 0 & 0 & b_2/8 \\ 0 & 1 & 0 & 0 & 0 & 0 & 0 & 0 & 0 & 0 & 0 & 0 & 0 & 0 & 0 & 0 & 0 & 0 \\ 0 & 0 & 0 & 0 & 0 & 0 & 0 & 1 & 0 & 0 & 0 & 0 & 0 & 0 & 0 & 0 & 0 & 0 \\ 0 & 0 & 0 & 0 & 0 & 0 & 0 & 0 & 0 & 0 & 0 & 0 & 0 & 1 & 0 & 0 & 0 & 0 \\ 0 & 0.5 & 0 & 0 & 0 & c_3/8 & 0 & 0.5 & 0 & 0 & 0 & -c_3/8 & 0 & 0 & 0 & 0 & 0 & 0 \\ 0 & 0 & 0 & 0 & 0 & 0 & 0 & 0.5 & 0 & 0 & 0 & c_1/8 & 0 & 0.5 & 0 & 0 & 0 & -c_1/8 \\ 0 & 0.5 & 0 & 0 & 0 & -c_2/8 & 0 & 0 & 0 & 0 & 0 & 0 & 0 & 0.5 & 0 & 0 & 0 & c_2/8 \end{bmatrix}$$

In the case of the DKT element the transverse displacement $w$ is not defined explicitly over the interior of the element. The derivatives $w_{,x}$ and $w_{,y}$ at the integration points can be obtained using a linear interpolation in terms of the nodal values, but this kind of interpolation required a very fine mesh and small load steps, probably due to the non-conformal nature of the derivatives along the element sides. Past experience (Farfard *et al.* [49]) has shown that evaluating the derivatives from a linear interpolation for $w$ using the nodal values gives better results. In the present study the same approach is followed. In area coordinates, $w$ is expressed as $w(\xi, \eta) = (1 - \xi - \eta)w_1 + \xi w_2 + \eta w_3$ from which the derivatives can be obtained as

$$\begin{Bmatrix} w_{,x} \\ w_{,y} \end{Bmatrix} = \frac{1}{2A} \begin{bmatrix} -b_2 - b_3 & b_2 & b_3 \\ -c_2 - c_3 & c_2 & c_3 \end{bmatrix} [T_w]\{a\} = [B_w]\{a\} \tag{2.44}$$

where $[T_w]$ is used to express $\{w_1\ w_2\ w_3\}^T$ in terms of $\{a\}$ as $\{w_1\ w_2\ w_3\}^T = [T_w]\{a\}$. The transformation matrix $[T_w]$ is made of zeroes and ones, the determination of which is straightforward. Combining Eqs. 2.41 and 2.44, the first variation of the membrane strains can be expressed as

$$\{\delta e\} = [G_1][G_2]\{\delta a\} \tag{2.45}$$

where $[G_2]$ is a matrix of size 6x18 with the first 4 rows made of $[B_{lst}]$ and the last 2 rows made of $[B_w]$. The first variation of the bending strains can now be expressed as

$$\{\delta\kappa\} \;=\; \frac{1}{2A}\begin{bmatrix} b_2H_{x,\xi}^T + b_3H_{x,\eta}^T \\ c_2H_{y,\xi}^T + c_3H_{y,\eta}^T \\ c_2H_{x,\xi}^T + c_3H_{x,\eta}^T + b_2H_{y,\xi}^T + b_3H_{y,\eta}^T \end{bmatrix}[T_{dkt}]\{\delta a\} \;=\; [B_{dkt}]\{\delta a\} \tag{2.46}$$

where $H_{x,\xi}, H_{x,\eta}, H_{y,\xi}, H_{y,\eta}$ are the derivatives of the shape functions with respect to the area coordinates given by

$$H_{x,\xi} = \left\{\begin{matrix} p4(1-2\xi) + (p6-p4)\eta) \\ q4(1-2\xi) - (q6+q4)\eta) \\ -4+6(\xi+\eta) + r4(1-2\xi) - \eta(r6+r4) \\ -p4(1-2\xi) + \eta(p5+p4) \\ q4(1-2\xi) - \eta(q4-q5) \\ -2+6\xi) + r4(1-2\xi)) + \eta(r5-r4) \\ -\eta(p6+p5) \\ \eta(q5-q6) \\ -\eta(r6-r5) \end{matrix}\right\}$$

$$H_{x,\eta} = \left\{\begin{matrix} -p6(1-2\eta) - (p4-p6)\xi \\ q6(1-2\eta) - (q6+q4)\xi \\ -4+6(\xi+\eta) + r6(1-2\eta) - \xi(r6+r4) \\ \xi(p5+p4) \\ \xi(q5-q4) \\ -\xi(r4-r5) \\ p6(1-2\eta) - \xi(p5+p6) \\ q6(1-2\eta) + \xi(q5-q6) \\ -2+6\eta + r6(1-2\eta) + \xi(r5-r6) \end{matrix}\right\}$$

$$H_{y,\xi} = \left\{ \begin{array}{c} t4(1-2\xi)+\eta(t6-t4) \\ 1+r4(1-2\xi)-\eta(r6+r4) \\ -q4(1-2\xi)+\eta(q6+q4) \\ -t4(1-2\xi)+\eta(t5+t4) \\ -1+r4(1-2\xi)+\eta(r5-r4) \\ -q4(1-2\xi)-\eta(q5-q4) \\ -\eta(t5+t6) \\ \eta(r5-r6) \\ -\eta(q5-q6) \end{array} \right\}$$

$$H_{y,\eta} = \left\{ \begin{array}{c} -t6(1-2\eta)-\xi(t4-t6) \\ 1+r6(1-2\eta)-\xi(r6+r4) \\ -q6(1-2\eta)+\xi(q6+q4) \\ \xi(t5+t4) \\ \xi(r5-r4) \\ -\xi(q5-q4) \\ t6(1-2\eta)-\xi(t5+t6) \\ -1+r6(1-2\eta)+\xi(r5-r6) \\ -q6(1-2\eta)-\xi(q5-q6) \end{array} \right\}$$

The matrix $[T_{dkt}]$ which is used to expresses $\{a_{dkt}\}$ in terms of $\{a\}$ as $\{a_{dkt}\} = [T_{dkt}]\{a\}$, is made up of zeroes and ones, the determination of which is straightforward.
The external virtual work can be expressed as

$$\delta W_e \ = \ \{\delta a\}^T\{f\} \tag{2.47}$$

where $\{f\}$ is the element external force vector. The equations of equilibrium at the element level can be expressed as

$$\{g\} = \{q\} - \{f\} = 0 \tag{2.48}$$

where $\{q\}$ is the element internal force vector given by

$$\{q\} = \int_{C_1} \Big( [G_2]^T[G_1]^T\{N\} \ + \ [B_{dkt}]^T\{M\} \Big) \, dA \tag{2.49}$$

The element internal and external force vectors thus obtained in the element local co-ordinates are converted to the global co-ordinates using the standard coordinate transformation (Zienkiewicz [13]) and are assembled to obtain the global internal force vector $\mathbf{q}$ and external force vector $\mathbf{f}$. In the rest of this chapter vectors and matrices in the global coordinate system are denoted in bold face. The non-linear governing equations of equilibrium of the entire finite element model in the global Cartesian co-ordinate system at any time $t$ can be written as $\mathbf{g}_t = \mathbf{q}_t - \mathbf{f}_t = 0$, where $\mathbf{g}$ is the residue or the imbalance between the internal and external forces.

The non-linear equations of equilibrium are solved using the Newton-Raphson method, an iterative or step-by-step process in which a linearized form of the equilibrium equations is solved in each step. Assuming that a known equilibrium configuration exists at some time $t_1$, the equations of equilibrium at some time $t_1 + \Delta t$ can be linearized using the truncated Taylor series expansion about the known configuration at time $t_1$ as

$$\mathbf{g}_{t_1+\Delta t} = \mathbf{q}_{t_1} + \left(\frac{\partial \mathbf{q}}{\partial \mathbf{a}}\right)_{t_1} \delta\mathbf{a} - \mathbf{f}_{t_1+\Delta t} \;=\; \mathbf{q}_{t_1} + [\mathbf{K}]\;\delta\mathbf{a} \;-\; \mathbf{f}_{t_1+\Delta t} \;=\; 0 \tag{2.50}$$

where $[\mathbf{K}]$ is the global tangent stiffness matrix which is obtained by transforming the local element stiffness matrices $[\mathbf{k}]$ (obtained by taking the derivative of the element internal force vector $\{q\}$ in Eq. 2.49 with respect to $\{a\}$) and assembling them in the standard way. The external force vector $\mathbf{f}$ could also be a function of the displacements. This case is dealt with later in this Chapter. The derivative of the terms in Eq. 2.49 are obtained using the chain rule $\delta(\;) = (\partial(\;)/\partial\{a\})\delta\{a\}$. Using Eqs. 2.31, 2.32, 2.34, 2.35, 2.37 and 2.46, the derivatives of $\{N\}$ and $\{M\}$ with respect to $\{a\}$ can be readily obtained as

$$\frac{\partial\{N\}}{\partial\{a\}} = [A][G_1][G_2] \;+\; [B][B_{dkt}] \qquad \frac{\partial\{M\}}{\partial\{a\}} = [B][G_1][G_2] \;+\; [D][B_{dkt}] \tag{2.51}$$

The variation of the product $[G_2]^T[G_1]^T\{N\}$ is given by

$$\delta([G_2]^T[G_1]^T\{N\}) \;=\; [G_2]^T(\delta[G_1]^T)\{N\} \;+\; [G_2]^T[G_1]^T\delta\{N\} \tag{2.52}$$

Using the special property of the matrix $[G_1]$ (Zienkiewicz and Taylor [77], p. 294), the product $(\delta[G_1]^T)\{N\}$ can be expressed as

$$(\delta[G_1]^T)\{N\} \;=\; \begin{bmatrix} \hat{N} & 0 & 0 \\ 0 & \hat{N} & 0 \\ 0 & 0 & \hat{N} \end{bmatrix} [G_2]\delta\{a\} \tag{2.53}$$

where $n_x, n_y$ and $n_{xy}$ are the components of $\{N\}$ and $\hat{N} = \begin{bmatrix} n_x & n_{xy} \\ n_{xy} & n_y \end{bmatrix}$

The derivative of $[G_2]^T[G_1]^T\{N\}$ with respect to $\{a\}$ can be easily obtained using Eqs. 2.52, 2.53 and the chain rule. The element tangent stiffness matrix $[\mathbf{k}]$ can now be expressed as

$$\begin{aligned} [\mathbf{k}] \ &= \ \int_{C_1} \Big( [G_2]^T[G_1]^T[A][G_1][G_2] \ + \ [B_{dkt}]^T[D][B_{dkt}] \ + \ [B_{dkt}]^T[B][G_1][G_2] \\ &\quad + \ [G_2]^T[G_1]^T[B][B_{dkt}] \ + \ [G_2]^T \begin{bmatrix} \hat{N} & 0 & 0 \\ 0 & \hat{N} & 0 \\ 0 & 0 & \hat{N} \end{bmatrix} [G_2] \Big) \, dA \end{aligned} \tag{2.54}$$

The Newton-Raphson method using load control and arc-length control is illustrated first for a concentrated load and then the steps that are to be modified for thermal and pressure loads are shown. The arc-length method used in the present study is that of Crisfield [78].

### 2.3.2 Newton-Raphson method with load control for a concentrated load

Let a known equilibrium configuration exist at some instant $t = t_1$, the total load applied to arrive at this configuration be $\mathbf{f_1} = \lambda_1 \, \mathbf{q_{ref}}$ and $\mathbf{a_1}$ be the solution at this instant. Here $\mathbf{q_{ref}}$ is a fixed reference load and $\lambda_1$ is the load proportionality factor. Since the reference load $\mathbf{q_{ref}}$ considered here is a concentrated load in the global Cartesian coordinate system, it is obtained just by prescribing the values of the global nodal forces. The new configuration at some instant $t = t_2$ is obtained by an incremental-iterative process in which a linearized form of the equilibrium equations is solved in each step. Let $\Delta\mathbf{f} = \Delta\lambda \, \mathbf{q_{ref}}$ be the incremental load applied to the structure at equilibrium at instant $t = t_1$ and $\mathbf{a}$ be the incremental displacement vector. In each step the external load applied to the structure is held constant. The incremental load factor $\Delta\lambda$ can be held constant for all the steps or varied for each step. The equations of equilibrium at $t = t_1 + \Delta t$ can be written as

$$\mathbf{g}_{t_1+\Delta t} \ = \ \mathbf{g}_{t_1} \ + \ [\mathbf{K}] \, \delta\mathbf{a} \ - \ \Delta\lambda \, \mathbf{q}_{ref} \ = \ 0 \tag{2.55}$$

Since the configuration at the beginning of the load increment $\Delta\lambda$ is in equilibrium the residue $\mathbf{g}_{t_1}$ is identically zero. The solution to this incremental step can be obtained from $[\mathbf{K}] \ \delta\mathbf{a} \ = \Delta\lambda \ \mathbf{q_{ref}}$ and the solution is updated as $\mathbf{a} = \mathbf{a} + \delta\mathbf{a}$ and $\mathbf{a_2} = \mathbf{a_1} + \mathbf{a}$. The incremental displacement $\mathbf{a}$ at the beginning of the step is obviously zero. The solution $\mathbf{a_2}$ thus obtained is only an estimate of the actual solution, as the new configuration may not be in equilibrium with the external forces. The correction to the solution (obtained by linearizing the equations of equilibrium about the new solution point) is given by $[\mathbf{K}]\ \delta\mathbf{a} = -\mathbf{g_{t_1+\Delta t}}$ and the solution is updated as $\mathbf{a} = \mathbf{a} + \delta\mathbf{a}$ and $\mathbf{a_2} = \mathbf{a_1} + \mathbf{a}$. This process is repeated until the solution converges or the unbalance force diminishes to a very small value. The residue $\mathbf{g}_{t_1+\Delta t}$ is obtained by assembling the element residual vectors given by Eq. 2.48 in the standard way. The force and moment resultants $\{N\}$ and $\{M\}$ and the matrix $[G_1]$ used in Eq. 2.49 to compute the element internal force vector are evaluated at each integration point using the local incremental displacement vector $\{a\}$ which is obtained from the global incremental displacement vector $\mathbf{a}$ in the standard way. The tangent stiffness matrix $[\mathbf{K}]$ is updated every time the solution is updated (regular Newton-Raphson method). If the tangent stiffness matrix is computed only at the beginning of each increment and not updated after every iteration (modified Newton-Raphson method), especially in the case of large rotation analysis, a large number of iterations will have to be performed or the solution might even start diverging.

Several convergence criteria are available in the existing literature to check the convergence of the solution during the incremental-iterative process. In the present study the iterations are performed until the ratio of maximum correction to the displacements in an iteration to maximum incremental translation and the ratio of maximum correction to the rotations in an iteration to the maximum incremental rotation are both less than $10^{-3}$. In other words if the solution vectors $\mathbf{a}$ and $\delta\mathbf{a}$ are split into displacements and rotations as $\mathbf{a} = \mathbf{a_t} + \mathbf{a_r}$ and $\delta\mathbf{a} = \delta\mathbf{a_t} + \delta\mathbf{a_r}$, then the convergence criteria can be expressed as $\|\delta\mathbf{a_t}\|_\infty / \|\mathbf{a_t}\|_\infty < 10^{-3}$ and $\|\delta\mathbf{a_r}\|_\infty / \|\mathbf{a_r}\|_\infty < 10^{-3}$. At the end of a load step, instead of updating the stresses as given by Eq. 2.21, the force and moment resultants $\{N\}$ and $\{M\}$ at each integration point for each element are updated as given by Eqs. 2.31 and 2.32 and are used as $\{N_1\}$ and $\{M_1\}$ for the next step.

### 2.3.3 Newton-Raphson method with arc-length control for a concentrated load

The major difference between load control and arc-length control is that in the case of load control the applied load in any given step is held constant, whereas in the case of arc-length control the applied load is allowed to vary in any given step. In other words, the load factor $\lambda$ does not remain constant in a step in the case of arc-length control. Since the load factor is an unknown, an equation in addition to the equilibrium equations (Eq. 2.48) is required to determine the change in the load factor in each step. This is achieved by imposing a constraint $\mathbf{a}^T\mathbf{a} = \Delta l^2$, where $l$ is a constant called the arc-length. Since the load does not remain constant in any step, the total load at some time $t_1 + \Delta t$ can be written as $\mathbf{f}_{t_1+\Delta t} = \mathbf{f}_{t_1} + \delta\lambda\ \mathbf{q}_{ref}$. The equlibrium equations at time $t_1 + \Delta t$ can now be expressed as

$$\mathbf{g}_{t_1+\Delta t} = \mathbf{g}_{t_1} + [\mathbf{K}]\ \delta\mathbf{a} - \delta\lambda\ \mathbf{q_{ref}} = \mathbf{0} \tag{2.56}$$

Let $\Delta\lambda_0$ be the constant incremental load parameter used for the incremental step as in the case of load control. The solution to this incremental step is obtained as before from $[\mathbf{K}]\ \delta\mathbf{a} = \boldsymbol{\Delta\lambda_0}\ \mathbf{q_{ref}}$ and the solution is updated as $\mathbf{a} = \mathbf{a} + \delta\mathbf{a}$ and $\mathbf{a_2} = \mathbf{a_1} + \mathbf{a}$. In the subsequent iterations the correction to the solution (obtained by linearizing the equations of equilibrium at the new solution point) is obtained from

$$\delta\mathbf{a} = -[\mathbf{K}]^{-\mathbf{1}}\ \mathbf{g_{t_1+\Delta t}}\ +\ \delta\lambda\ [\mathbf{K}]^{-\mathbf{1}}\ \mathbf{q_{ref}}\ =\ \delta\bar{\mathbf{a}}\ +\ \delta\lambda\ \delta\mathbf{a_t} \tag{2.57}$$

where the residue $\mathbf{g}_{t_1+\Delta t}$ is obtained as in the case of load control and the change in the load parameter $\delta\lambda$ is obtained by applying the constraint as follows:

$$(\mathbf{a} + \delta\mathbf{a})^T(\mathbf{a} + \delta\mathbf{a}) = \Delta l^2 \tag{2.58}$$

where $\mathbf{a}$ is the solution at the end of the previous iteration (or at the end of the incremental step) and $\mathbf{a} + \delta\mathbf{a}$ is the solution that will be obtained at the end of the current iteration after determining the change in the load parameter $\delta\lambda$. In Eq. 2.57 the updated value of $[\mathbf{K}]$ is used. When $\delta\mathbf{a}$ from Eq. 2.57 is substituted into the constraint equation (Eq. 2.58), the resulting quadratic equation is given by

$$a_1\ \delta\lambda^2 + a_2\ \delta\lambda + a_3 = 0 \tag{2.59}$$

where

$$\begin{aligned} a_1 &= \delta\mathbf{a_t^T}\delta\mathbf{a_t} \\ a_2 &= 2(\mathbf{a} + \delta\bar{\mathbf{a}})^{\mathbf{T}}\delta\mathbf{a_t} \\ a_3 &= (\mathbf{a} + \delta\bar{\mathbf{a}})^{\mathbf{T}}(\mathbf{a} + \delta\bar{\mathbf{a}}) \end{aligned} \tag{2.60}$$

Out of the two roots of Eq. 2.59, the one which results in the least root mean square error between the solution at the end of the previous iteration $\mathbf{a}$ and the solution at the end of the current iteration $\mathbf{a} + \delta\mathbf{a}$, is selected. The load factor should also be updated at the end of each iteration in order to correctly compute the total load acting on the structure at any time. For example, at the end of the first iterative step, the total load acting on the structure will be $(\lambda_1 + \Delta\lambda_0 + \delta\lambda)\mathbf{q}_{ref}$, or the load increment at the end of the first iteration will be $\Delta\lambda = \Delta\lambda_0 + \delta\lambda$ and the total load acting on the structure will be $\mathbf{f}_1 + \Delta\lambda\mathbf{q}_{ref}$. The solution at the end of the current iteration is updated as before as $\mathbf{a} = \mathbf{a} + \delta\mathbf{a}$ and $\mathbf{a_2} = \mathbf{a_1} + \mathbf{a}$.

In the very first step, the incremental load parameter $\Delta\lambda_0$ is suitably chosen and the arc length $\Delta l$ is determined as

$$\Delta l = \Delta\lambda_0 \sqrt{(\mathbf{a}_0^T \mathbf{a}_0)} \tag{2.61}$$

where $\mathbf{a}_0$ is obtained from

$$[\mathbf{K}]\ \mathbf{a}_0 = \mathbf{q}_{ref} \tag{2.62}$$

where $[\mathbf{K}]$ is the global tangent stiffness matrix at the beginning of the incremental step or at time $t = t_1$ and is made up of only the linear stiffness matrix and the initial stress matrix (the last term in Eq. (2.54)). All the non-linear terms are zero since the incremental displacement vector at the beginning of the load step is identically equal to zero. For subsequent steps, the arc length may be adjusted such that a more or less constant number of iterations is required to obtain convergence, using the following relation (Crisfield [78]):

$$\Delta l_i = \Delta l_{i-1} N_d / N_{i-1} \tag{2.63}$$

where $\Delta l_i$ is the constant arc length to be used in the current step, $\Delta l_{i-1}$ is the constant arc length used in the previous step, $N_{i-1}$ is the number of iterations needed in the previous step and $N_d$ is the desired number of iterations to be performed in any step to obtain convergence based on the chosen convergence criterion. For all the steps other than the first, the incremental loading parameter $\Delta\lambda_0$ used for the tangential step is obtained by

$$\Delta\lambda_0 = \pm\Delta l_i / \sqrt{(\mathbf{a}_o^T \mathbf{a}_0)} \tag{2.64}$$

The sign follows that of the previous step (positive in the very first step) unless the determinant of the tangent stiffness matrix has changed sign, in which case a sign reversal is applied. In the present study the system of equations resulting from the linearization of the governing equations of equilibrium (Eq. 2.50) is solved by factorizing the tangent stiffness matrix in the standard way as $[\mathbf{K}] = [\mathbf{L}][\mathbf{D}][\mathbf{L}]^T$, where $[\mathbf{L}]$ is a lower triangular matrix with diagonal terms as unity and $[\mathbf{D}]$ is a diagonal matrix, the determinant of which gives the determinant of $[\mathbf{K}]$. In most practical problems the determinant turns out to be a very large number which may not be represented using the finite precision of a computer. Hence instead of computing the determinant of $[\mathbf{K}]$, the sign change is determined by determining the number of negative terms in $[\mathbf{D}]$. The determinant is exactly zero at the critical point which could either be a limit point or a bifurcation point. Since the tangent stiffness matrix is singular at the critical point, the solution at the critical point cannot be determined. Based on the author's experience, in most cases the critical point is not exactly reached. When the arc length method is used, the critical point is usually crossed, resulting in a non-positive definite tangent stiffness matrix. In the case of a limit point this does not cause any problems as the solution at the limit point is unique and hence the load deflection path beyond the limit point can be traced by changing the sign of the load parameter as mentioned above, whereas in the case of a bifurcation point the solution is not unique and hence an additional investigation is necessary.

Unlike the case of the limit point, the bifurcation point will have to determined *a priori*. This can be done by monitoring the fundamental frequency of the tangent stiffness matrix. The plot of the fundamental frequency versus the load parameter crosses the load-deflection curve (plot of the deflection at any chosen point on the structure versus the load parameter) at the critical point. Also, in the load-frequency diagram, the load for vanishing frequency defines the critical point. Hence the critical point (limit or bifurcation point) can be anticipated at an earlier stage. After arriving close to the critical point, the solution can be perturbed by adding a small fraction of the mode shape corresponding to the fundamental frequency and then proceed to determine if the secondary branches of the load-deflection path are traced. An easier method would be to add small imperfections to the structure right from the beginning and trace the load-deflection path. Since the load-deflection path of the imperfect structure is asymptotic to the corresponding branch of the perfect structure (depending on the type of the imperfection added), the response of the imperfect structure gives a very good estimate of the secondary branches. The analysis is also less expensive, unlike the analysis of a perfect structure, in which the eigenvalue analysis will have to be performed at almost every load step to determine the critical point.

### 2.3.4 Newton-Raphson method for a thermal load

In the case of a thermal load, the load vector cannot be expressed as $\lambda\ \mathbf{q}_{ref}$ since a thermal load cannot be treated as a proportional load. The Newton-Raphson method for a thermal load is illustrated below. Only the steps required to compute the thermal load vector and the residue are given below since all other steps remain the same.

As in the case of a concentrated load, a known equilibrium configuration is assumed to exist at some instant $t = t_1$. Let $\Delta T = \Delta\lambda_0\ T_{ref}$ be the temperature increment applied to the structure, where $T_{ref}$ is the reference temperature field which at any point $(\xi, \eta, z)$ within the element is given by

$$T_{ref}(\xi,\eta,z) \ = \ \frac{1}{2}\Big(T_u(\xi,\eta)+T_l(\xi,\eta)\Big)+\frac{z}{h}\Big(T_u(\xi,\eta)-T_l(\xi,\eta)\Big) \tag{2.65}$$

where $T_u(\xi,\eta)$ and $T_l(\xi,\eta)$ are the temperatures at the top and bottom surfaces of the laminate, respectively. They are represented in terms of the nodal quantities $T_{u_1}, T_{u_2}, T_{u_3}$ and $T_{l_1}, T_{l_2}, T_{l_3}$ using linear interpolation functions in area coordinates as follows:

$$T_u(\xi,\eta) = T_{u_1} + T_{u_{21}}\xi + T_{u_{31}}\eta \qquad T_l(\xi,\eta) = T_{l_1} + T_{l_{21}}\xi + T_{l_{31}}\eta \tag{2.66}$$

where $T_{u_{21}} = T_{u_2} - T_{u_1},\ \ T_{u_{31}} = T_{u_3} - T_{u_1},\ \ T_{l_{21}} = T_{l_2} - T_{l_1},\ \ T_{l_{31}} = T_{l_3} - T_{l_1}$.

The incremental force and moment resultants due to the applied temperature increment $\Delta T$ are $\{\Delta N^0\}$ and $\{\Delta M^0\}$ as given by Eq. 2.36 ( $\{\Delta N^m\}$ and $\{\Delta M^m\}$ are zero since the incremental displacement vector $\mathbf{a}$ at the beginning of the step is identically zero). The element force vector due to the temperature increment is given by

$$\{\Delta f^0\} = \int_{C_1}\Big([G_2]^T[G_1]^T\{\Delta N^0\}\ +\ [B_{dkt}]^T\{\Delta M^0\}\Big)\,dA \tag{2.67}$$

The matrix $[G_1]$ in Eq. 2.67 consists of only zeroes and ones as the incremental displacement $\mathbf{a}$ at $t = t_1$ is identically zero. The element thermal load vectors $\{\Delta f^0\}$ are assembled in a standard way to obtain the global incremental thermal load vector $\Delta\mathbf{f}^0$. The solution to this incremental step is obtained from $[\mathbf{K}]\ \delta\mathbf{a}\ =\ \Delta\mathbf{f}^0$ and the solution is updated as $\mathbf{a} = \mathbf{a} + \delta\mathbf{a}$ and $\mathbf{a_2} = \mathbf{a_1} + \mathbf{a}$.

In the case of load control the correction to this solution is obtained as before using the residue as $[\mathbf{K}]\ \delta\mathbf{a}\ =\ -\mathbf{g}^0_{t_1+\Delta t}$. The residue $\mathbf{g}^0_{t_1+\Delta t}$ is obtained by assembling the element residual vectors $\{g^0\}$ given by

$$\{g^0\}\ =\ \int_{C_1}\Big([G_2]^T[G_1]^T\{N\}\ +\ [B_{dkt}]^T\{M\}\Big)\,dA \tag{2.68}$$

where $\{N\}$ and $\{M\}$ are given by Eqs. 2.31 and 2.32. The solution is updated as before as $\mathbf{a} = \mathbf{a} + \delta\mathbf{a}$ and $\mathbf{a_2} = \mathbf{a_1} + \mathbf{a}$. The thermal load vector is not used in evaluating the residue as the thermal force and moment resultants are already contained in the expression for $\{N\}$ and $\{M\}$ in Eqs. 2.31 and 2.32.

In the case of arc-length method the correction is obtained as

$$\delta\mathbf{a} = -[\mathbf{K}]^{-1}\ \mathbf{g}^0_{t_1+\Delta t}\ + \delta\lambda\ [\mathbf{K}]^{-1}\ \Delta\mathbf{f}^0 \tag{2.69}$$

where $\delta\lambda$ is determined from the constraint as in the case of a concentrated load and $\Delta\mathbf{f}^0$ is obtained by assembling the element thermal load vectors $\{\Delta f^0\}$ given by Eq. 2.67. The solution at the end of the current iteration is updated as before as $\mathbf{a} = \mathbf{a} + \delta\mathbf{a}$ and $\mathbf{a_2} = \mathbf{a_1} + \mathbf{a}$. The iterations are continued untill the solution converges based on the convergence criterion as mentioned before. In determining the thermal load vector to be used for the corrections $\delta\mathbf{a}$ (Eq. 2.69), the thermal force and moment resultants $\{\Delta N^0\}$ and $\{\Delta M^0\}$ are computed using Eqs. 2.36 with $\Delta T = T_{ref}$, unlike the case of the incremental step where the thermal force and moment resultants are determined using $\Delta T = \Delta\lambda_0 T_{ref}$. It should also be noted that the matrix $[G_1]$ that will be used in computing the thermal load used in Eq. 2.69 will be a function of the displacements $\mathbf{a}$ as given by 2.39. Since the thermal load depends on the displacements, it contributes to the tangent stiffness matrix. By comparing Eqs. 2.49 and 2.67, it is obvious that the contribution to the tangent stiffness matrix due to the variation of the thermal load with displacement is similar to the initial stress matrix, which is the last term in Eq. 2.54. No additional effort is needed to determine this contribution as the thermal force resultants are already included in the expressions for $\{N\}$ and $\{M\}$ in Eqs. 2.31 and 2.32.

### 2.3.5 Newton-Raphson method for a pressure load

The pressure load is always assumed to act normal to the current or deformed configuration of the structure. Hence the direction of the pressure load continuously changes as the structure deforms and this is referred to as the follower action. Since the pressure load is a function of the displacements, it contributes to the tangent stiffness matrix and this contribution, called the pressure stiffness matrix, is in general unsymmetric. In practice a symmetric form defined as the average of the pressure stiffness and its transpose is employed. The contribution to the tangent stiffness matrix due to the follower effect, called the pressure stiffness should be taken into account, especially in the case of large deformation analysis. Neglecting the pressure stiffness might seriously affect the convergence of the solution even when the deformations are small and in the case of large deformations the solution may not converge at all.

Unlike the case of the thermal load, the determination of the pressure stiffness is not straightforward. The pressure load and the pressure stiffness can be systematically derived from the principle of virtual work. The virtual work due to the pressure load in a local coordinate system is given by

$$\delta W_p \;=\; \int \{\delta u \;\delta v \;\delta w\}\; P\; d\bar{\mathbf{A}} \tag{2.70}$$

where $\delta u, \delta v$ and $\delta w$ are the virtual displacements of the midplane of the element, $d\bar{\mathbf{A}}$ is the area vector normal to the deformed configuration and $P$ is the total pressure acting normal to the element in the deformed configuration and is represented using a linear interpolation in area coordinates as

$$P(\xi,\eta) \;=\; \lambda\;(P_{1_{ref}}(1-\xi-\eta) \;+\; P_{2_{ref}}\xi \;+\; P_{3_{ref}}\eta) \tag{2.71}$$

where $P_{1_{ref}}, P_{2_{ref}}$ and $P_{3_{ref}}$ are the nodal values obtained from a reference pressure distribution to which the structure is subjected to and $\lambda$ is the load proportionality factor. The pressure distribution could either be space attached in which the distribution of the magnitude is a function of the coordinates in the deformed configuration, or body attached in which it is a function of the coordinates in the undeformed initial configuration. A positive sign is used for the nodal pressure if the pressure acts in the same direction as the outward normal to the current/deformed surface (internal pressure) and a negative sign is used for the nodal pressure if the pressure acts opposite to the outward normal to the current/deformed surface (external pressure).

In the updated Lagrangian formulation, all quantities are measured with respect to the reference configuration $C_1$ which is a known equilibrium configuration. Hence the area vector in the deformed configuration $d\bar{\mathbf{A}}$ has to be expressed in the reference configuration. This is achieved using the relation given by Malvern [71] as

$$d\bar{\mathbf{A}} \;=\; [F^{-1}]^T\{\bar{n}\}\; dA \tag{2.72}$$

where $[F]$ is the deformation gradient tensor, $\{\bar{n}\}$ is the normal to the midplane of the element in $C_1$ and $dA$ is the magnitude of an area element in $C_1$. The deformation gradient tensor is given by

$$[F] = \begin{bmatrix} 1+U_x & U_y & U_z \\ V_x & 1+V_y & V_z \\ W_x & W_y & 1+W_z \end{bmatrix} \tag{2.73}$$

where

$$\begin{aligned} U(x,y,z) &= u(x,y) + z\beta_x(x,y) \\ V(x,y,z) &= v(x,y) + z\beta_y(x,y) \\ W(x,y,z) &= w(x,y) \end{aligned} \tag{2.74}$$

where $u, v$ and $w$ are the displacements of the mid-plane of the element along the local $x, y$ and $z$ axes, respectively, and $\beta_x, \beta_y$ are the rotations of the shell normal about the local $y$ and $x$ axes, respectively.

Since the structures under consideration are very thin and most of the deformation of the element is comprised of rigid body rotations, the contribution to the deformation gradient tensor by the normal rotations $\beta_x$ and $\beta_y$ can be neglected and a linear interpolation for $u, v$ and $w$ can be used. The deformation gradient tensor can now be simplified as

$$[F] = \begin{bmatrix} 1+u_{,x} & u_{,y} & 0 \\ v_{,x} & 1+v_{,y} & 0 \\ w_{,x} & w_{,y} & 1 \end{bmatrix} \tag{2.75}$$

Since the normal to the mid-plane of the element in $C_1$ coincides with the local z-axis, $\{\bar{n}\} = \{0, 0, 1\}$. The area vector normal to the deformed configuration can now be expressed in the reference configuration as

$$d\bar{\mathbf{A}} = \begin{Bmatrix} v_{,x}w_{,y} - w_{,x}(1+v_{,y}) \\ u_{,y}w_{,x} - w_{,y}(1+u_{,x}) \\ (1+u_{,x})(1+v_{,y}) - u_{,y}v_{,x} \end{Bmatrix} dA \tag{2.76}$$

The mid-plane displacements $u, v$ and $w$ can be expressed in terms of the nodal values using linear interpolation functions in area coordinates as

$$\begin{aligned} u &= (1-\xi-\eta)u_1 + \xi u_2 + \eta u_3 \\ v &= (1-\xi-\eta)v_1 + \xi v_2 + \eta v_3 \\ w &= (1-\xi-\eta)w_1 + \xi w_2 + \eta w_3 \end{aligned} \tag{2.77}$$

The variation of the mid-plane displacements can be expressed as

$$\{\delta u \; \delta v \; \delta w\}^T = [G_3][T]\{\delta a\} \tag{2.78}$$

where

$$[G_3] \;=\; \begin{bmatrix} 1-\xi-\eta & 0 & 0 & \xi & 0 & 0 & \eta & 0 & 0 \\ 0 & 1-\xi-\eta & 0 & 0 & \xi & 0 & 0 & \eta & 0 \\ 0 & 0 & 1-\xi-\eta & 0 & 0 & \xi & 0 & 0 & \eta \end{bmatrix} \tag{2.79}$$

The transformation matrix $[T]$ which is used to express the vector of nodal displacements $\{u_1, v_1, w_1, u_2, v_2, w_2, u_3, v_3, w_3\}$ in terms of the vector of nodal degrees of freedom of the shell element $\{a\}$ is comprised of zeroes and ones, the determination of which is straightforward. The virtual work due to the pressure load can now be expressed as

$$\delta W_p \;=\; \{\delta a\}^T\{f_p\} \tag{2.80}$$

where $\{f_p\}$ is the pressure load vector in the local coordinate system given by

$$\{f_p\} \;=\; \int_0^1 \int_-^{1-\eta} [T]^T[G_3]^T P \left\{ \begin{array}{c} v_{,x}w_{,y} - w_{,x}(1+v_{,y}) \\ u_{,y}w_{,x} - w_{,y}(1+u_{,x}) \\ (1+u_{,x})(1+v_{,y}) - u_{,y}v_{,x} \end{array} \right\} 2A \; d\xi d\eta \tag{2.81}$$

where $A$ is the area of the mid-plane of the element in $C_1$. The partial derivatives of the mid-plane displacements in Eq. 2.81, which are constants, are easily obtained from the linear interpolation field as

$$\{\, u_{,x} \quad u_{,y} \quad v_{,x} \quad v_{,y} \quad w_{,x} \quad w_{,y} \,\}^T = \frac{1}{2A}[G_4][T]\{a\} \tag{2.82}$$

where

$$[G_4] \;=\; \begin{bmatrix} -b_2-b_3 & 0 & 0 & b_2 & 0 & 0 & b_3 & 0 & 0 \\ -c_2-c_3 & 0 & 0 & c_2 & 0 & 0 & c_3 & 0 & 0 \\ 0 & -b_2-b_3 & 0 & 0 & b_2 & 0 & 0 & b_3 & 0 \\ 0 & -c_2-c_3 & 0 & 0 & c_2 & 0 & 0 & c_3 & 0 \\ 0 & 0 & -b_2-b_3 & 0 & 0 & b_2 & 0 & 0 & b_3 \\ 0 & 0 & -c_2-c_3 & 0 & 0 & c_2 & 0 & 0 & c_3 \end{bmatrix} \tag{2.83}$$

where $b_i = y_j - y_k$, $c_i = x_k - x_j$ and $i, j, k$ take cyclically values 1,2,3. The pressure stiffness $[k_p]$ is obtained by taking the derivative of $\{f_p\}$ with respect to $\{a\}$ using the standard chain rule $\delta(\;) = (\partial(\;)/\partial\{a\})\delta\{a\}$ or in other words

$$\{\delta f_p\} \;=\; (\partial\{f_p\}/\partial\{a\})\{\delta a\} \;=\; [k_p]\{\delta a\} \tag{2.84}$$

After straightforward manipulations the pressure stiffness matrix can be expressed as

$$[k_p] \ = \ \int_0^1 \int_0^{1-\eta} [T]^T [G_3]^T P [G_5][G_4][T] \ d\xi d\eta \tag{2.85}$$

where

$$[G_5] \ = \ \begin{bmatrix} 0 & 0 & w_{,y} & -w_{,x} & -(1+v_{,y}) & v_{,x} \\ -w_{,y} & w_{,x} & 0 & 0 & u_{,y} & -(1+u_{,x}) \\ 1+v_{,y} & -v_{,x} & -u_{,y} & 1+u_{,x} & 0 & 0 \end{bmatrix} \tag{2.86}$$

The area integrals in Eqs. 2.81 and 2.85 are performed using the standard three-point rule in area coordinates. As can be seen from Eq. 2.85, the pressure stiffness matrix is unsymmetric. In the present study the pressure stiffness matrix is not split into interior and boundary parts. A symmetric form defined as $(1/2)([k_p] + [k_p]^T)$ is employed. The pressure load $\mathbf{f}^p$ and the pressure stiffness $[\mathbf{K}_p]$ in global Cartesian coordinates are obtained by assembling the element load vectors given by Eq. 2.81 and the element stiffness matrix given by Eq. 2.85 in the standard way. The pressure stiffness matrix is subtracted from the tangent stiffness matrix (Eq. 2.54).

As in the case of mechanical load, a known equilibrium configuration is assumed to exist at some instant $t = t_1$. Let $\lambda_1$ be the load proportionality factor at $t = t_1$ and $\Delta\lambda_0$ be the incremental load proportionality factor at $t = t_1$. The incremental pressure load $\Delta\mathbf{f}^p$ acting on the current configuration (which at time $t = t_1$ is $C_1$) is obtained by assembling the element pressure load vectors $\{f^p\}$ given by Eq. 2.81, using the load proportionality factor $\lambda = \Delta\lambda_0$ in Eq. 2.71. The solution to this incremental step is obtained as before from $[\mathbf{K}] \ \delta\mathbf{a} = \Delta\mathbf{f}^p$ and the solution is updated as $\mathbf{a} = \mathbf{a} + \delta\mathbf{a}$ and $\mathbf{a_2} = \mathbf{a_1} + \mathbf{a}$. It should be noted that for the incremental step the pressure stiffness is not included as the pressure load is not a function of displacement (since $\mathbf{a} = 0$ at $t = t_1$).

In the case of load control the correction to this solution is obtained as before using the residue as $[\mathbf{K}] \ \delta\mathbf{a} = -\mathbf{g}^p_{t_1+\Delta t}$. Here the pressure stiffness matrix is included in $[\mathbf{K}]$. The residue $\mathbf{g}^p_{t_1+\Delta t}$ is obtained by assembling the element residual vectors $\{g^p\}$ given by

$$\{g^p\} \ = \ \{q\} \ - \ \{f^p\} \tag{2.87}$$

where $\{q\}$ is the element internal force vector given by Eq. 2.49 (considering only mechanical stresses) and $\{f^p\}$ is given by Eq. 2.81. In computing $\{f^p\}$, the current load proportionality factor is used in Eq. 2.71, which is $\lambda_1 + \Delta\lambda_0$. The solution is updated as before as $\mathbf{a} = \mathbf{a} + \delta\mathbf{a}$ and $\mathbf{a_2} = \mathbf{a_1} + \mathbf{a}$.

In the case of the arc length method, the correction is obtained as

$$\delta\mathbf{a} = -[\mathbf{K}]^{-1}\,\mathbf{g}^{p}_{t_1+\Delta t} \;+ \delta\lambda\,[\mathbf{K}]^{-1}\,\Delta\mathbf{f}^{p} \tag{2.88}$$

where $\delta\lambda$ is determined from the constraint as in the case of a concentrated load. The solution at the end of the current iteration is updated as before as $\mathbf{a} = \mathbf{u} + \delta\mathbf{u}$ and $\mathbf{a_2} = \mathbf{a_1} + \mathbf{u}$. The iterations are continued until the solution converges based on the convergence criterion as mentioned before. The pressure load $\Delta\mathbf{f}^{p}$ in Eq. 2.88 is obtained using $\lambda = 1$ in Eq. 2.71 unlike the case of the incremental step where $\lambda = \Delta\lambda_0$. The pressure load used in the residue (Eq. 2.87) is determined using the current load proportionality factor $\lambda_1 + \Delta\lambda_0$ at the end of the incremental step or $\lambda_1 + \Delta\lambda_0 + \delta\lambda$ at the end of an iteration.

### 2.3.6 Dynamic analysis

As in the case of static analysis, it is assumed that a known equilibrium configuration exists at some time $t_1$ and the solution at some time $t_1+\Delta t$ has to be determined. The equations of equilibrium governing the dynamic response of a structure at time $t_1 + \Delta t$ can be expressed as

$$[\mathbf{M}]\ddot{\mathbf{a}}_{t_1+\Delta t} \;+\; \mathbf{q}_{t_1+\Delta t} \;=\; \mathbf{f}_{t_1+\Delta t} \tag{2.89}$$

where $\mathbf{M}$ is the mass matrix, $\mathbf{q}$ is the internal force and $\mathbf{f}$ is the externally applied force.

Since the transverse displacement is not defined explicitly at the interior of the DKT element, the determination of a consistent mass matrix is not possible. This problem is alleviated by using a lumped mass matrix which is obtained by assigning one-third of the total mass of the element to each of the translational degrees of freedom at each node. The rotational inertias are neglected in computing the lumped mass matrix. It is well known that the natural frequencies obtained using a lumped mass converge from below. A fine mesh is required in order to obtain the the eigenvalues of a large number of modes and hence the analysis is computationally expensive. In the present study a so called consistent mass matrix is also employed in order to compare the performance of the two types of mass matrices. A 9x9 mass matrix corresponding to the degrees of freedom of the DKT element is obtained using the shape functions in area coordinates proposed by Specht [37] for the transverse displacement. A 12x12 mass matrix corresponding to the degrees of freedom of the LST element is obtained using the same shape functions that are used for the in-plane displacements in the LST element. The 9x9 mass matrix corresponding to the degrees of freedom of the membrane element is obtained by applying the transformation given by Cook [5] to the 12x12 mass matrix of the LST element derived as mentioned above. A three point integration scheme in area coordinates (Yang [2]) is used to determine the elements of the mass matrix. The element mass matrices thus obtained in a local coordinate system are transformed to the global Cartesian coordinate system prior to their assembly into the global mass matrix $[M]$. Details of derivation of the mass matrices are not repoduced here as it is well documented in the existing literature. The frequencies of free vibration and the mode shapes are obtained by solving the eigenvalue problem given by

$$\Big|[\mathbf{K}] - \omega^{\mathbf{2}}[\mathbf{M}]\Big| = 0 \tag{2.90}$$

where $[\mathbf{K}]$ is the linear stiffness matrix obtained from Eq. 2.54 by neglecting the initial stress matrix and the terms dependent on displacements. The eigenvalue problem given by Eq. 2.90 is solved using the subspace iteration method, which is described in detail by Bathe [79]. The non-linear governing equations of dynamic equilibrium given by Eq. 2.89 are solved using the Newmark time integration method in conjunction with the Newton-Raphson method, using the algorithm given by Bathe and Ramm [80].

# Chapter 3

# Numerical examples

A large set of problems on linear static analysis, free vibration analysis, linear thermal analysis and geometrically nonlinear analysis was solved in order to demonstrate the accuracy of the present flat shell formulation, and the results are presented in this chapter in different sections. The present results are compared with those available in the existing literature whereever applicable and with those obtained using the STRI3, S4R and S4R5 elements of the commercial finite element package ABAQUS using the same solution procedure and convergence criterion. STRI3 is a three-noded flat shell element obtained by combining the DKT plate bending element and the CST element. S4R is a four-noded doubly curved shell element with reduced integration, applicable for both thick and thin shell. S4R5 is also a four-noded double curved shell element with reduced integration, but is applicable only for thin shells.

## 3.1 Linear Static Analysis

Static analysis of simply supported square plates under a doubly sinusoidal load $P_0\ sin(\pi x/a) sin(\pi y/a)$ and simply supported spherical shells with square base under a uniformly distributed load of intensity $P_0$ were performed. Both symmetric and unsymmetric laminates were considered for the analysis. In all cases the layers constituting the laminate were assumed to be of equal thickness. Unless mentioned otherwise, for the square plates $h/a = 0.01$ where $a$ is the side and $h$ is the thickness of the plate, and for the spherical shells $h/a = 0.01, r/a = 10$ where $a$ is the side of the square base, $h$ is the thickness and $r$ is

the radius of curvature. The following types of boundary conditions and material properties were used for the numerical examples presented.
BC1: $v = w = \theta_x = 0$ at $x = 0, a$ and $u = w = \theta_y = 0$ at $y = 0, b$
BC2: $u = w = \theta_x = 0$ at $x = 0, a$ and $v = w = \theta_y = 0$ at $y = 0, b$
MAT1: $E_1 = 25E_2$ , $G_{12} = 0.5E_2$ , $\nu_{12} = 0.25$
MAT2: $E_1 = 40E_2$ , $G_{12} = 0.6E_2$ , $\nu_{12} = 0.25$

*Simply supported [0/90/90/0] square plate:* One quadrant of the plate under a doubly sinusoidal load was analyzed with boundary conditions BC1 and material properties MAT1. The convergence of non-dimensionalized mid-deflection is given in Table 3.1 along with the closed form solution as given by Phan and Reddy [81].

*Simply supported [-45/45] square plate:* A full plate under a doubly sinusoidal load was analyzed with boundary conditions BC2 and material properties MAT2. The convergence of non-dimensionalized maximum displacements $w* = w_{max}E_2h^3 10^2/P_o a^4$, $u* = u_{max}E_2h^3 10^4/P_o a^4$ and $v* = v_{max}E_2h^3 10^4/P_o a^4$ is given in Table 3.2 along with the analytical solution computed using equations 39-44 of Whitney and Leissa [82].

*Scordelis-Lo roof:* The geometry, material properties and the boundary conditions used are shown in Fig. 3.1. One quadrant of the roof under selfweight was analyzed. The convergence of the vertical downward deflection at the mid-point of the free edge is given in Table 3.3 along with the results of Chen [59] (DKT + 4 point integrated higher order membrane element of Allman [4] ), Carpenter *et al.* [10] (DKT + one point integrated quadratic membrane element of Allman [3]) and those obtained using STRI3. The exact value of the vertical downward deflection at the mid-point of the free edge as quoted by Carpenter *et al.* [10] is 0.3024.

*Pinched cylinder:* The geometry, material properties and the boundary conditions used are shown in Fig. 3.2. One quadrant of the cylinder under a concentrated mid-load (as shown in Fig. 3.2) was analyzed. The convergence of the vertical downward deflection at the load point is given in Table 3.4 along with the results of Chen [59], Carpenter *et al.* [10] and those obtained using STRI3. The exact value of the vertical downward downward deflection at the load point as quoted by Carpenter *et al.* [10] is 1.8248 x $10^{-5}$.

*Hemispherical shell with a hole:* The geometry, material properties and the boundary conditions used are shown in Fig. 3.3. One quadrant of the cylinder under diametrically opposite pinching and stretching loads (as shown in Fig. 3.3) was analyzed. The boundary conditions as shown in Fig. 3.3 (and as given in the literature) do not inhibit the rigid body vertical translation of the shell. Analysis was performed both with a free hole and with the vertical displacement constrained along the hole. The convergence of the radial deflection at A, in the direction of the load, and the vertical deflection at A, are given in Tables 3.5 and 3.6 respectively, for the case with a free hole, along with the results of Chen [59] and those obtained using the STRI3 element of ABAQUS. The corresponding results for the case with the vertical displacement constrained along the hole are given in Tables 3.7 and 3.8. The results of Carpenter *et al*. [10] are not compared since their results correspond to a hemispherical shell without a hole. The exact value of the radial deflection under the load for the shell without a hole as quoted by MacNeal and Harder [83] is 0.0924. To the best of the author's knowledge the exact solution for the shell with a hole is not available in the existing literature.

*Simply supported spherical shell:* The full shell under a uniformly distributed load was analyzed with boundary conditions BC1 and material properties MAT1. The convergence of non-dimensionalized mid deflection for two stacking sequences, [0/90] and [0/90/90/0] is given in Table 3.9 along with the exact solution as given by Reddy [84].

The results for linear static analysis converged from below and to within 1 % of the exact solution or finite element solution available in the existing literature. The three shell problems, namely, Scordelis-Lo roof, pinched cylinder and the hemispherical shell have been widely used in the existing literature as standard problems to test the accuracy of the finite element formulations. Hence a discussion on the performance of the present formulation in the case of these three problems is warranted here.

In the case of the Scordelis-Lo roof, the convergence of the present results is less rapid compared to that of the underintegrated Allman element of Carpenter *et al*. [10] and the higher order Allman element of Chen [59], but the same accuracy is obtained using a finer mesh without the need for the additional effort that is required to suppress the spurious zero energy modes as in the case of the underintegrated element. Since the Allman element used in the present formulation is quadratic, the present analysis is expected to be computationally less expensive compared to that using the higher order Allman element, especially in the case of non-linear analysis.

In the case of the pinched cylinder, the present results appear to converge towards the exact solution, whereas both the underintegrated Allman element used by Carpenter *et al.* [10] and the higher order Allman element used by Chen [59] give over soft solutions. The STRI3 element appeared to converge towards the exact solution less rapidly compared to the present results.

It has been well established in the existing literature that the fully integrated Allman element (quadratic membrane element of Allman [3]) exhibits very poor rate convergence and that the CST element outperforms the fully integrated Allman element in the case of the hemispherical shell under diametrically opposite pinching and stretching loads. This can be clearly seen from the results presented in Table 3.5. The 4-point integrated higher order membrane element used by Chen [59] performs better than the present element, but the convergence is not as rapid as in the case of the CST element.

The boundary conditions for this problem as given by MacNeal and Harder [83] and Chen [59] do not suppress the rigid body vertical translation of the entire shell. As can be seen from Table 3.6, the vertical deflection at point A does not show any sign of convergence. This can be attributed mainly to the fact that the rigid body motion of the shell is not completely restrained. Though the stiffness matrix may not be singular, it could be ill conditioned, giving incorrect results. When the vertical deflection along the hole was suppressed, the present results and those obtained using STRI3 and S4R converged to more or less the same value for both the radial and vertical deflection at point A, but the rate of convergence of the present results is less rapid compared to that of STRI3. The reason for better performance of the CST element for this problem alone is not quite clear.

## 3.2 Free Vibration Analysis

Free vibration analysis of square cantilever plates, skew cantilever plates and simply supported spherical shells was performed. Both symmetric and unsymmetric laminates were considered for analysis. In all cases layers constituting the laminates were assumed to be of equal thickness.

*Eight layer [0/45/-45/90/90/-45/45/0] cantilever plate:* The material properties used are: $E_1 = 128\ GPa$, $E_2 = 11\ GPa$, $\nu_{12} = 0.25$, $G_{12} = 4.48\ GPa$, density = 1500 $kg/m^3$. Plate dimensions are 0.0762 $m$ x 0.0762 $m$ x 0.00105664 $m$. The convergence of the first five natural frequencies (Hz) are given in Tables 3.10 and 3.11 for lumped and consistent mass matrices respectively, along with the Ritz solution obtained by Kapania and Singhvi [85]. The mode shapes obtained using the consistent mass matrix are shown in Fig 3.5.

*Two-layer [0/22.5] square cantilever plate:* The material properties used are: $E_1 = 161.21\ GPa$, $E_2 = 12.52\ GPa$, $\nu_{12} = 0.22$, $G_{12} = 6.75\ GPa$, density = 1881.81 $kg/m^3$. Plate dimensions are 0.2032 $m$ x 0.2032 $m$ x 0.00124968 $m$. The convergence of the first five natural frequencies (Hz) is given in Tables 3.12 and 3.13 for lumped and consistent mass matrices, respectively, along with the Ritz solution obtained by Kapania and Singhvi [85]. The mode shapes obtained using the consistent mass matrix are shown in Fig. 3.6.

*Six layer* $[15_2/0]_s$ *skew cantilever plate :* The geometry of the skew cantilever plate is shown in Fig. 3.4. The material properties used are: $E_1 = 38.61\ GPa$, $E_2 = 8.27\ GPa$, $\nu = 0.26$, $G_{12} = 4.14\ GPa$, density=2546.54 $kg/m^3$. The geometric parameters are aspect ratio=2.333, taper ratio=0.5, area=0.04064508 $m^2$, thickness=0.003556 $m$. The sweep angle $\beta$ of the quarterchord line as shown in Fig. 3.4 is $30^o$. The aspect ratio is defined as the ratio of length to the width at the root. The taper ratio is defined as the ratio of width at the tip to the width at the root. The fiber angle is measured counterclockwise from the quarterchord line. For example a 2-ply laminate [0/45] has fibers along the quarterchord line in one layer and at 45 degrees counter clock wise from the quarterchord line in the other layer. The convergence of the first five natural frequencies (Hz) is given in Tables 3.14 and 3.15 for lumped and consistent mass matrices, respectively, along with the Ritz solution obtained by Kapania and Singhvi [85]. The mode shapes obtained using the consistent mass matrix are shown in Fig. 3.7.

*Two-layer [0/22.5] skew cantilever plate:* The material properties used are, $E_1 = 161.21\ GPa$, $E_2 = 12.52\ GPa$, $\nu = 0.22$, $G_{12} = 6.75\ GPa$, density=1881.81 $kg/m^3$. The geometric parameters are $\beta = 45$, aspect ratio=1, taper ratio=1, area=0.04129024 $m^2$, thickness=0.00124968 $m$. The convergence of the five natural frequencies (Hz) are given in Tables 3.16 and 3.17 for lumped and consistent mass matrices respectively, along with the Ritz solution obtained by Kapania and Singhvi [85]. The mode shapes obtained using the consistent mass matrix are shown in Fig. 3.8.

*Simply supported [0/90/90/0] spherical shell:* The material and geometric properties used are: $E_1 = 25E_2$, $G_{12} = 0.5E_2$, $\nu_{12} =$ 0.25, $a/h = 100$, $r/a = 10$. The full shell was analyzed with boundary conditions as in the static analysis. The convergence of first five non-dimensional frequencies $(\omega a^2\sqrt{\rho/E_2}/h)$ is shown in Tables 3.18 and 3.19 for lumped and consistent mass matrices respectively. The exact value for the non-dimensionalized fundamental frequency as given by Reddy [84] is 20.38. The mode shapes obtained using the consistent mass matrix are shown in Fig. 3.9.

The natural frequencies obtained using the lumped mass matrix converged from below for the plate problems. No regular trend was observed in the case of shells and with the results obtained using the consistent mass matrix. The rate of convergence of the frequencies obtained using the consistent mass matrix was very rapid compared to that obtained using the lumped mass matrix, except in the case of the spherical shells for which the rate of convergence of the frequencies obtained by both approaches was more or less equal. The results obtained using both approaches are in good agreement with each other and with those of Kapania and Singhvi [85] except for the higher modes in the case of symmetrically laminated square plates. There is a lot of disparity among the free vibration results by different authors, as stated by Kapania and Singhvi [85]. Since exact solutions are not available, nothing can be said about the accuracy of the results available in the existing literature. However, the consistent mass approach adopted here seems far more economical than the lumped mass approach, especially when a large number of modes is required to be extracted.

## 3.3 Linear Thermal Analysis

Thermal analysis of square plates and spherical shells with a square base was performed. Symmetric and unsymmetric laminates under a uniform thermal field and a non-uniform thermal field with a linear variation of temperature across the thickness were considered. For both uniform and non-uniform temperature distributions, the top surface of the laminate is assumed to be at a constant temperature of $T_u\ ^o\ C$ and the bottom surface at a constant temperature of $T_l\ ^o\ C$. The geometric parameters used are $h/a = 0.01$ for square plates and $h/a = 0.01, r/a = 10$ for spherical shells. The following boundary conditions and material properties were used for the numerical problems presented:

BC1: $v = w = \theta_x = 0$ at $x = 0, a$ and $u = w = \theta_y = 0$ at $y = 0, b$
BC2: $u = w = \theta_x = 0$ at $x = 0, a$ and $v = w = \theta_y = 0$ at $y = 0, b$
Material properties: $E_1 = 53.8\ GPa$, $E_2 = 17.9\ GPa$, $G_{12} = 8.62\ GPa$, $\nu_{12} = 0.25$, $\alpha_1 = 6.3\text{x}10^{-6}/^oC$, $\alpha_2 = 20.5\text{x}10^{-6}/^oC$, $\alpha_{12} = 0$

The results obtained for simply supported, symmetric, specially orthotropic plates and antisymmetric cross-ply and angle-ply laminated plates are compared with the series solution presented by Wu and Tauchert [86] & [87]. A convergence study was first performed in order to determine the number of terms to be used for the series solution. The convergence history showed that the convergence of the in-plane displacements was very slow compared to the rapid convergence of the transverse displacement. In the numerical examples presented below, the mid-deflection $w_{max}$ and the maximum in-plane displacements $u_{max}$ and $v_{max}$ obtained using the present finite element formulation are compared with the series solution of Wu and Tauchert [86] & [87] obtained using 100 terms in the case of $w_{max}$ of symmetric specially orthotropic laminates and 10000 terms (100x100) in the case of $u_{max}$ and $v_{max}$ of symmetric specially orthotropic laminates and $u_{max}, v_{max}$ and $w_{max}$ of antisymmetric cross-ply and angle-ply laminates.

*Simply supported [0/90/90/0] square plate (BC1):* The convergence of $w_{max}$ due to a linearly varying thermal field ($T_u = 1, T_l = -1$) and $u_{max}, v_{max}$ due to a uniform thermal field ($T_u = 1, T_l = 1$) are given in Table 3.20 along with the series solution of Wu and Tauchert [86] & [87].

*Simply supported [0/90/0/90] square plate (BC1):* The convergence of $u_{max}, v_{max}$ and $w_{max}$ due to a non-uniform thermal field ($T_u = 1, T_l = 0$) are given in Table 3.21 along with the series solution of Wu and Tauchert [86] & [87].

*Simply supported* $[15/-15/15/-15]$ *square plate (BC2):* The convergence of $u_{max}, v_{max}$ and $w_{max}$ due to a non-uniform thermal field ($T_u = 1, T_l = 0$) are given in Table 3.22 along with the series solution of Wu and Tauchert [86] & [87].

*Simply supported spherical shell (BC1):* The convergence of $u_{max}, v_{max}$ and $w_{max}$ due to a non-uniform thermal field ($T_u = 1, T_l = 0$) for cross-ply and angle-ply laminates is given in Tables 3.23 and 3.24, respectively. The results could not be compared as exact solutions or finite element results for thermal deformation of thin shells are not available in the existing literature to the best of the author's knowledge.

The thermal deformations converged from below in the case of plates. In the case of shells the transverse deformations converged from above. No regular trend was noticed in the case of in-plane displacements. The present results (in the case of plate problems) are in good agreement with the results available in the existing literature.

## 3.4 Geometrically Nonlinear Analysis

### 3.4.1 Static response analysis

*Two layer [45/-45] hinged cylindrical panel:* The geometry, material properties and the boundary conditions used are given in Fig. 3.10. One quarter of the panel under a concentrated load of 1600 N was analyzed. The present results are compared with those obtained using STRI3 and S4R elements in Fig. 3.11. The load -deflection curve was traced using the standard arc-length control method. Very small increments have been used in order to obtain a very smooth load-deflection curve. Only a few points are shown in the figure. It was possible to perform the analysis using very large load steps since the rotations are very small.

*Cantilever beam under a tip moment* : The geometry and material properties used are: Length = 10 $m$, width = 1 $m$, thickness = 0.1 $m$, E = 1.2x$10^8 N/m^2$, $\nu = 0$. The applied bending moment ($2000\pi$ Nm) at the tip causes the beam to deform into a full circle. In Fig. 3.12 the present results, obtained using load-control in 50 steps and a total of 200 iterations, are compared with those obtained using the STRI3, S4R5 and S4R elements. The present results are in good agreement with those obtained using STRI3 and S4R elements. The results obtained using the S4R5 element show a slight deviation from the rest of the results for 4200 < M < 6000 Nm.

*Clamped cylindrical shell under pinching loads at the apex*: The geometry and material properties used are: Length = 3.048 $m$, Radius = 1.016 $m$, thickness = 0.03 $m$, E = 2.0685 x $10^7 N/m^2$ and $\nu = 0.3$. One quarter of the shell, with the boundary conditions as shown in Fig. 3.13, was analyzed under a concentrated apex load. The analysis was performed until the deflection under the load was just about equal to the radius of the cylinder. The load-deflection path was traced using arc length control in 32 increments with a total of 120 iterations. Though the response does not show any instabilities, arc length control has been used because the convergence is faster in the case of arc length control than load control. In Fig. 3.13 the present results are compared with those obtained using STRI3, S4R and those of Brank *et al.* [57]. The STRI3 element showed severe convergence problem for P $>$ 500 N when load control was used. Though large load increments could be used up to P = 500 N, the load increments were automatically cut down for P $>$ 500 N resulting in at least 100 steps. When arc length control was used, the STRI3 element showed extreme sensitivity to the size of the arc-length increments. Only the results obtained using the arc-length control are presented in the case of the STRI3 element. The flat shell element of the present study and S4R did not show such problems. As can be seen from Fig. 3.13, the results obtained using the STRI3 element in 37 increments do not agree well with the rest of the results. The present results agree well with those of Brank *et al.* [57], S4R and STRI3 (obtained using 90 increments).

*Cylindrical shell with free ends under stretching loads at the apex*: The geometry and the material properties used are: Radius = 4.953 $m$, Length = 10.35 $m$, thickness = 0.094 $m$, E = 10.5 x $10^3 N/m^2$ and $\nu = 0.3125$. One quarter of the shell, with the boundary conditions as shown in Fig. 3.14, was analyzed under stretching loads at the apex. Two distinct zones of stiff and soft behavior can be identified from the load deflection curve (3.14). Most of the results in the existing literature show good agreement only in the soft zone. In 3.14 the present results, obtained using arc-length control in 25 steps with a total of 95 iterations, are compared with those of Brank *et al.* [57] and those obtained using the S4R and S4R5 elements of ABAQUS. The present results are in good agreement with those of Brank *et al.* [57] and S4R in both the stiff and soft zones. The S4R5 element failed to proceed in the same direction for P $>$ 32 N.

*Hemispherical shell with a hole under pinching and stretching loads:* The geometry, material properties and the boundary conditions used are the same as those used in the linear analysis. The non-linear analysis was performed with the transverse deflection constrained along the hole in order to prevent the rigid body motion which otherwise is not suppressed by the symmetry conditions shown in Fig. 3.3. The present results obtained using the arc-length control in 22 steps with a total of 88 iterations are compared with those of Buechter and Ramm [88] and those obtained using STRI3 and S4R elements in Figures 3.15 and 3.16. The present results are in good agreement with those of Buechter and Ramm [88] and S4R.

The results obtained using the STRI3 element for the transverse displacement Fig. 3.16 do not agree well with the present results and those obtained using S4R.

*Ring plate under a line load at the free edge*: The geometry (Fig. 3.17) and material properties used are: inner radius = 8 $m$, outer radius = 10 $m$, thickness = 0.03, E = 2.1 x $10^8 N/m^2$ and $\nu = 0.0$. The plate is clamped at one of the edges which meet along the line AB (Fig. 3.17) and subjected to a line load at the other edge. The present results obtained using arc-length control in 44 steps and 223 iterations are compared with those of Buechter and Ramm [88] and those obtained using the S4R and STRI3 elements in Fig. 3.17 and are in good agreement. As in the case of the pinched cylindrical shell, the STRI3 element showed some convergence problems. Though large initial increments were used (in arc-length control) the increments were cut down several times during the course of the analysis resulting in 242 increments with a total of 1199 iterations. The total number of iterations used in the case of the present formulation or S4R is smaller than the total number of increments used in the case of the STRI3 elements.

### 3.4.2 Dynamic response analysis

The dynamic response analysis of an antisymmetric angle ply laminated ([45/-45]) hinged cylindrical panel of thickness 0.0126 $m$ under a centrally applied load of 1600N was performed. The geometry and material properties used are the same as those used in the static response analysis. The density and time step used are 1000 $kg/m^3$ and 0.5x$10^{-3} sec.$ respectively. The force was applied at time $t = 0$ and held constant. The results obtained using the present formulation are compared with those obtained using the STRI3 and S4R element (using the same time step) in Fig. 3.18 and are in good agreement.

### 3.4.3 Thermal postbuckling analysis

The thermal postbuckling analysis of a simply supported symmetrically laminated imperfect square plate and an antisymmetric angle ply laminated clamped cylindrical panel subject to a uniform temperature rise were performed. The material properties used for the plate are $E_1 = 155Gpa, E_2 = 8.07Gpa, \nu_{12} = 0.22$ and $G_{12} = 4.55Gpa$. The plate dimensions are 0.15x0.15x0.001016 $m$ and the imperfections considered are in the form of the first buckling mode. The bifurcation behavior of the perfect plate at the critical temperature was simulated by adding a very small amount of imperfection, with a maximum magnitude of 0.0005 times the thickness of the plate. The critical temperature (39.491 $^{0}C$) was determined by performing a linear thermal buckling analysis. The same shape functions that were used to compute the so-called consistent mass matrix were used to compute the geometric stiffness matrix for the linear buckling analysis. The eigenvalue problem was solved using a subspace iteration method. The material properties used for the clamped cylindrical panel are $E_1 = 138Gpa, E_2 = 8.28Gpa, \nu_{12} = 0.33$ and $G_{12} = 6.9Gpa$. The geometry is the same as that used in the static analysis except that the thickness used in this case is 0.00254 $m$.

The results for thermal post buckling analysis of the square plate are given in Fig. 3.19 along with the Rayleigh-Ritz solution of Meyers and Hyer [89] and are in good agreement. The results given in Fig. 3.19 are nondimensionalized with respect to the critical buckling temperature (38.6 $^{o}C$) given by Meyers and Hyer [89]. The response of the imperfect plate closely follows the simulated response of the perfect plate as in the case of the results presented by Meyers and Hyer [89]. The results for the clamped cylinder under uniform temperature rise are given in Fig. 3.20 along with those obtained using the STRI3 and S4R elements. The present results are in good agreement with those obtained using the S4R element, whereas the results obtained using the STRI3 element do not agree well with the present results or those obtained using S4R.

### 3.4.4 Analysis of general shells under deformation-dependent pressure loads

Very few numerical examples involving deformation dependent pressure loads are available in the existing literature. To the best of the author's knowledge, a cantilever beam under uniform external pressure and a thin circular ring under a non-uniform external pressure are the two most widely used examples. These two examples were solved in order to validate the accuracy of the present formulation. Though the response in these two examples does not show any instability (within the range of the applied loads), the analysis was performed using the Riks method[13] as this method converges faster than the load-control method.

*Cantilever beam under uniform external pressure:* The geometry and material properties used are given in Fig. 3.21. The present results are compared in Fig. 3.21 with those obtained using S4R and are in good agreement. In order to study the effect of the pressure stiffness matrix on the convergence and accuracy of the solution, the analysis was performed both with and without including the pressure stiffness matrix in the system tangent stiffness matrix. The results of this comparative study are presented in Fig. 3.22, where Case-1 and Case-2 are with and without the pressure stiffness matrix, respectively. The results of Case-1 are the same as those presented in Fig. 3.21, but have been presented again for comparison. As can be seen from Fig. 3.22, the results in both the cases agree well, but in Case-2 very small load steps were required to obtain convergence beyond a certain load level. The analysis was abandoned beyond a certain load factor as the rate of convergence was extremely slow. This indicates that exclusion of the pressure stiffness matrix could inflict significant harmful effects on the convergence of the solution, especially in the regime of large deformations and rotations.

*Thin circular ring under non-uniform external pressure*: The geometry and the material properties used are given in Fig. 3.23. Since the geometry and the loading are symmetric, one half of the ring was modeled using a 1x40 mesh of 80 elements. The pressure distribution was assumed to be body attached, or in other words the magnitude of the pressure distribution is a function of the coordinates in the undeformed initial configuration, but the direction is always normal to the current/deformed configuration. Present results are compared with the numerical solution of Seide [90] in Fig. 3.23 and are in good agreement. The pressure stiffness matrix did not have a significant effect on the convergence of the solution in this problem.

Table 3.1: Convergence of non-dimensionalized mid-deflection of a simply supported [0/90/90/0] square plate under doubly sinusoidal load.

| Grid size | d.o.f. | $wE_2h^3 10^2/P_o a^4$ |
|---|---|---|
| 10x10 | 726 | 0.429483 |
| 12x12 | 1014 | 0.430029 |
| 14x14 | 1350 | 0.430356 |
| 16x16 | 1734 | 0.430567 |
| 18x18 | 2166 | 0.430711 |
| 20x20 | 2646 | 0.430814 |
| 22x22 | 3174 | 0.430889 |
| 24x24 | 3750 | 0.430947 |
| Phan and Reddy(1985) | | 0.434300 |

Table 3.2: Convergence of non-dimensionalized maximum displacements $u*, v*$ and $w*$ of a simply supported [-45/45] square plate under a doubly sinusoidal load.

| Grid size | d.o.f. | $u*$ | $v*$ | $w*$ |
|---|---|---|---|---|
| 10x10 | 726 | 0.3396 | 0.3396 | 0.4512 |
| 12x12 | 1014 | 0.3424 | 0.3424 | 0.4560 |
| 14x14 | 1350 | 0.3441 | 0.3441 | 0.4588 |
| 16x16 | 1734 | 0.3452 | 0.3452 | 0.4607 |
| 18x18 | 2166 | 0.3459 | 0.3459 | 0.4620 |
| 20x20 | 2646 | 0.3465 | 0.3465 | 0.4629 |
| 22x22 | 3174 | 0.3469 | 0.3469 | 0.4635 |
| 24x24 | 3750 | 0.3472 | 0.3472 | 0.4641 |
| Whitney and Leissa (1969) | | 0.3486 | 0.3486 | 0.4667 |

Table 3.3: Convergence of the vertical downward deflection at the mid-point of the free edge of the Scordelis roof.

| Grid size | 8x8 | 10x10 | 12x12 | 16x16 | 20x20 |
|---|---|---|---|---|---|
| Present | 0.2986 | 0.2991 | 0.2994 | 0.2998 | 0.3001 |
| Chen (1992) | 0.2999 | 0.2999 | 0.3001 | 0.3002 | - |
| Carpenter *el al.* (1985 ) | 0.3006 | 0.3003 | 0.3003 | 0.3003 | 0.3003 |
| STRI3 | 0.2642 | 0.2752 | 0.2819 | 0.2896 | 0.2933 |

Table 3.4: Convergence of the vertical downward deflection (x$10^3$) at the load point of a pinched cylinder.

| Grid size | 8x8 | 10x10 | 12x12 | 16x16 | 20x20 | 23x23 |
|---|---|---|---|---|---|---|
| Present | 1.6183 | 1.7060 | 1.7508 | 1.7906 | 1.8066 | 1.8130 |
| Chen (1992) | 1.7201 | 1.8051 | 1.8412 | 1.8600 | | |
| Carpenter *el al.* (1985 ) | 1.7353 | 1.8138 | 1.8485 | 1.8631 | 1.8613 | 1.8576 |
| STRI3 | 1.5740 | 1.6770 | 1.7300 | 1.7770 | 1.7970 | 1.8050 |

Table 3.5: Convergence of the radial deflection in the direction of the load, at point A, of a hemispherical shell with a free hole.

| Grid size | 8x8 | 10x10 | 12x12 | 16x16 | 20x20 | 23x23 |
|---|---|---|---|---|---|---|
| Present | 0.0354 | 0.0524 | 0.0664 | 0.0819 | 0.0881 | 0.0902 |
| Chen (1992) | 0.0759 | 0.0849 | 0.0888 | 0.0917 | | |
| STRI3 | 0.0927 | 0.0926 | 0.0925 | 0.0924 | 0.0925 | 0.0926 |

Table 3.6: Convergence of the vertical deflection at the load point A of a hemispherical shell with a free hole.

| Grid size | 10x10 | 14x14 | 18x18 | 24x24 | 28x28 |
|---|---|---|---|---|---|
| Present | +0.0212 | -0.1045 | +0.0246 | +0.0756 | +0.0536 |
| STRI3 | -0.1160 | +0.0397 | +0.0239 | -0.0165 | -0.9200 |

Table 3.7: Convergence of the radial deflection in the direction of the load, at point A, of a hemispherical shell, with the vertical deflection constrained along the hole.

| Grid size | 10x10 | 14x14 | 18x18 | 24x24 | 28x28 | 36x36 |
|---|---|---|---|---|---|---|
| Present | 0.0517 | 0.0735 | 0.0824 | 0.0870 | 0.0881 | 0.0889 |
| STRI3 | 0.0882 | 0.0883 | 0.0884 | 0.0887 | 0.0888 | 0.0890 |

Table 3.8: Convergence of the downward vertical deflection at the load point A, of a hemispherical shell, with the vertical displacement constrained along the hole.

| Grid size | 10x10 | 14x14 | 18x18 | 24x24 | 28x28 | 36x36 |
|---|---|---|---|---|---|---|
| Present | 0.0256 | 0.0363 | 0.0406 | 0.0428 | 0.0432 | 0.0436 |
| STRI3 | 0.0438 | 0.0436 | 0.0435 | 0.0435 | 0.0436 | 0.0437 |

Table 3.9: Convergence of non-dimensionalized mid- deflection of simply supported [0/90] and [0/90/90/0] spherical shells under a uniformly distributed load.

| Grid size full shell | d.o.f. | $wE_2h^3 10^3/P_0a^4$ [0/90] | [0/90/90/0] |
|---|---|---|---|
| 10x10 | 726 | 5.320 | 3.600 |
| 16x16 | 1734 | 5.447 | 3.663 |
| 20x20 | 2646 | 5.477 | 3.679 |
| 24x24 | 3750 | 5.494 | 3.687 |
| 28x28 | 5046 | 5.503 | 3.691 |
| 30x30 | 5766 | 5.507 | 3.693 |
| 32x32 | 6534 | 5.510 | 3.694 |
| Reddy (1984) | | 5.542 | 3.720 |

Table 3.10: Convergence of first five natural frequencies (Hz) of a square [0/45/-45/90/90/-45/45/0] cantilever plate using lumped mass.

| mesh | mode 1 | mode 2 | mode 3 | mode 4 | mode 5 |
|---|---|---|---|---|---|
| 6x6 | 223.09 | 424.93 | 959.98 | 1364.01 | 1627.73 |
| 8x8 | 224.54 | 426.29 | 986.88 | 1391.17 | 1673.51 |
| 10x10 | 225.20 | 426.84 | 1000.08 | 1404.03 | 1694.57 |
| 12x12 | 225.55 | 427.13 | 1007.44 | 1411.10 | 1705.88 |
| 14x14 | 225.76 | 427.29 | 1011.93 | 1415.38 | 1712.64 |
| 16x16 | 225.90 | 427.38 | 1014.87 | 1418.18 | 1717.00 |
| 18x18 | 225.99 | 427.45 | 1016.89 | 1420.10 | 1719.96 |
| 20x20 | 226.05 | 427.49 | 1018.34 | 1421.47 | 1722.08 |
| 22x22 | 226.10 | 427.53 | 1019.41 | 1422.49 | 1723.63 |
| 24x24 | 226.14 | 427.55 | 1020.23 | 1423.26 | 1724.81 |
| Kapania and Singhvi(1991) | 225.14 | 425.63 | 1020.21 | 1418.18 | 1721.59 |

Table 3.11: Convergence of first five natural frequencies (Hz) of a square [0/45/-45/90/90/-45/45/0] cantilever plate using consistent mass.

| mesh | mode 1 | mode 2 | mode 3 | mode 4 | mode 5 |
|---|---|---|---|---|---|
| 6x6 | 225.91 | 429.59 | 1040.47 | 1413.20 | 1728.79 |
| 8x8 | 226.13 | 428.89 | 1033.73 | 1419.74 | 1731.33 |
| 10x10 | 226.22 | 428.52 | 1030.54 | 1422.74 | 1732.03 |
| 12x12 | 226.26 | 428.29 | 1028.77 | 1424.26 | 1732.07 |
| 14x14 | 226.28 | 428.14 | 1027.68 | 1425.14 | 1731.96 |
| 16x16 | 226.30 | 428.04 | 1026.97 | 1425.69 | 1731.83 |
| 18x18 | 226.31 | 427.97 | 1026.47 | 1426.05 | 1731.70 |
| 20x20 | 226.31 | 427.91 | 1026.11 | 1426.31 | 1731.60 |
| Kapania and Singhvi(1991) | 225.14 | 425.63 | 1020.21 | 1418.18 | 1721.59 |

Table 3.12: Convergence of the first five natural frequencies (Hz) of a [0/22.5] square cantilever plate using lumped mass.

| Grid size | Mode 1 | Mode 2 | Mode 3 | Mode 4 | Mode 5 |
|---|---|---|---|---|---|
| 10x10 | 34.27 | 56.55 | 121.80 | 213.75 | 240.19 |
| 12x12 | 34.32 | 56.57 | 122.47 | 214.81 | 242.57 |
| 14x14 | 34.35 | 56.58 | 122.88 | 215.45 | 243.98 |
| 16x16 | 34.37 | 56.59 | 123.14 | 215.87 | 244.89 |
| 18x18 | 34.39 | 56.59 | 123.33 | 216.16 | 245.50 |
| Kapania and Singhvi (1991) | 34.26 | 56.34 | 123.40 | 216.17 | 246.57 |

Table 3.13: Convergence of the first five natural frequencies (Hz) of a [0/22.5] square cantilever plate using consistent mass.

| Grid size | Mode 1 | Mode 2 | Mode 3 | Mode 4 | Mode 5 |
|---|---|---|---|---|---|
| 10x10 | 34.44 | 56.73 | 124.91 | 217.62 | 249.55 |
| 12x12 | 34.44 | 56.70 | 124.64 | 217.53 | 249.09 |
| 14x14 | 34.44 | 56.68 | 124.48 | 217.47 | 248.77 |
| 16x16 | 34.44 | 56.66 | 124.37 | 217.43 | 248.55 |
| 18x18 | 34.44 | 56.65 | 124.30 | 217.39 | 248.40 |
| Kapania and Singhvi (1991) | 34.26 | 56.34 | 123.40 | 216.17 | 246.57 |

Table 3.14: Convergence of the first five natural frequencies (Hz) of a $[15_2/0]_s$ skew cantilever plate ($\beta = 30$) using lumped mass.

| Grid size | Mode 1 | Mode 2 | Mode 3 | Mode 4 | Mode 5 |
|---|---|---|---|---|---|
| 4x8 | 16.81 | 74.68 | 105.82 | 193.29 | 284.36 |
| 6x12 | 16.87 | 75.98 | 108.65 | 197.22 | 294.52 |
| 8x16 | 16.89 | 76.45 | 109.70 | 198.65 | 298.26 |
| 10x20 | 16.90 | 76.67 | 110.20 | 199.32 | 300.02 |
| 12x24 | 16.91 | 76.79 | 110.47 | 199.68 | 300.98 |
| Kapania and Singhvi (1991) | 16.96 | 77.28 | 111.40 | | |

Table 3.15: Convergence of the first five natural frequencies (Hz) of a $[15_2/0]_s$ skew cantilever plate ($\beta = 30$) using consistent mass.

| Grid size | Mode 1 | Mode 2 | Mode 3 | Mode 4 | Mode 5 |
|---|---|---|---|---|---|
| 4x8 | 16.93 | 76.94 | 111.67 | 199.97 | 304.49 |
| 6x12 | 16.92 | 77.01 | 111.37 | 200.27 | 303.80 |
| 8x16 | 16.92 | 77.03 | 111.26 | 200.38 | 303.55 |
| 10x20 | 16.92 | 77.04 | 111.20 | 200.43 | 303.43 |
| 12x24 | 16.92 | 77.05 | 111.17 | 200.46 | 303.35 |
| Kapania and Singhvi (1991) | 16.96 | 77.28 | 111.40 | | |

Table 3.16: Convergence of the first five natural frequencies (Hz) of a [0/22.5] skew cantilever plate ($\beta = 45$) using lumped mass.

| Grid size | Mode 1 | Mode 2 | Mode 3 | Mode 4 | Mode 5 |
|---|---|---|---|---|---|
| 10x10 | 20.58 | 44.89 | 115.10 | 142.33 | 216.67 |
| 12x12 | 20.57 | 45.00 | 115.47 | 143.25 | 218.02 |
| 14x14 | 20.56 | 45.06 | 115.69 | 143.80 | 218.83 |
| 16x16 | 20.55 | 45.10 | 115.82 | 144.14 | 219.35 |
| 18x18 | 20.55 | 45.13 | 115.91 | 144.38 | 219.71 |
| Kapania and Singhvi (1991) | 20.42 | 45.09 | 115.75 | 144.76 | 219.94 |

Table 3.17: Convergence of the first five natural frequencies (Hz) of a [0/22.5] skew cantilever plate ($\beta = 45$) using consistent mass.

| Grid size | Mode 1 | Mode 2 | Mode 3 | Mode 4 | Mode 5 |
|---|---|---|---|---|---|
| 10x10 | 20.68 | 45.33 | 117.06 | 145.99 | 222.18 |
| 12x12 | 20.64 | 45.30 | 116.83 | 145.81 | 221.85 |
| 14x14 | 20.61 | 45.29 | 116.69 | 145.68 | 221.65 |
| 16x16 | 20.59 | 45.28 | 116.59 | 145.59 | 221.51 |
| 18x18 | 20.58 | 45.27 | 116.52 | 145.52 | 221.41 |
| Kapania and Singhvi (1991) | 20.42 | 45.09 | 115.75 | 144.76 | 219.94 |

Table 3.18: Convergence of first five non-dimensionalized frequencies ($\omega a^2\sqrt{\rho/E_2}/h$) of a simply supported [0/90/90/0] spherical shell using lumped mass.

| mesh<br>full shell | mode 1 | mode 2 | mode 3 | mode 4 | mode 5 |
|---|---|---|---|---|---|
| 10x10 | 20.62 | 32.70 | 56.27 | 58.98 | 61.37 |
| 16x16 | 20.53 | 32.53 | 56.66 | 58.60 | 61.96 |
| 20x20 | 20.51 | 32.50 | 56.75 | 58.52 | 62.11 |
| 24x24 | 20.50 | 32.48 | 56.80 | 58.48 | 62.20 |
| 28x28 | 20.49 | 32.46 | 56.83 | 58.45 | 62.25 |
| Reddy (1984) | 20.38 | | | | |

Table 3.19: Convergence of first five non-dimensionalized frequencies ($\omega a^2\sqrt{\rho/E_2}/h$) of a simply supported [0/90/90/0] spherical shell using consistent mass.

| mesh<br>full shell | mode 1 | mode 2 | mode 3 | mode 4 | mode 5 |
|---|---|---|---|---|---|
| 10x10 | 20.58 | 32.65 | 56.31 | 58.94 | 61.42 |
| 16x16 | 20.48 | 32.48 | 56.67 | 58.55 | 61.95 |
| 20x20 | 20.46 | 32.44 | 56.75 | 58.47 | 62.09 |
| 24x24 | 20.45 | 32.42 | 56.80 | 58.43 | 62.17 |
| 28x28 | 20.44 | 32.41 | 56.83 | 58.41 | 62.22 |
| Reddy (1984) | 20.38 | | | | |

Table 3.20: Convergence of mid-deflection $w_{max}$ due to a nonuniform thermal field ($T_u = 1, T_l = -1$) and maximum in-plane displacements $u_{max}, v_{max}$ due to a uniform thermal field ($T_u = 1, T_l = 1$) for a simply supported [0/90/90/0] square plate.

| Grid size full plate | $10^5\ u_{max}$ | $10^5\ v_{max}$ | $10^3\ w_{max}$ |
|---|---|---|---|
| 6x6 | 0.44274 | 0.44274 | 0.21177 |
| 8x8 | 0.44309 | 0.44309 | 0.21254 |
| 10x10 | 0.44329 | 0.44329 | 0.21286 |
| 12x12 | 0.44342 | 0.44342 | 0.21303 |
| 14x14 | 0.44350 | 0.44350 | 0.21312 |
| 16x16 | 0.44355 | 0.44355 | 0.21318 |
| 18x18 | 0.44359 | 0.44359 | 0.21322 |
| 20x20 | 0.44362 | 0.44362 | 0.21325 |
| 22x22 | 0.44364 | 0.44364 | 0.21327 |
| Wu and Tauchert (1980) | 0.44138 | 0.44138 | 0.21336 |

Table 3.21: Convergence of mid-deflection $w_{max}$ and maximum in-plane displacements $u_{max}, v_{max}$ for a simply supported [0/90/0/90] square plate (BC1) under a non-uniform thermal field ($T_u = 1, T_l = 0$).

| Grid size | $10^5\ u_{max}$ | $10^5\ v_{max}$ | $10^3\ w_{max}$ |
|---|---|---|---|
| full plate | | | |
| 6x6 | 0.25268 | 0.19543 | 0.10995 |
| 8x8 | 0.25317 | 0.19544 | 0.11044 |
| 10x10 | 0.25341 | 0.19546 | 0.11065 |
| 12x12 | 0.25354 | 0.19548 | 0.11076 |
| 14x14 | 0.25363 | 0.19549 | 0.11083 |
| 16x16 | 0.25368 | 0.19550 | 0.11087 |
| 18x18 | 0.25372 | 0.19551 | 0.11090 |
| 20x20 | 0.25375 | 0.19552 | 0.11092 |
| Wu and Tauchert (1980) | 0.25250 | 0.19446 | 0.11099 |

Table 3.22: Convergence of mid-deflection $w_{max}$ and maximum in-plane displacements $u_{max}, v_{max}$ for a simply supported [15/-15/15/-15] square plate (BC2) under a non-uniform thermal field ($T_u = 1, T_l = 0$)

| Grid size full plate | $10^6\ u_{max}$ | $10^6\ v_{max}$ | $10^3\ w_{max}$ |
|---|---|---|---|
| 6x6 | 0.16902 | 0.13556 | 0.09988 |
| 8x8 | 0.17326 | 0.13785 | 0.10025 |
| 10x10 | 0.17536 | 0.13860 | 0.10040 |
| 12x12 | 0.17660 | 0.13890 | 0.10047 |
| 14x14 | 0.17739 | 0.13903 | 0.10052 |
| 16x16 | 0.17795 | 0.13909 | 0.10055 |
| 18x18 | 0.17835 | 0.13911 | 0.10057 |
| 20x20 | 0.17864 | 0.13911 | 0.10058 |
| Wu and Tauchert (1980) | 0.17967 | 0.13740 | 0.10063 |

Table 3.23: Convergence of mid-deflection $w_{max}$ and maximum in-plane displacements $u_{max}, v_{max}$ for a simply supported [0/90/0/90] spherical shell (BC1) under a non-uniform thermal field ($T_u = 1, T_l = 0$)

| Grid size full shell | $10^5\ u_{max}$ | $10^5\ v_{max}$ | $10^4\ w_{max}$ |
|---|---|---|---|
| 6x6 | 0.15838 | 0.12010 | 0.79489 |
| 8x8 | 0.14889 | 0.11464 | 0.79315 |
| 10x10 | 0.15084 | 0.11832 | 0.79232 |
| 12x12 | 0.15219 | 0.11493 | 0.79186 |
| 14x14 | 0.14918 | 0.11697 | 0.79159 |
| 16x16 | 0.15077 | 0.11656 | 0.79141 |
| 18x18 | 0.15105 | 0.11609 | 0.79128 |
| 20x20 | 0.14944 | 0.11671 | 0.79119 |
| 22x22 | 0.15065 | 0.11572 | 0.79113 |

Table 3.24: Convergence of mid-deflection $w_{max}$ and maximum in-plane displacements $u_{max}, v_{max}$ for a simply supported [45/-45/45/-45] spherical shell (BC1) under a non-uniform thermal field ($T_u = 1, T_l = 0$)

| Grid Size full shell | $10^5$ $u_{max}$ | $10^5$ $v_{max}$ | $10^4$ $w_{max}$ |
|---|---|---|---|
| 6x6 | 0.14844 | 0.14844 | 0.71711 |
| 8x8 | 0.14208 | 0.14209 | 0.71545 |
| 10x10 | 0.14076 | 0.14077 | 0.71467 |
| 12x12 | 0.14322 | 0.14323 | 0.71423 |
| 14x14 | 0.14178 | 0.14178 | 0.71394 |
| 16x16 | 0.14131 | 0.14132 | 0.71374 |
| 18x18 | 0.14255 | 0.14256 | 0.71359 |
| 20x20 | 0.14196 | 0.14197 | 0.71348 |
| 22x22 | 0.14168 | 0.14169 | 0.71339 |
| 26x26 | 0.14196 | 0.14197 | 0.71326 |
| 30x30 | 0.14217 | 0.14218 | 0.71318 |

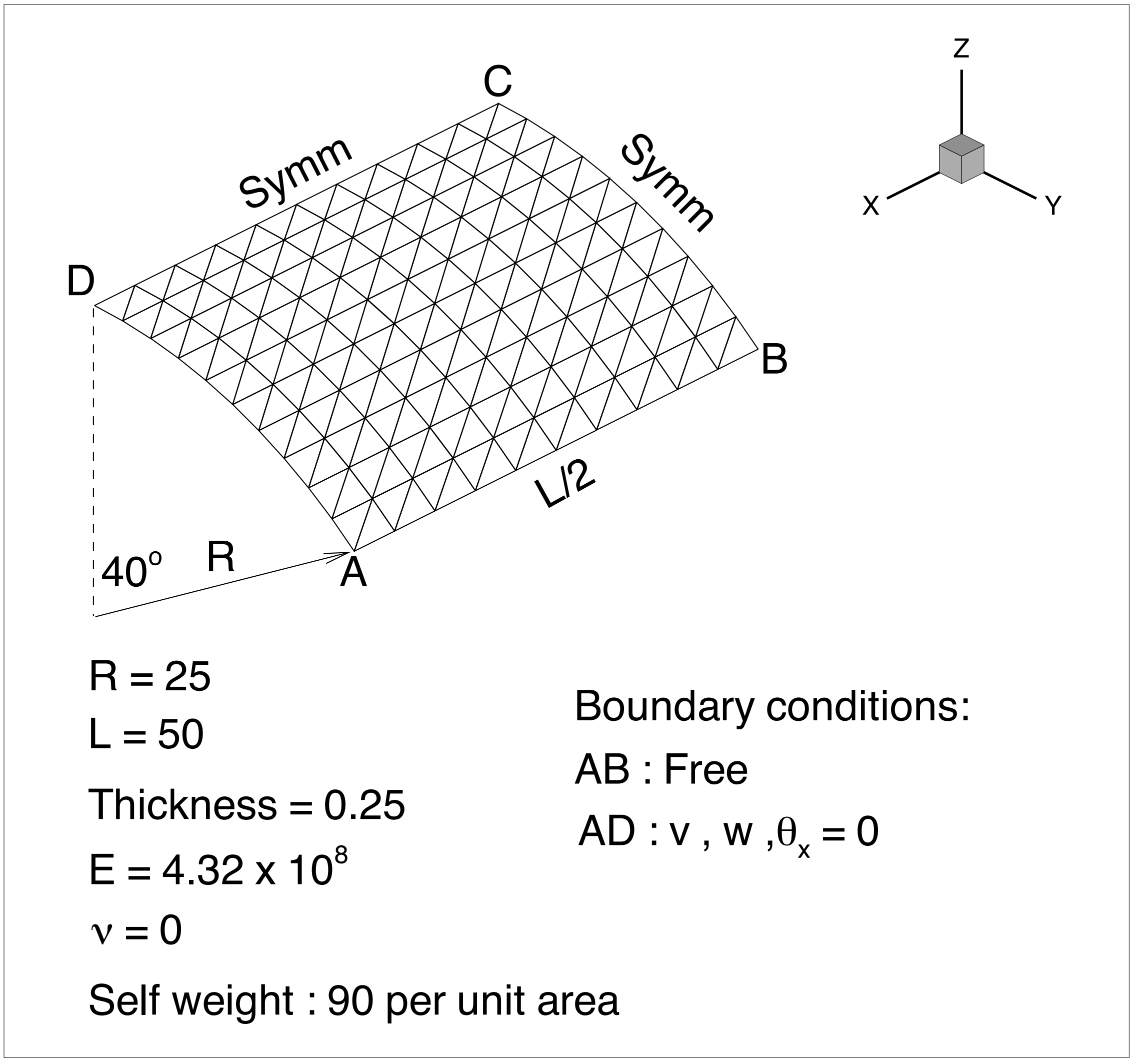

Figure 3.1: Geometry of the Scordelis-Lo roof.

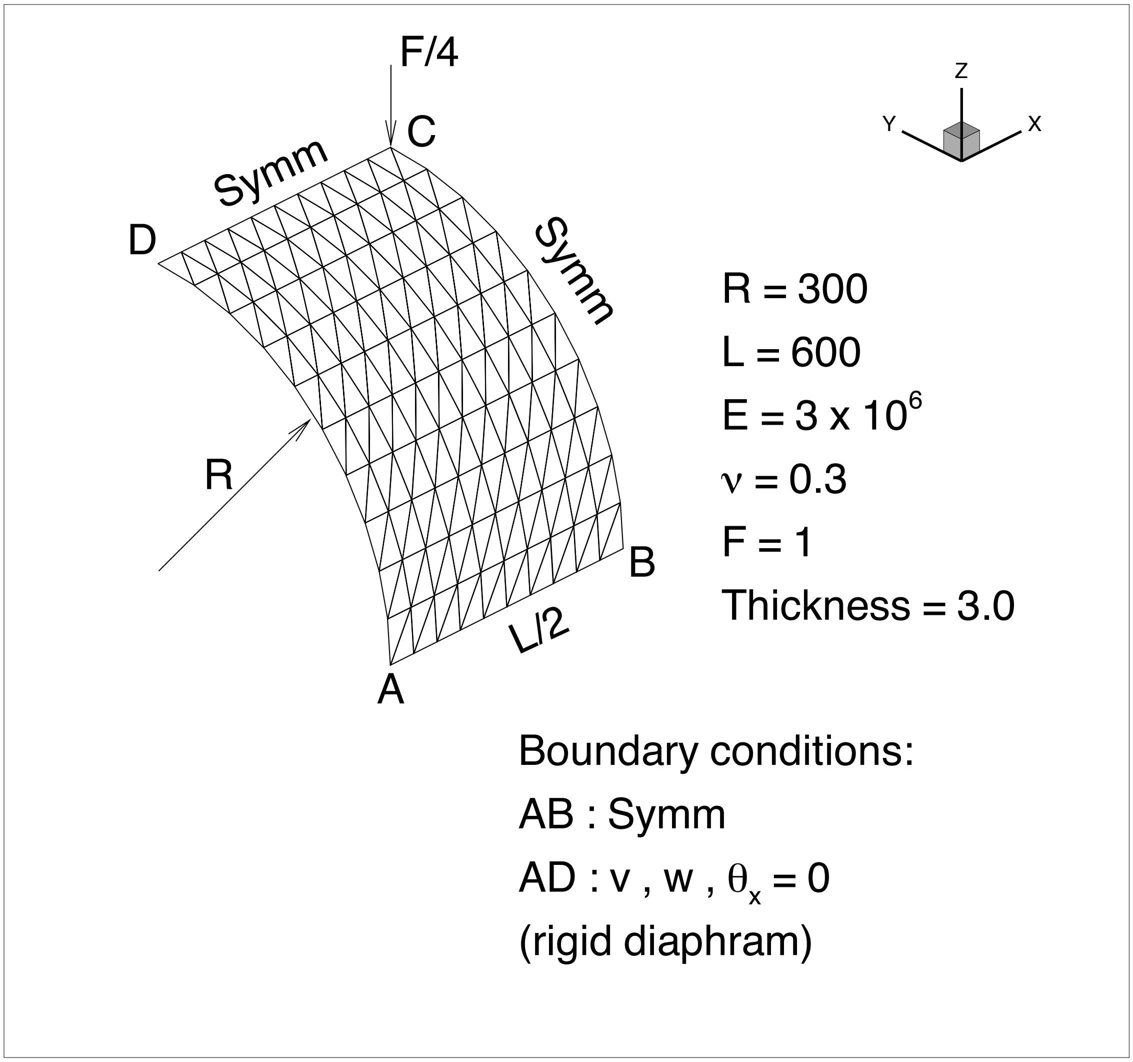

Figure 3.2: Geometry of the pinched cylinder

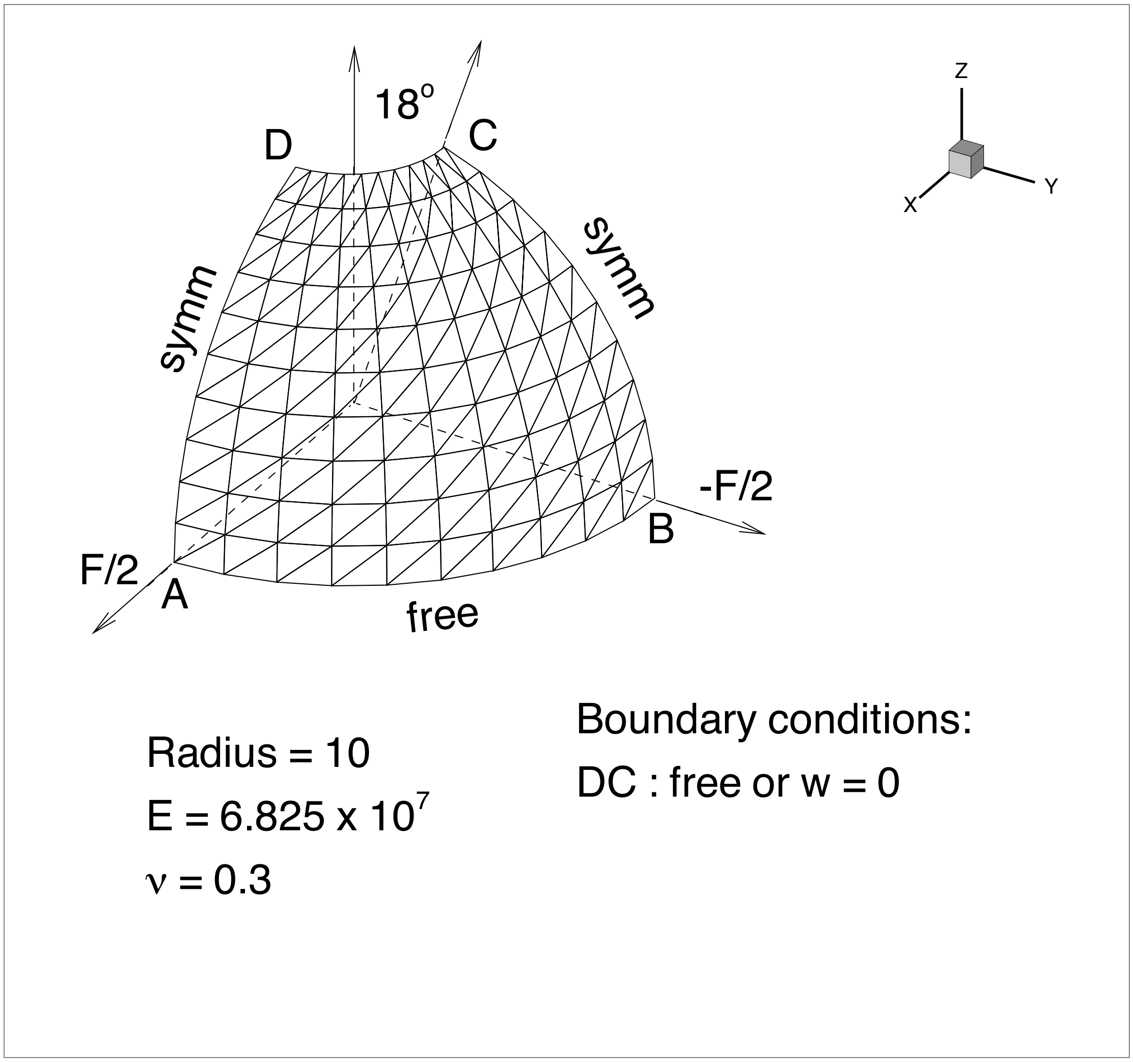

Figure 3.3: Geometry of the hemispherical shell

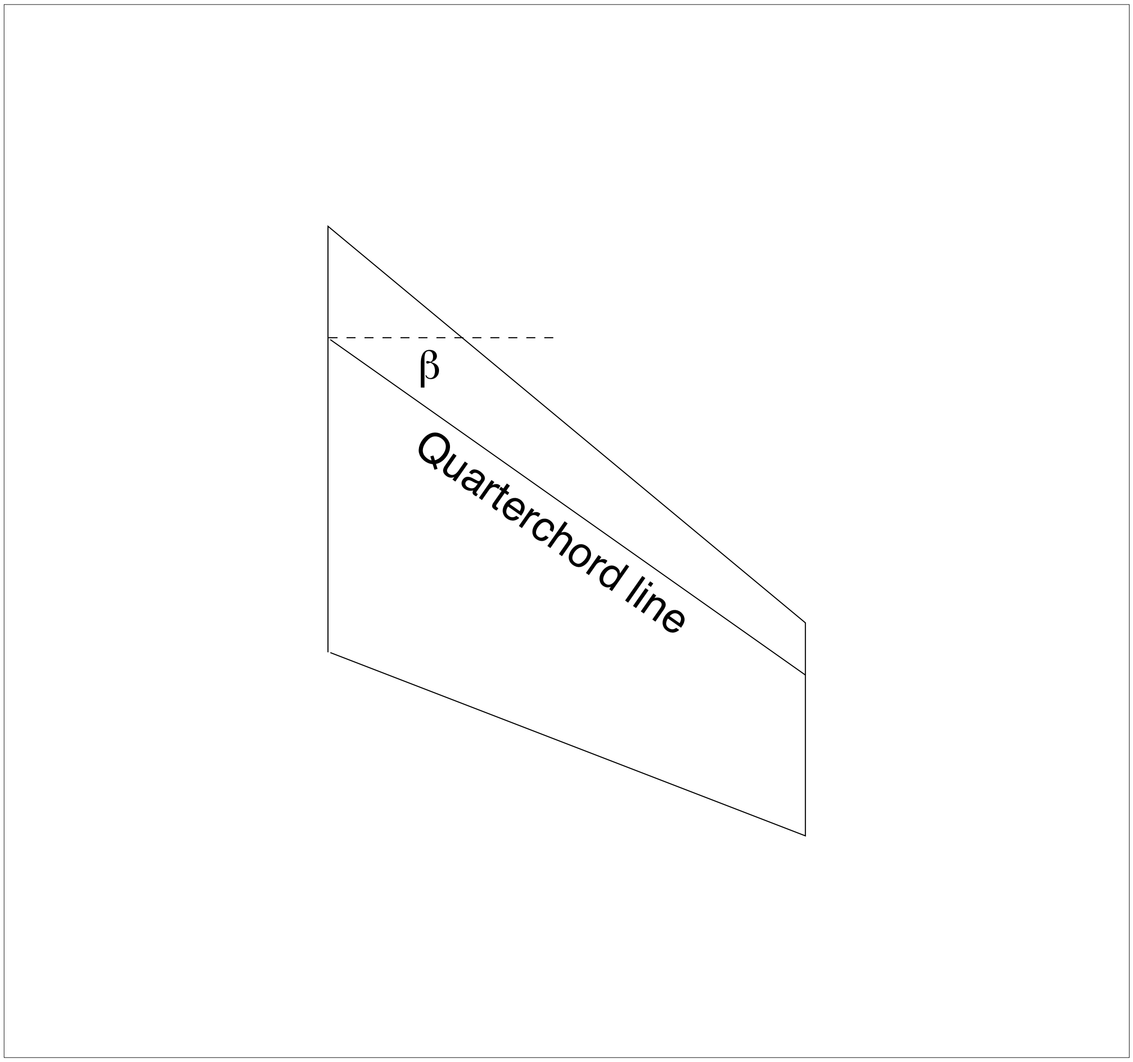

Figure 3.4: Geometry of the skew cantilever plate.

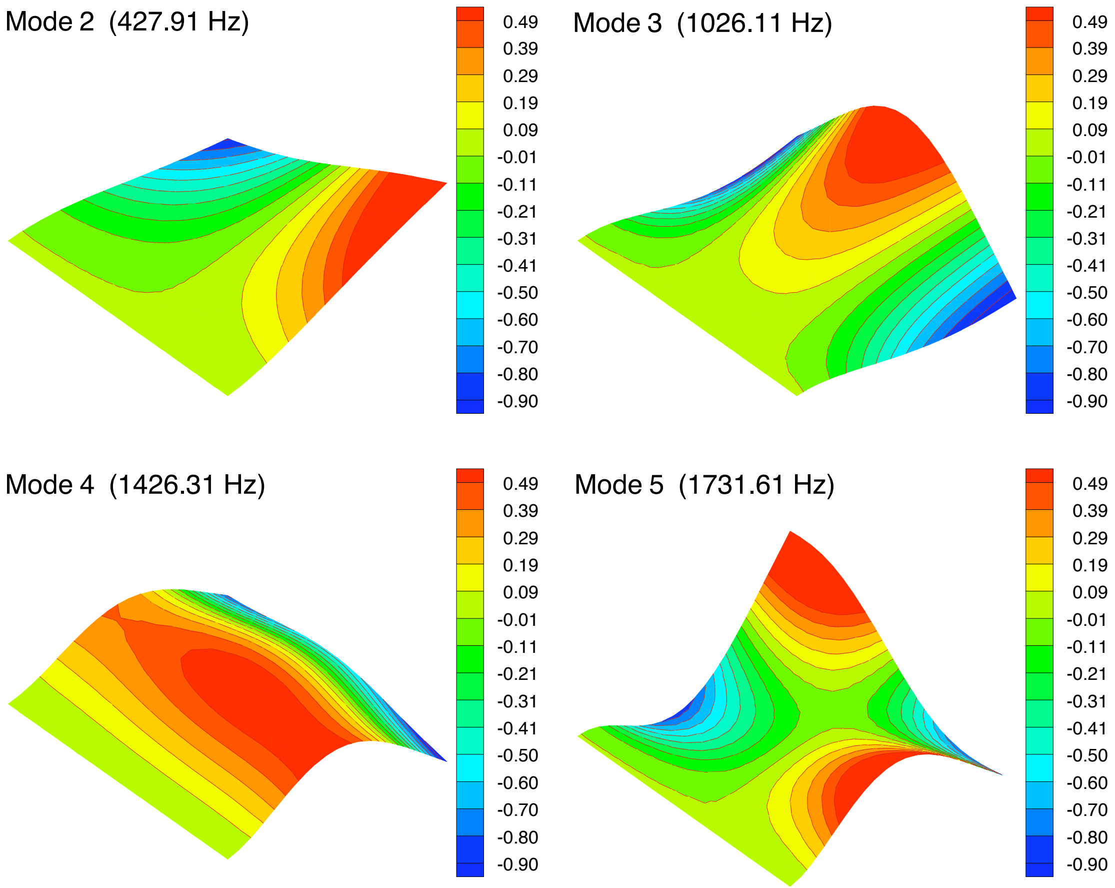

Figure 3.5: Normalized modes 2,3,4 and 5 of a [0/45/-45/90/90/-45/45/0] cantilever plate obtained using consistent mass matrix

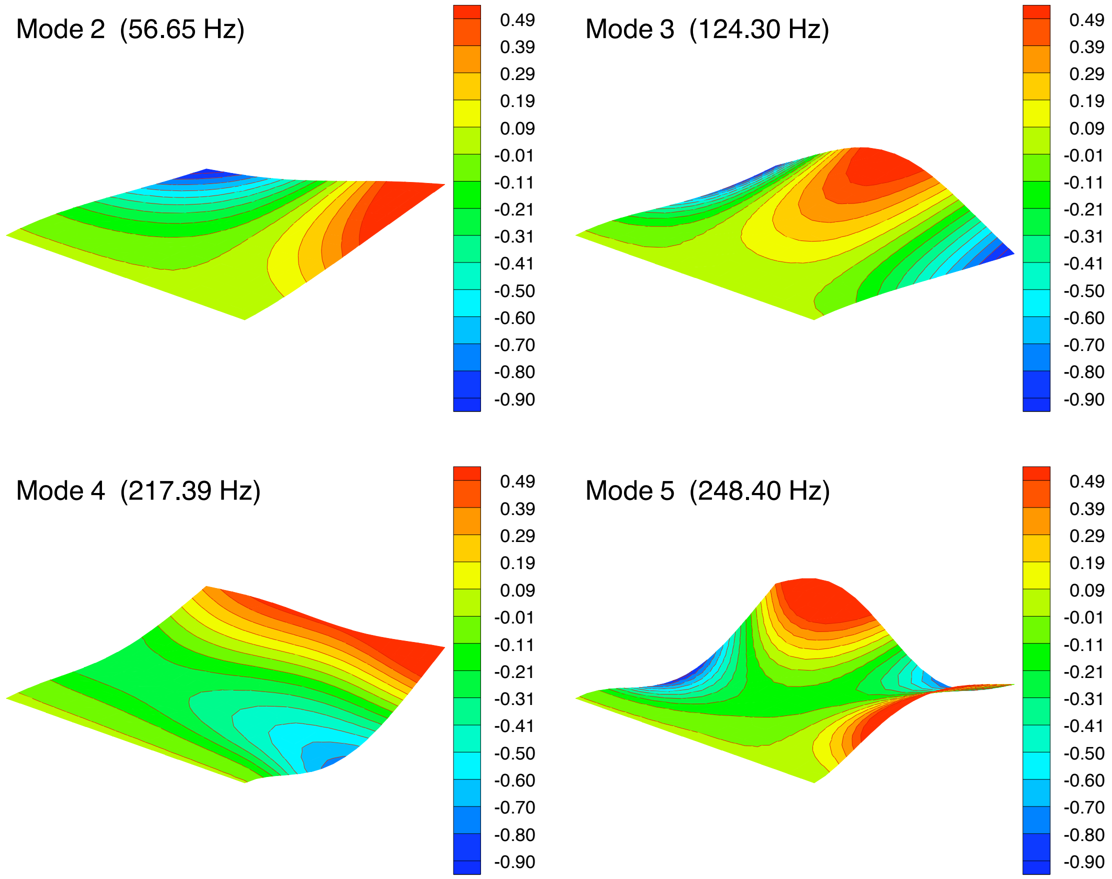
Mode 2 (56.65 Hz)

Mode 3 (124.30 Hz)

Mode 4 (217.39 Hz)

Mode 5 (248.40 Hz)

Figure 3.6: Normalized modes 2,3,4 and 5 of a [0/22.5] cantilever plate obtained using consistent mass matrix

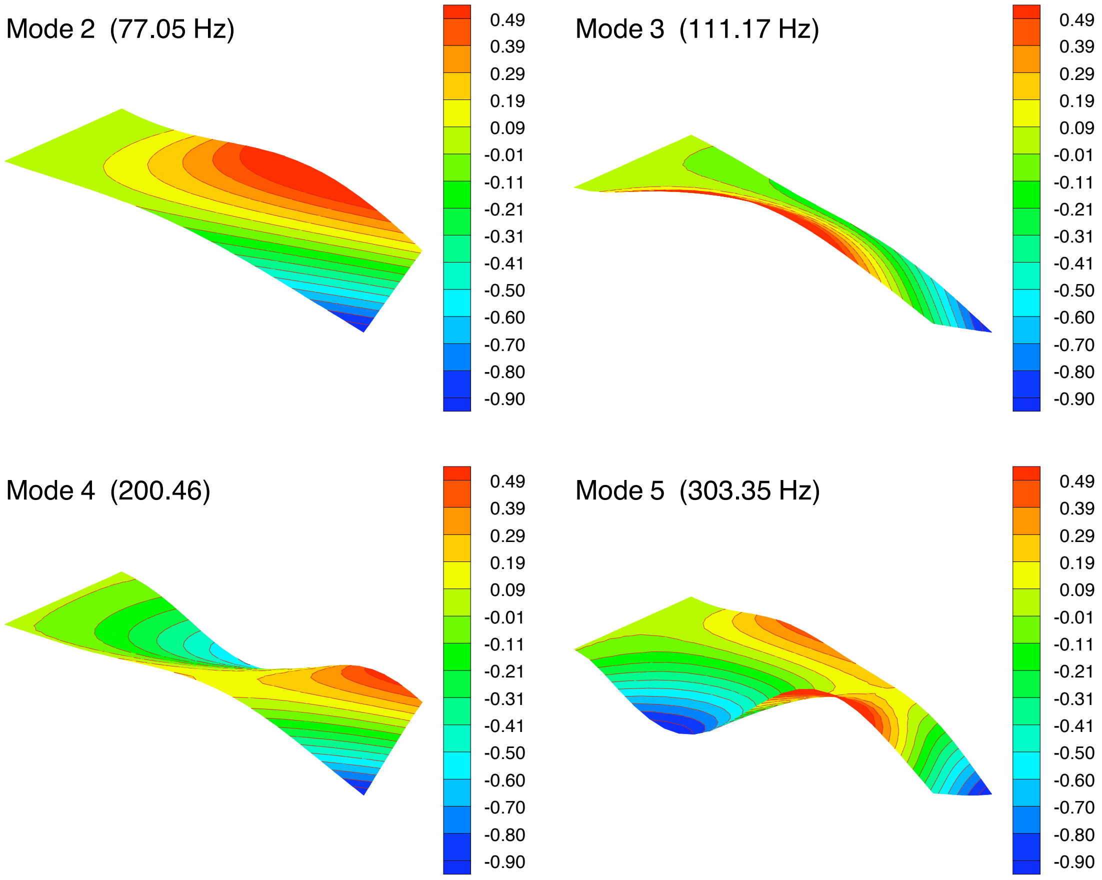

Figure 3.7: Normalized modes 2,3,4 and 5 of a $[15_2/0]_s$ skew cantilever plate ($\beta = 30$) obtained using consistent mass matrix

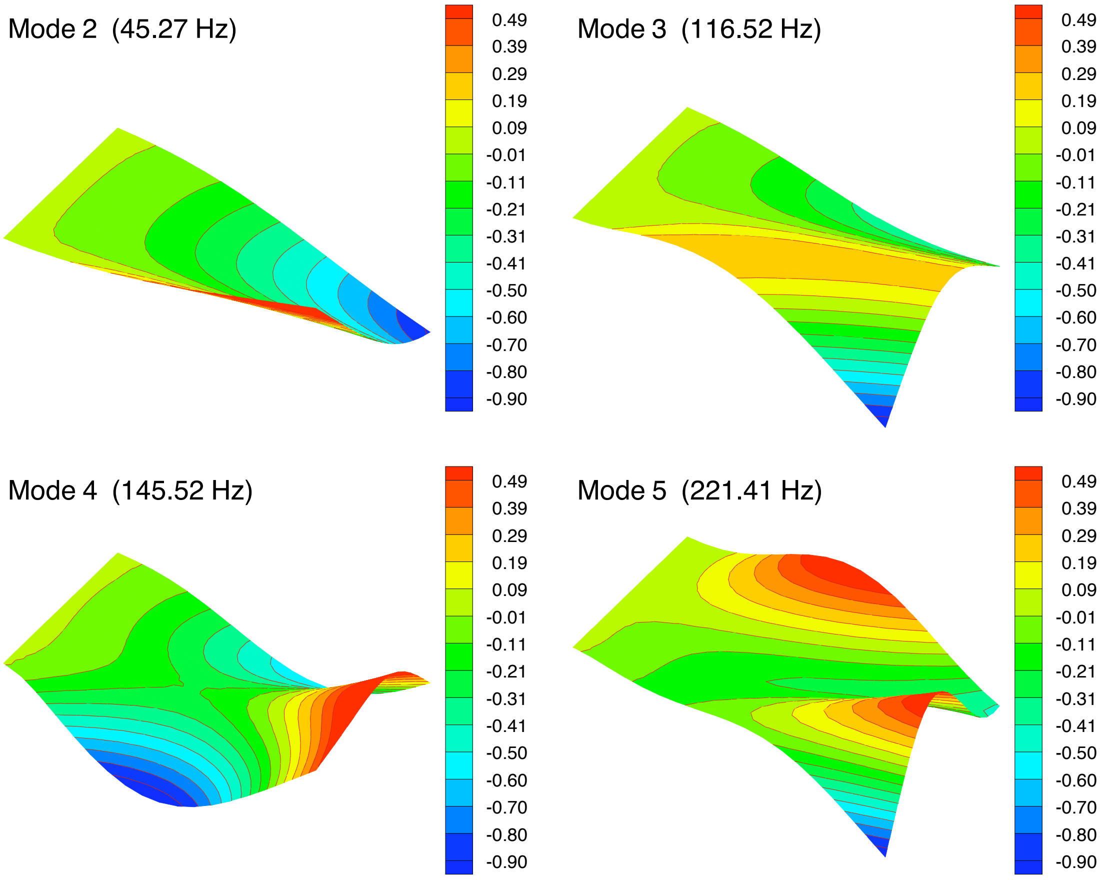

Figure 3.8: Normalized modes 2,3,4 and 5 of a [0/22.5] skew cantilever plate ($\beta = 45$) obtained using consistent mass matrix

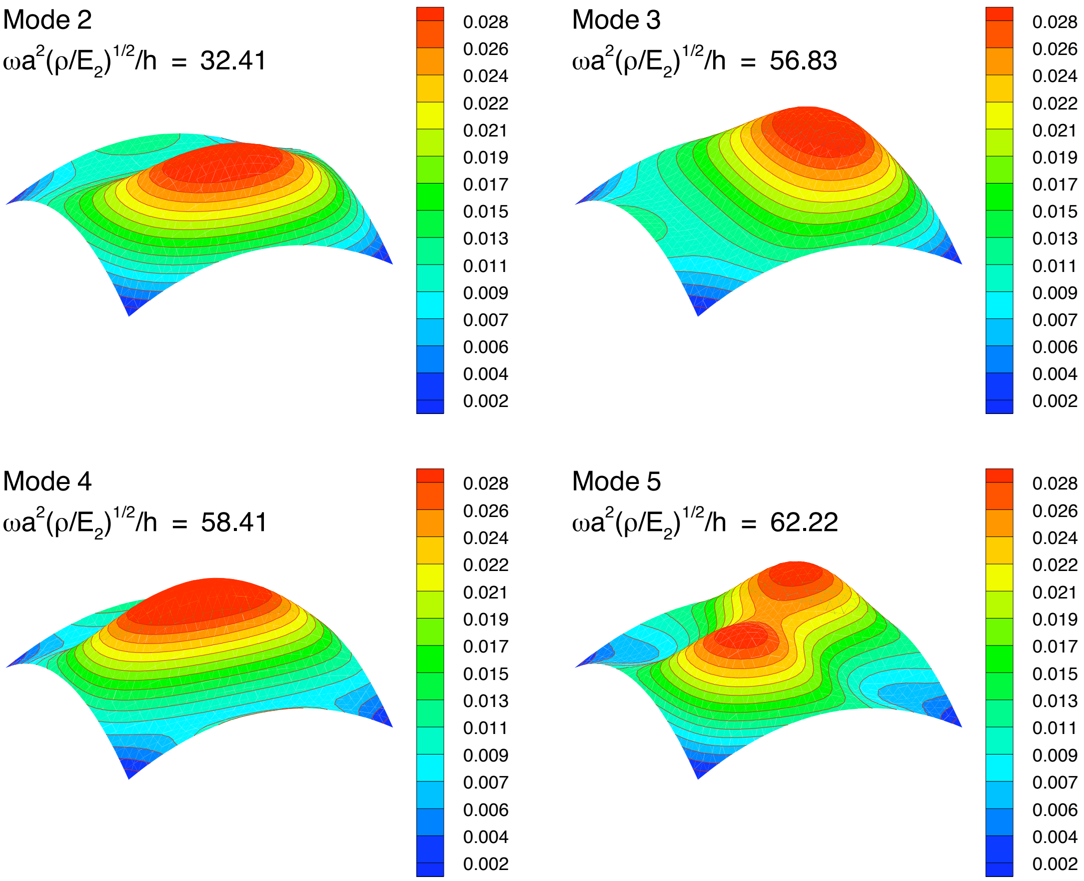

Figure 3.9: Normalized modes 2,3,4 and 5 of a [0/90/90/0] simply supported spherical shell obtained using consistent mass matrix

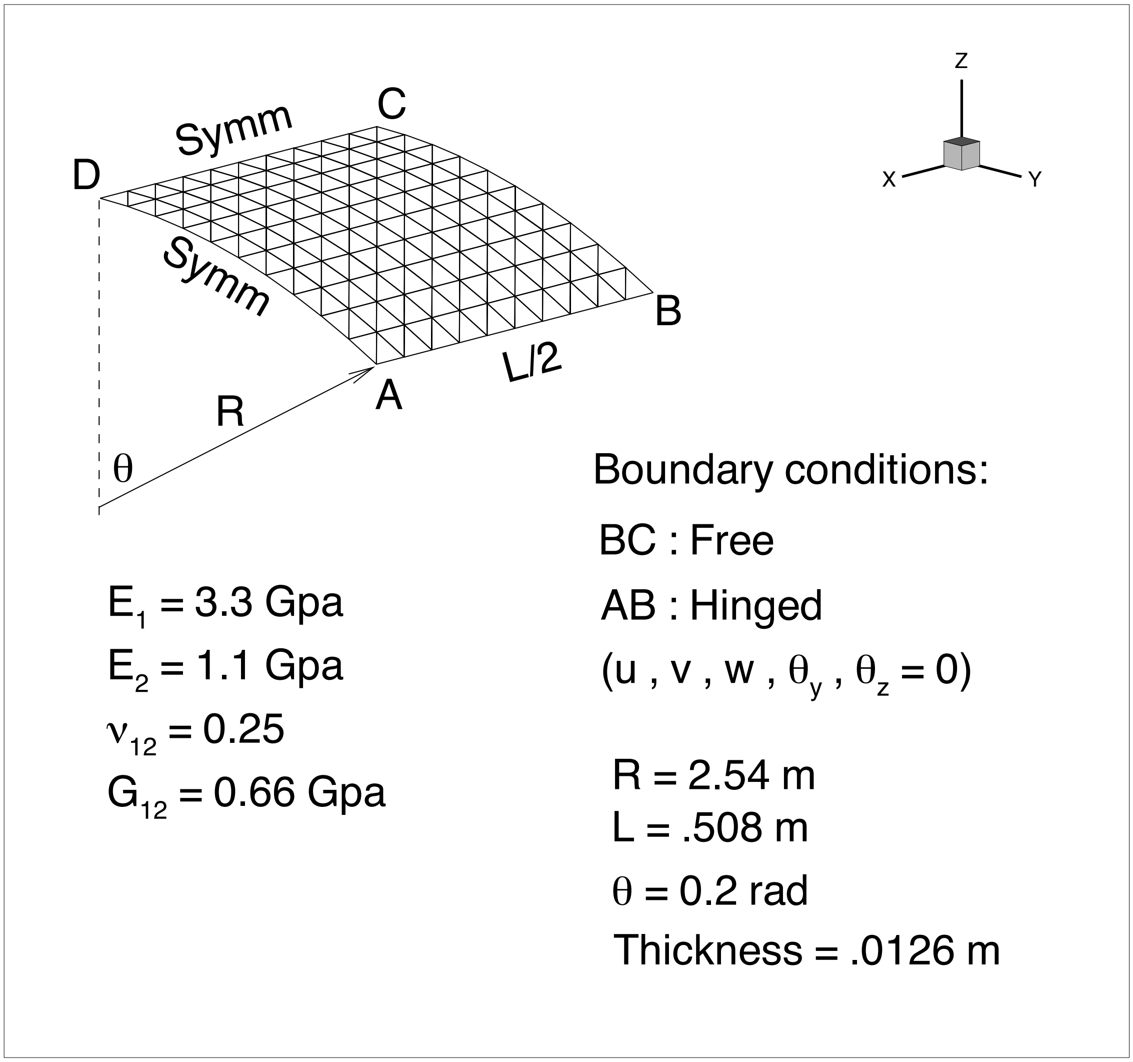

Figure 3.10: Geometry of the hinged cylindrical panel.

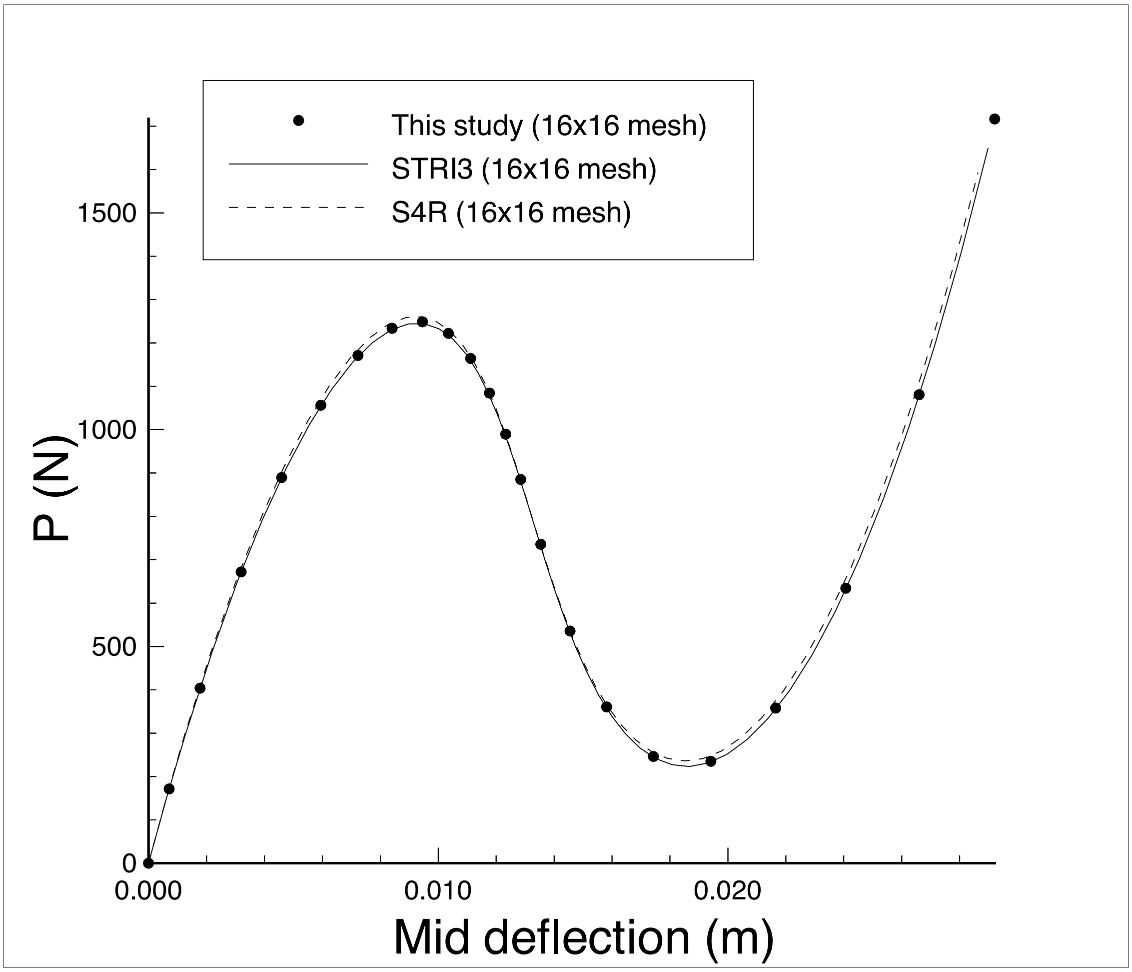

Figure 3.11: Snap-through behavior of a [45/-45] hinged cylindrical panel under a concentrated mid-load.

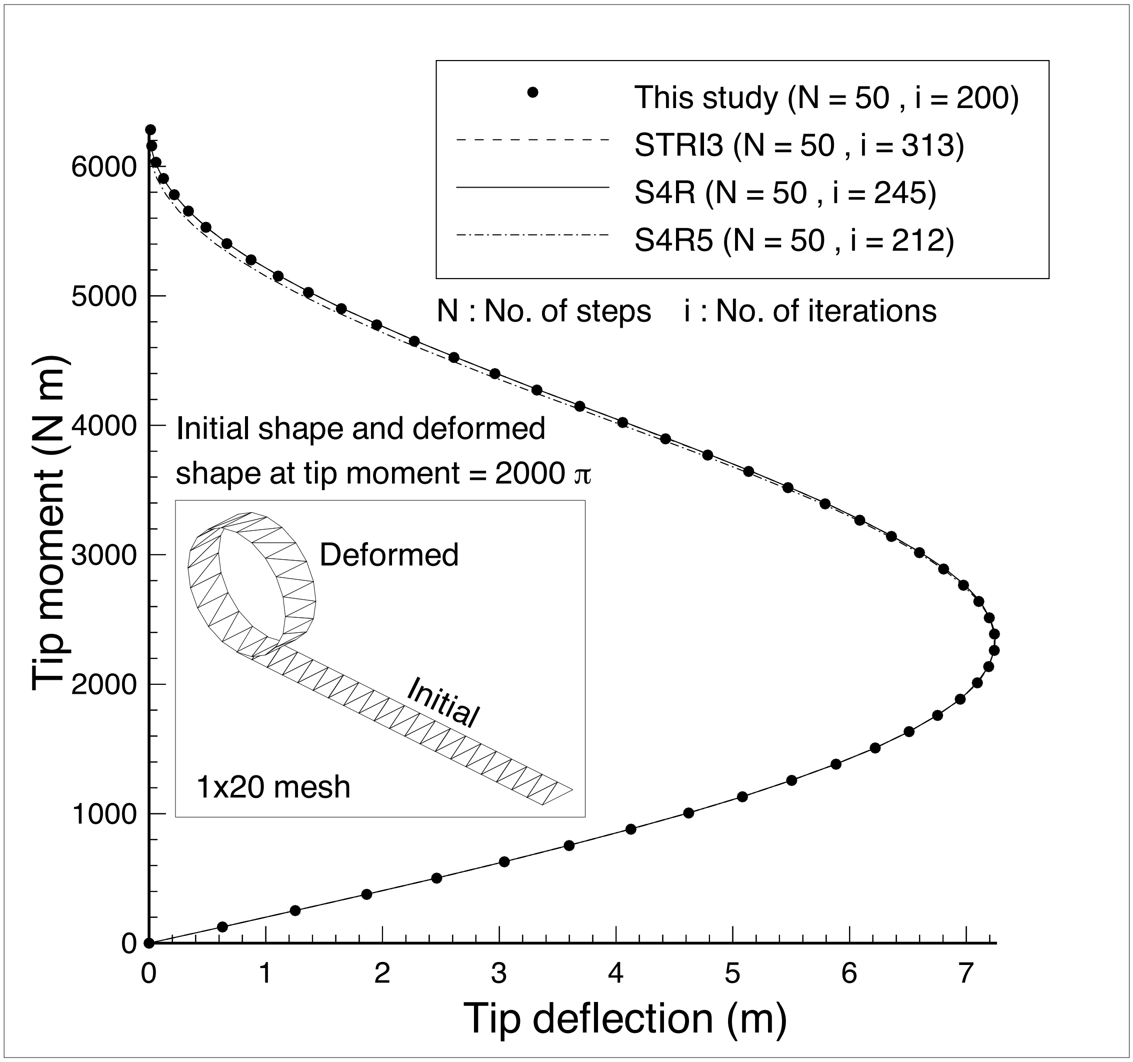

Figure 3.12: Cantilever beam under a tip moment.

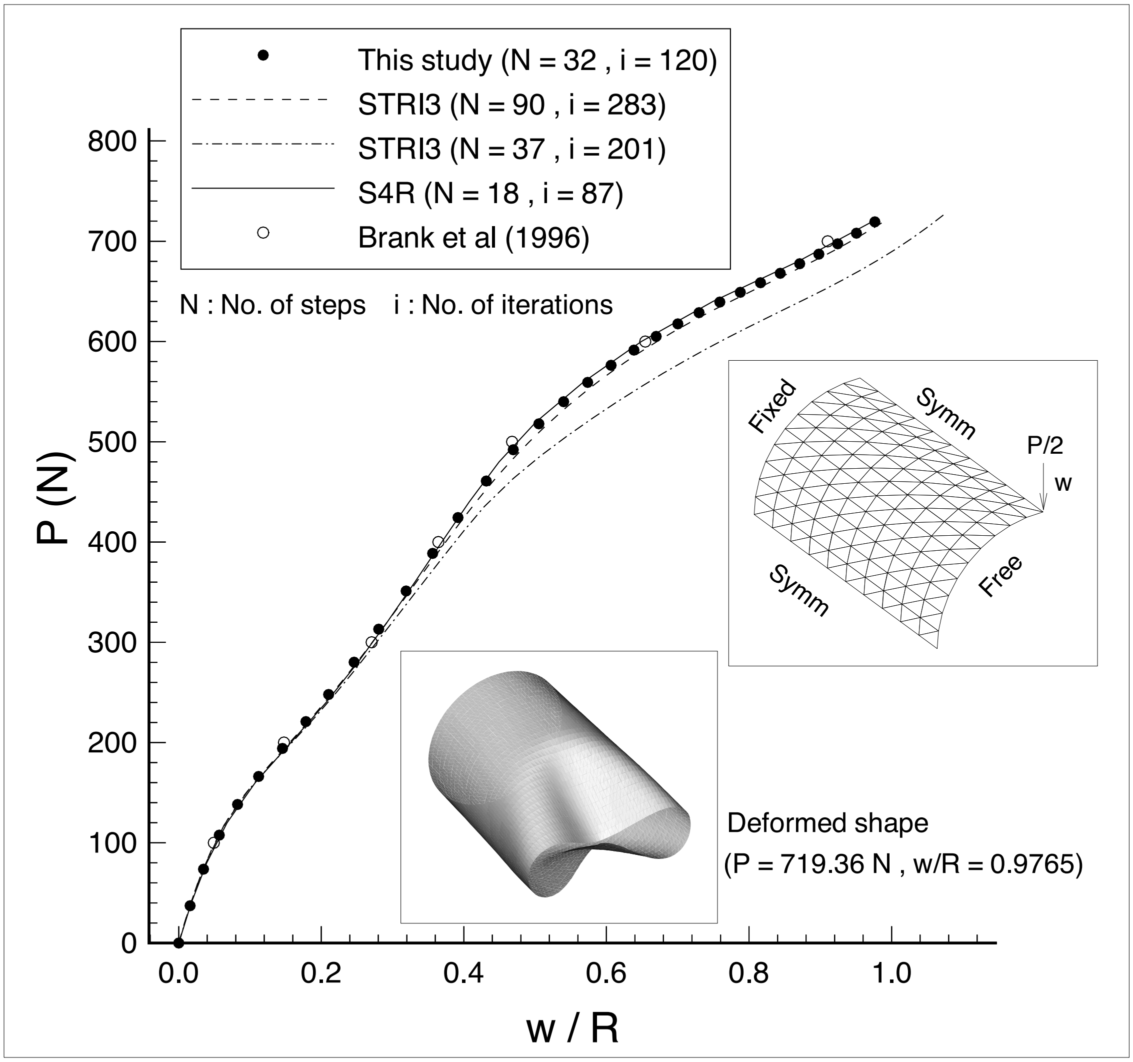

Figure 3.13: Clamped cylindrical shell under pinching loads (quarter shell model, 30x30 mesh).

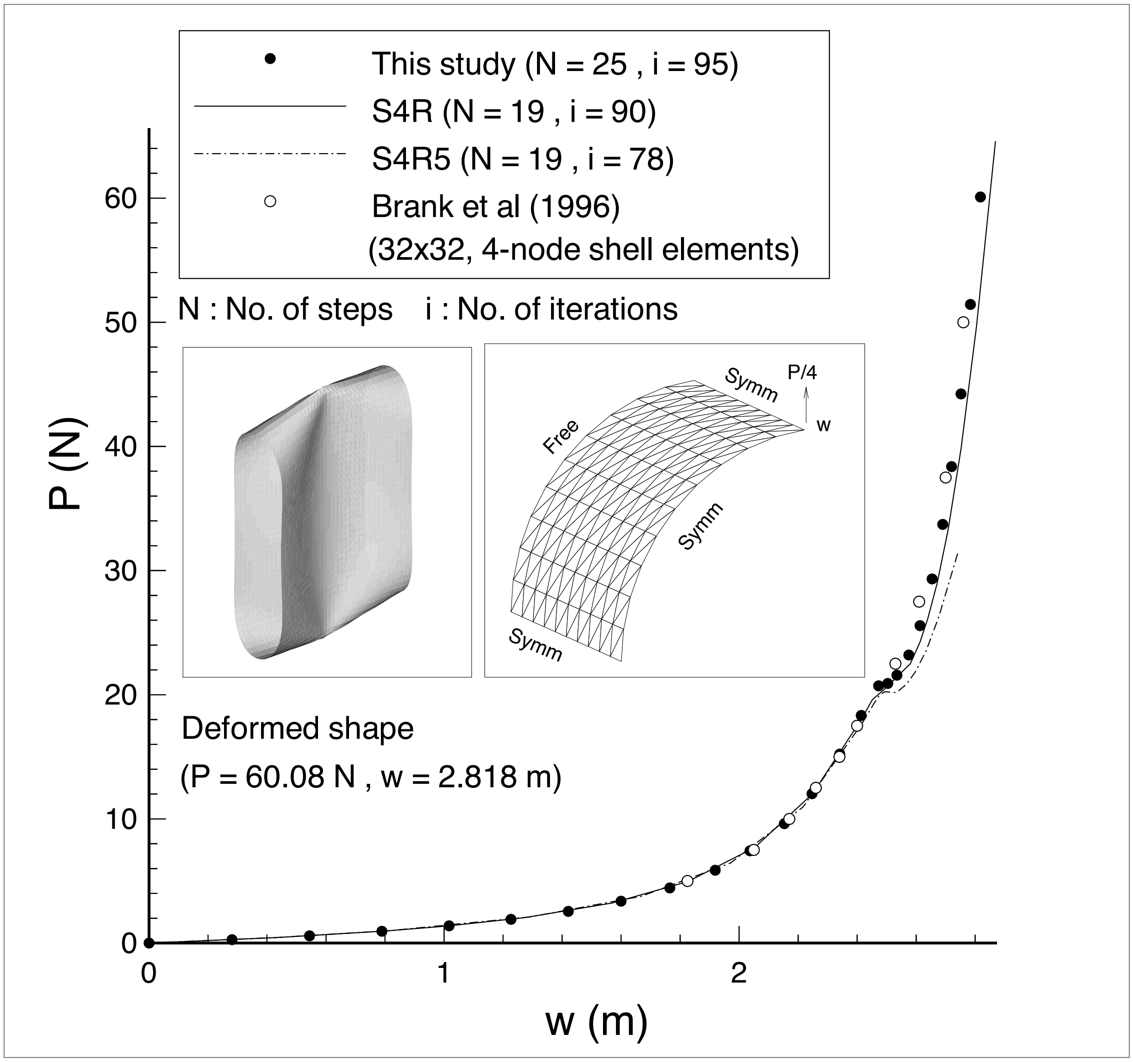

Figure 3.14: Cylindrical shell with free ends under stretching loads (1/8th model, 20x20 mesh).

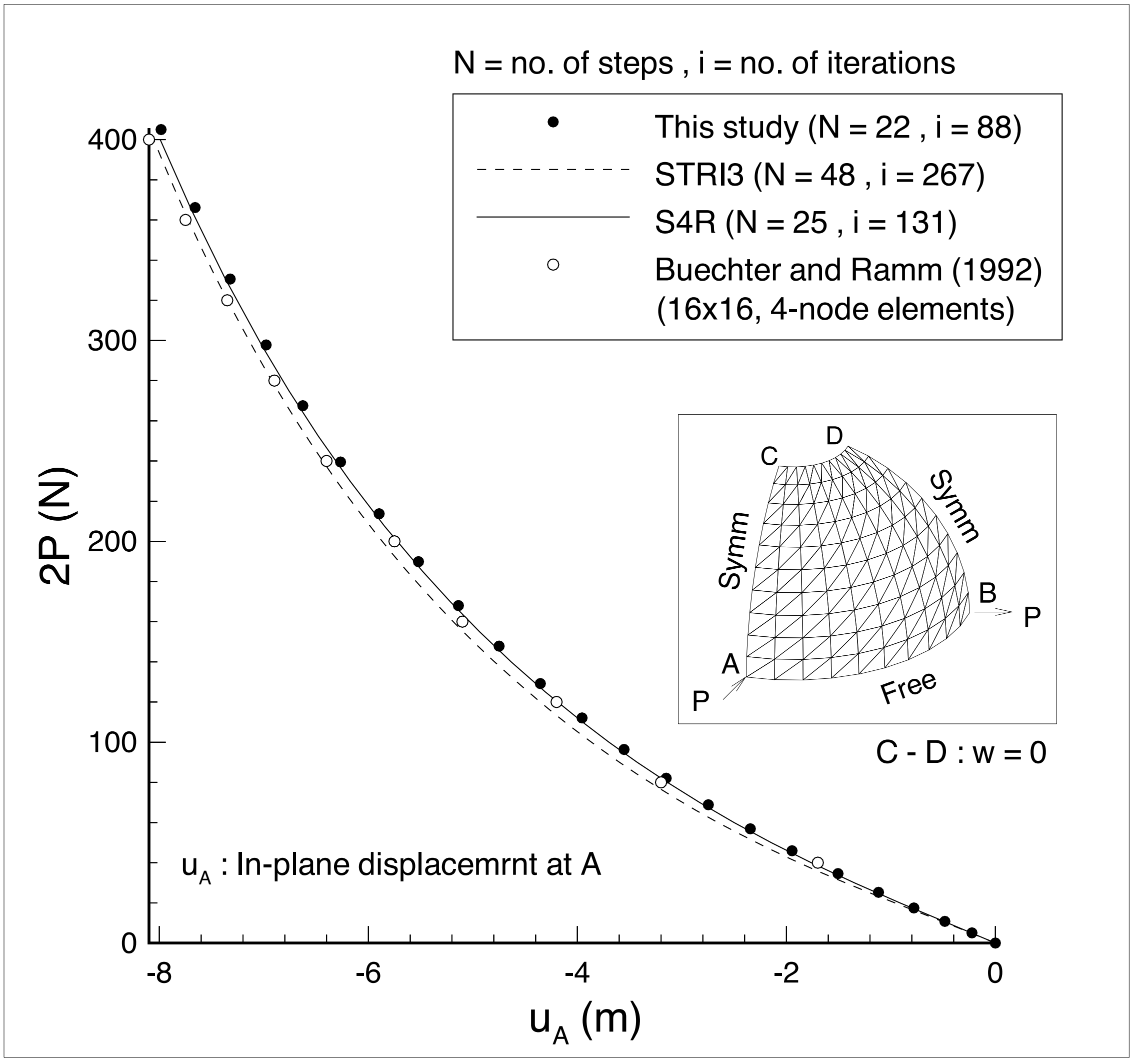

Figure 3.15: Hemispherical shell under pinching and stretching loads (u at point a, quarter shell model, 40x40 mesh).

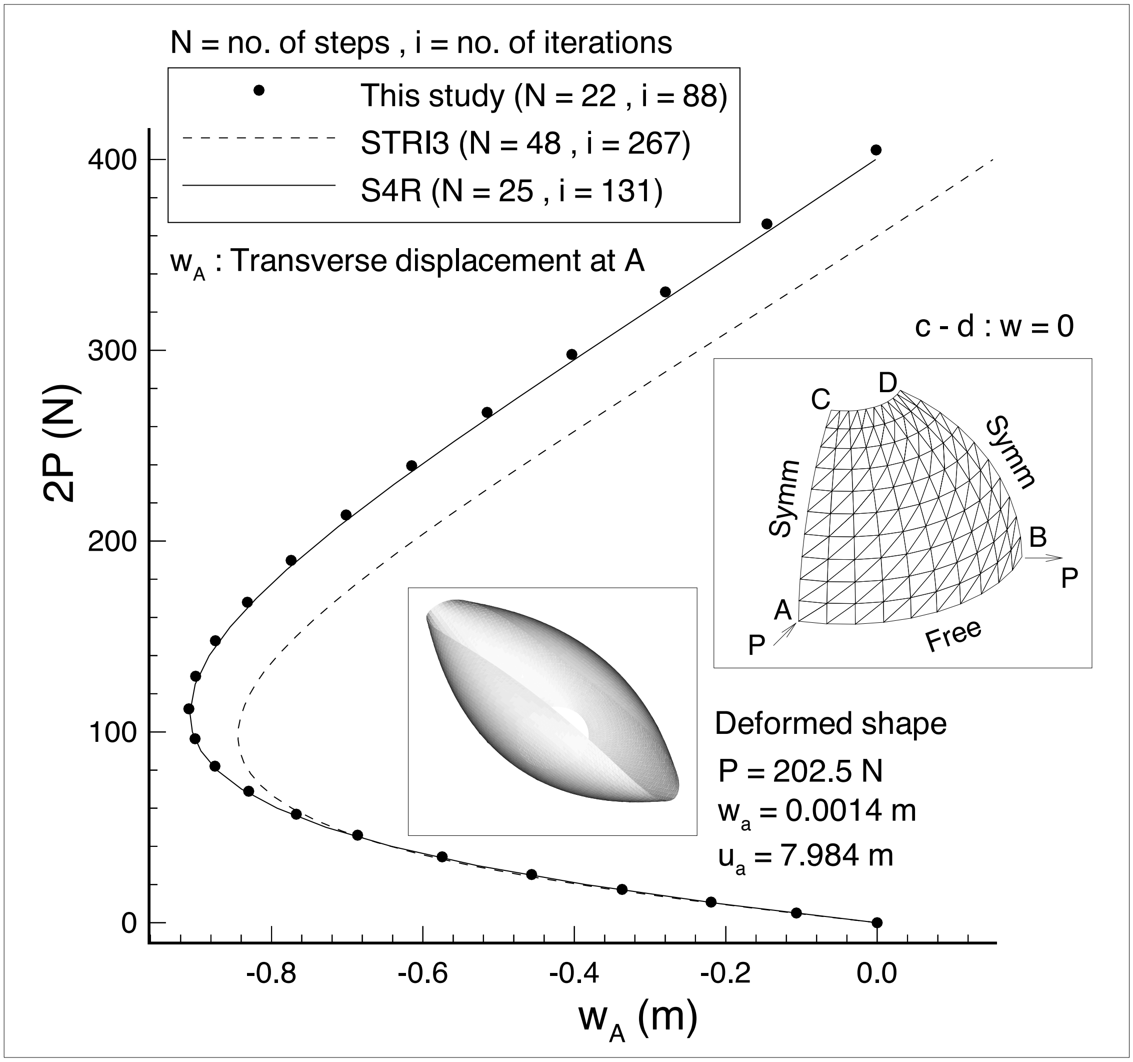

Figure 3.16: Hemispherical shell under pinching and stretching loads (w at point a, quarter shell model, 40x40 mesh).

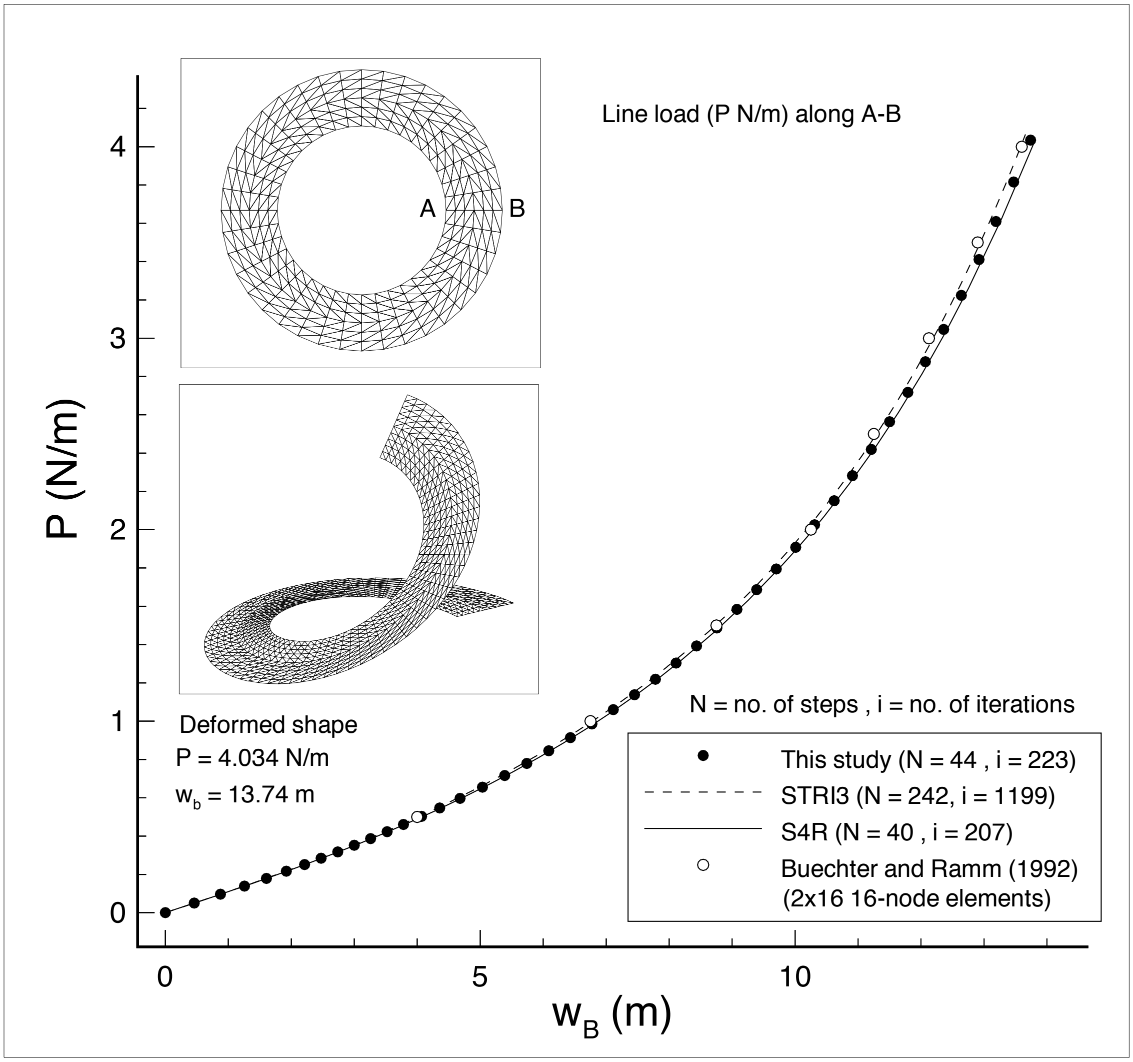

Figure 3.17: Ring plate under line load at the free edge (full plate, 10x80 mesh).

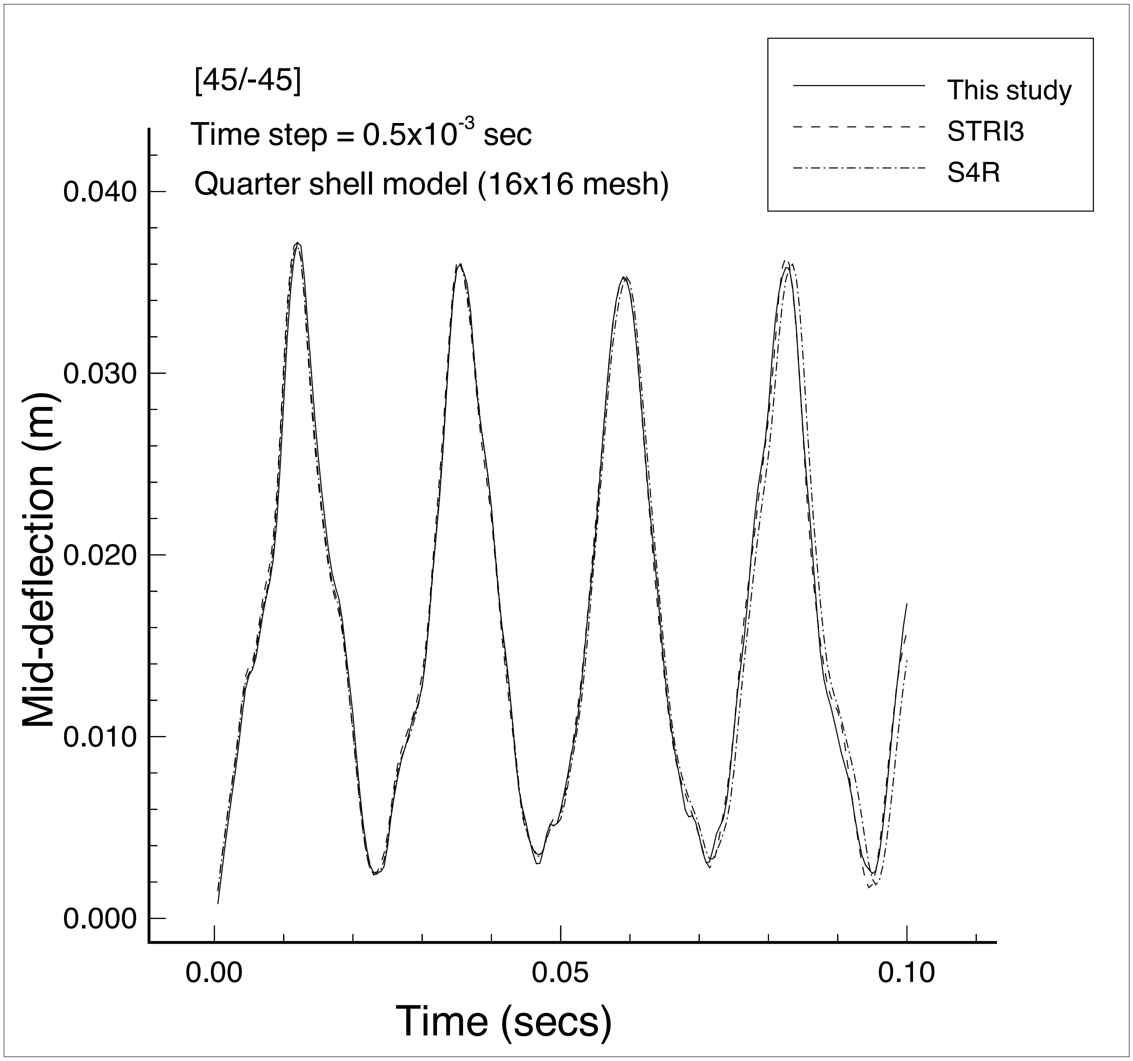

Figure 3.18: Dynamic analysis of an anisotropic ([45/-45]) hinged cylindrical panel under a concentrated load at the center.

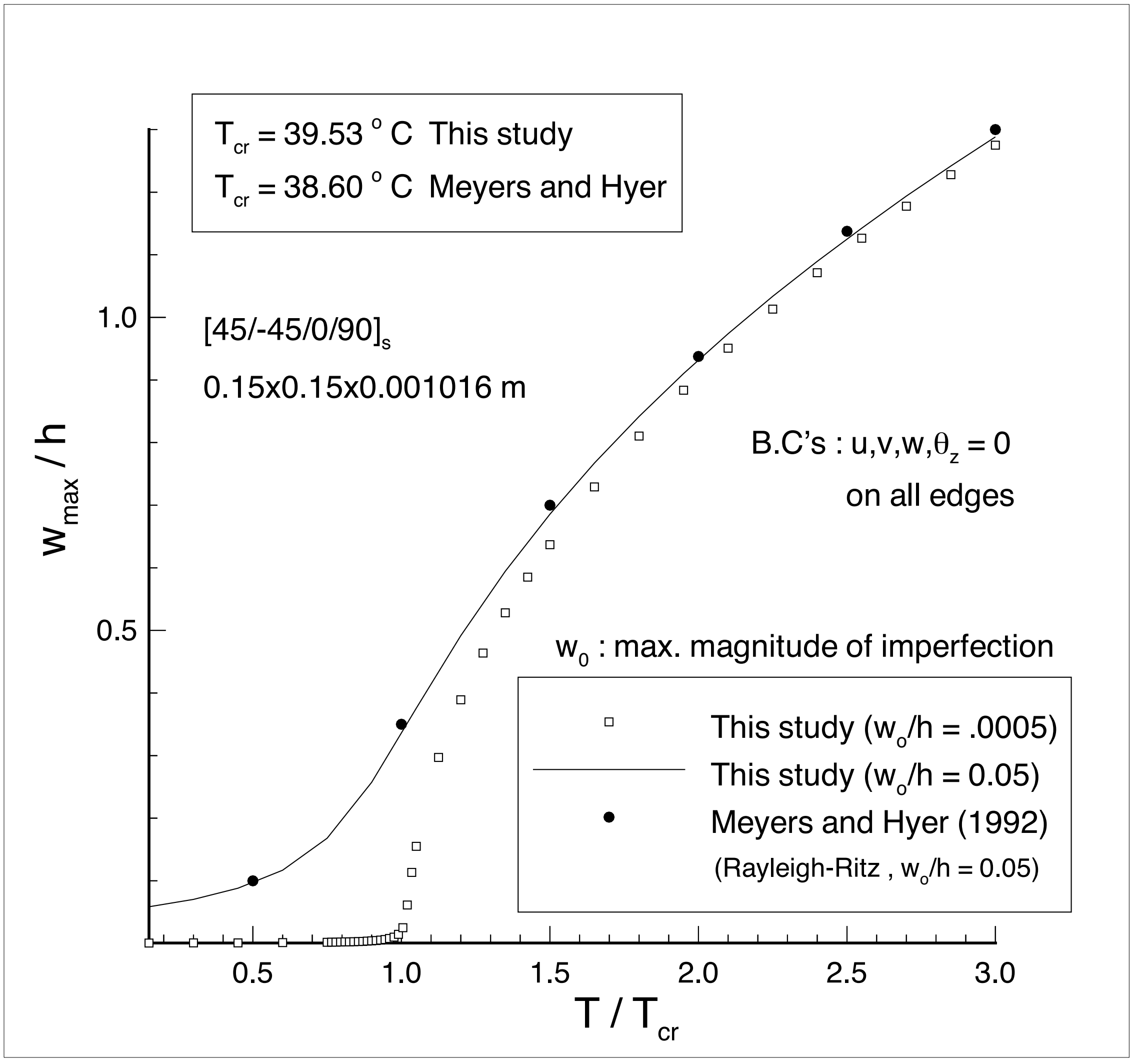

Figure 3.19: Thermal postbuckling analysis of a simply supported square plate under uniform temperature rise (full plate, 16x16 mesh).

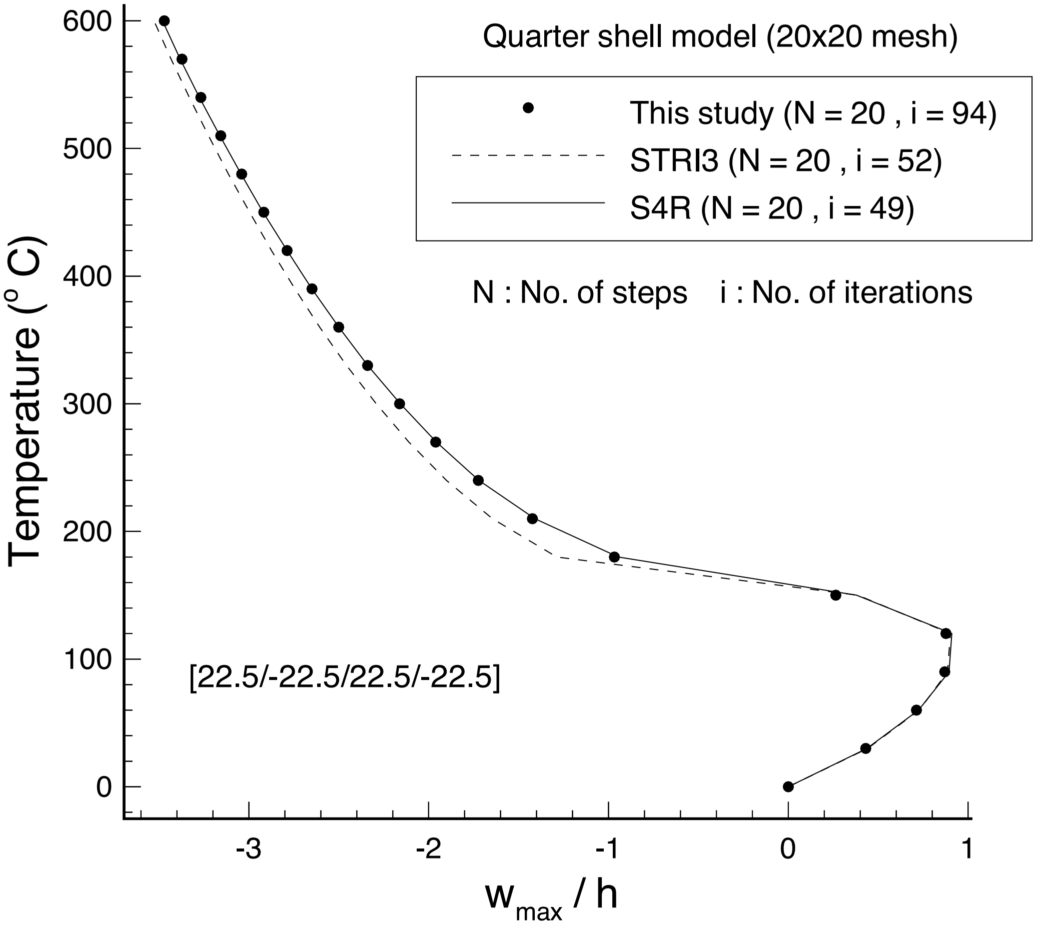

Figure 3.20: Thermal postbuckling analysis of a clamped cylindrical panel under uniform temperature rise.

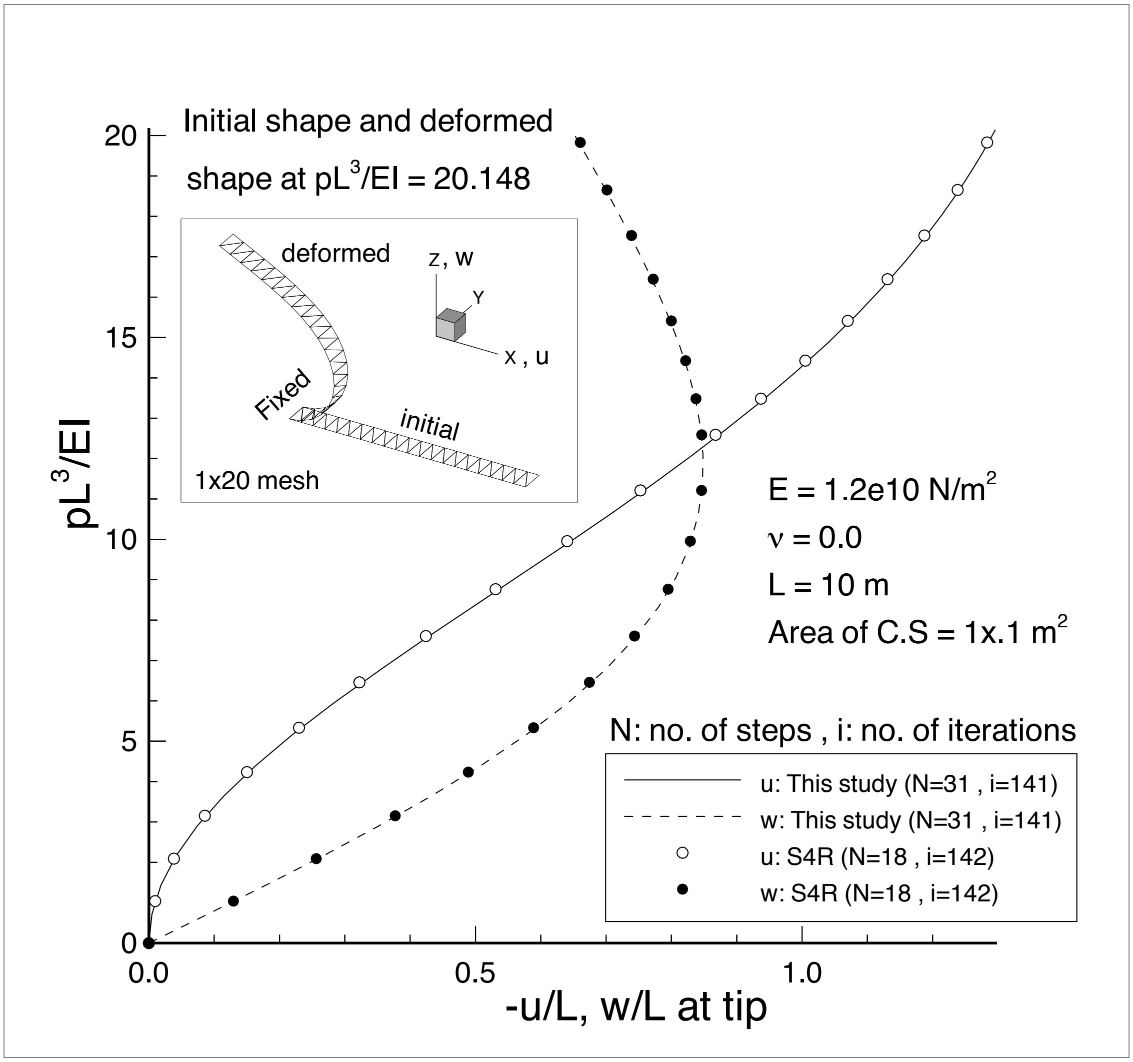

Figure 3.21: Cantilever beam under uniform external pressure.

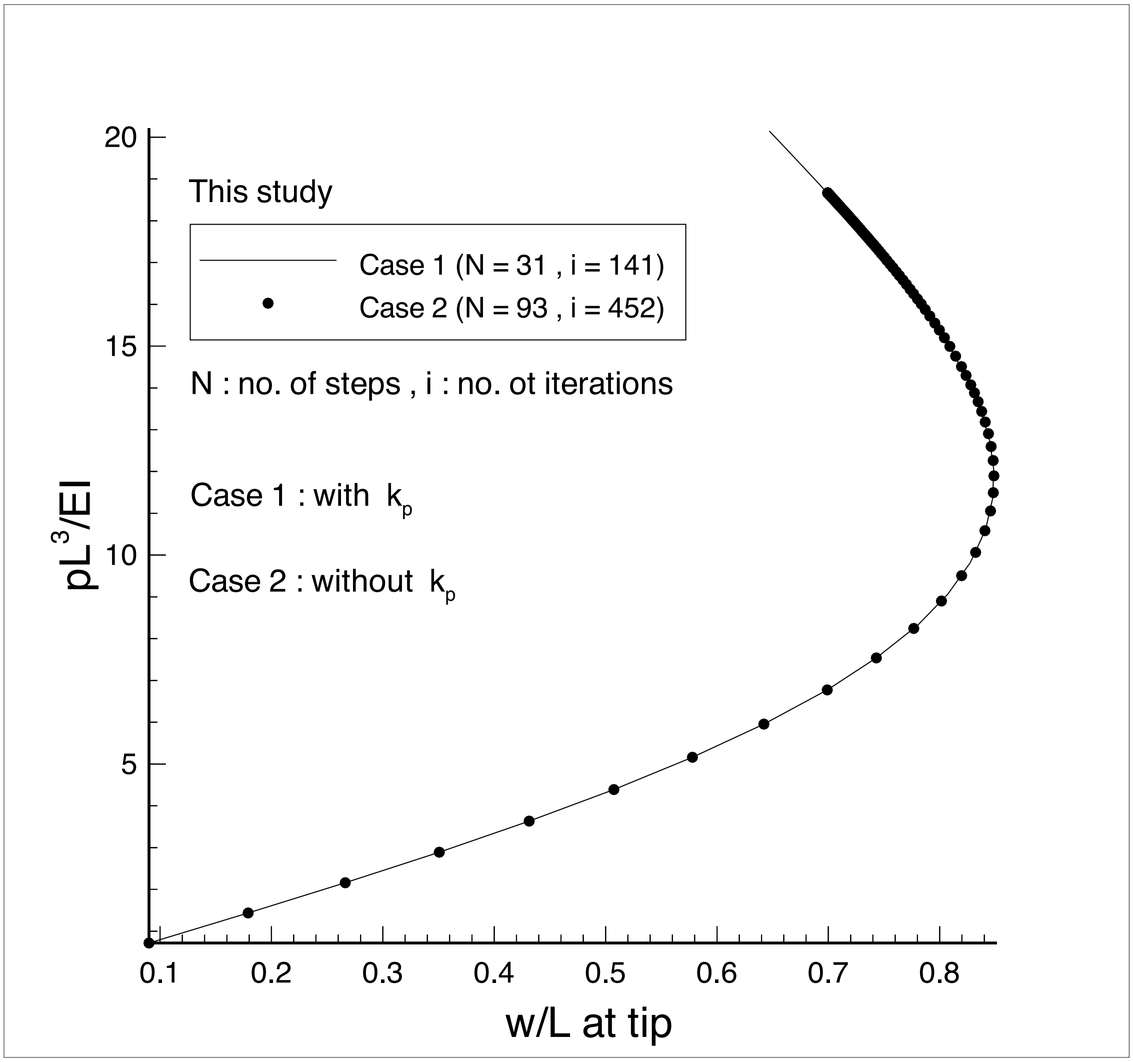

Figure 3.22: Cantilever beam under uniform external pressure (comparison of results obtained with and without pressure stiffness).

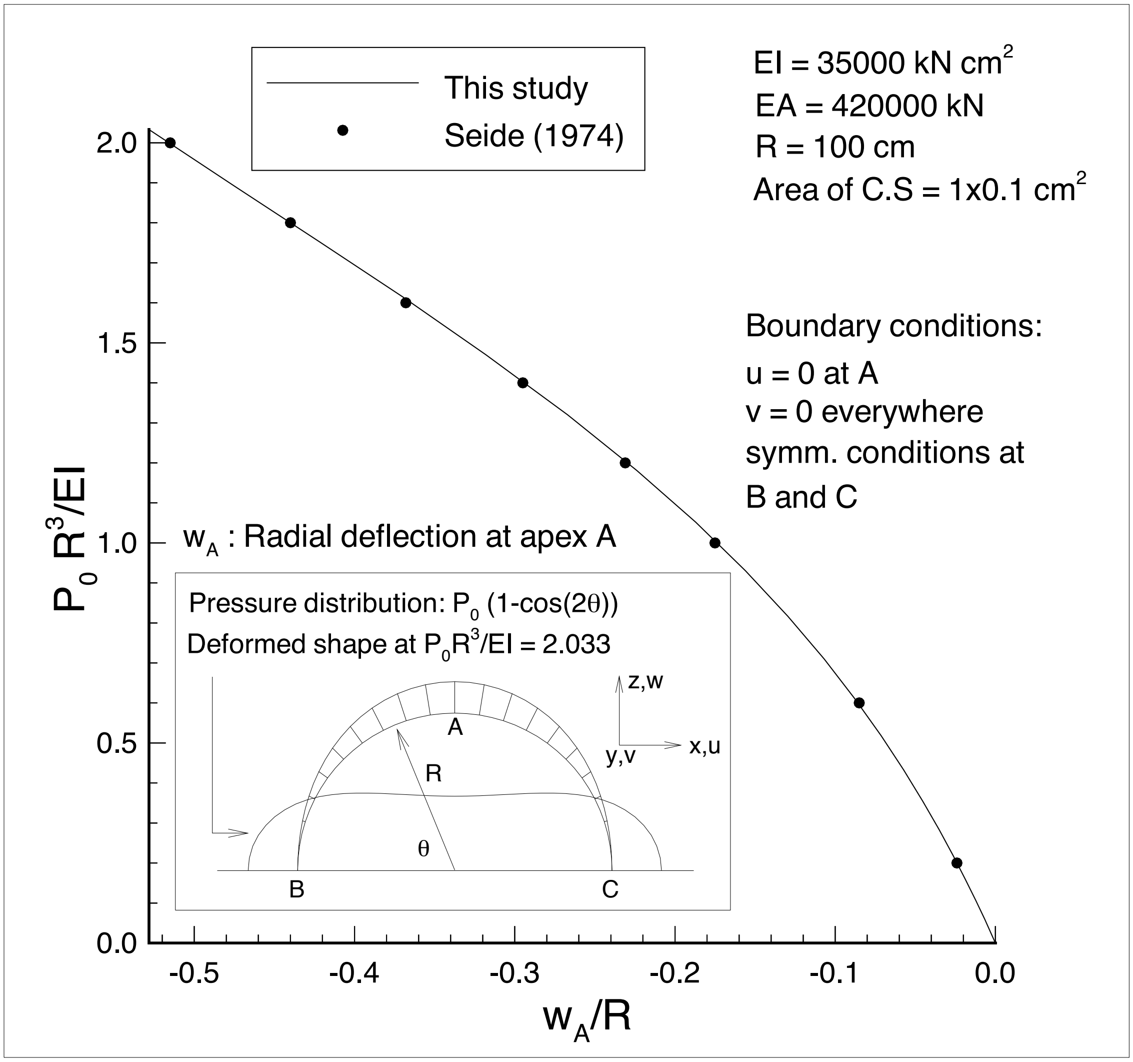

Figure 3.23: Thin circular ring under nonuniform pressure (half-ring model, 1x40 mesh, 80 elements).

# Chapter 4

# Shape Control of a Mirror Segment

## 4.1 Introduction and Literature Review

One of the most stringent requirements in the design of astronomical telescopes is the maintenance of the primary mirror surface to a very high degree of accuracy. The shape of the primary mirror has to be continuously monitored and any deviation from the desired shape caused by external disturbances needs to be controlled by applying corrective measures. Active control techniques are widely being adopted to correct the surface inaccuracies of optical surfaces. This involves correction of the surface deformation by applying control inputs using discrete or distributed actuation. In the case of discrete actuation, concentrated forces are applied at discrete locations on the deformed mirror using actuators that are located at the rear surface of the mirror. In the case of distributed actuation, strips of piezoelectric material are used as actuators. These strips are either bonded to the rear surface of the mirror or embedded in a composite mirror faceplate. Piezoelectric materials undergo mechanical deformation when an electric field is applied. The resulting induced distributed strain is used to control the surface deformation of the structure.

The active optics concept was first applied by Robertson *et al*. [91] to a 0.508 $m$ diameter, 3-segmented mirror. The mirror segments were aligned using 3 actuators per segment, which exerted control in piston and tilt only. Since the mirror segments were moved as rigid bodies the elastic deformations could not be controlled using such control techniques. The concept of thin deformable mirror was introduced by Robertson [92] who investigated analytically and experimentally the feasibility of controlling the shape of a 0.782 $m$ diameter 0.0127 $m$

thick spherical mirror using actuators that worked on the rear surface of the mirror. He used 58 equally spaced actuators to correct the surface error introduced during fabrication and mounting the mirror on the reaction support system. A finite element model was utilized to determine the actuator force configurations that would provide local displacements of the mirror at the actuator control points. The initial $rms$ figure error which was greater than 0.5 wavelength ($6328 \times 10^{-10}$ $m$) was corrected to within 0.02 wavelength.

Creedon and Lindgren [93] employed the modal expansion technique to represent the surface distortion of a flexible structure in terms of its natural vibration modes and countered the distortion by exerting control over a finite number of most significant modes. The actuators were located at the nodes of the next highest mode. They demonstrated this concept using flat rectangular and circular plates for which mode shapes are available in closed forms. Howell and Creedon [94] extended the modal expansion method to a 0.762 $m$ diameter 0.0127 $m$ thick spherical mirror used in the study by Robertson [92]. They used the first 58 modes for the modal expansion and 58 equally spaced actuators as was done by Robertson *et al*. [91]. The mode shapes were obtained using the finite element model similar to that used by Robertson [92]. The actuator locations resulting in minimum surface error were selected from the common nodes of a predetermined number of uncontrolled modes. Ostroff [95] presented an improved method for selection of actuator locations based on minimization of that part of the potential energy which is associated with the uncontrolled modes. Ostroff used the first 48 modes for the modal expansion of the surface distortion. The same finite element model which was used by Robertson [92] was employed but all the available nodal points were considered for positioning the actuators.

Scott [96] proposed a new method in which the correction of the surface distortion of the mirror was achieved by the application of moments at selected locations. An advantage of this method is that equal and opposite moments could be applied, eliminating the need for a rigid backup structure. Scott used a finite element model of a 0.254 $m$ flat disc to demonstrate the control of shapes in the form of the first 10 terms of the Zernike series, employing a maximum of 24 moment actuators. Bushnell [97] studied the effectiveness of concentrated loads in controlling the surface distortions of $4m$ diameter $0.01m$ thick spherical caps and circular plates using a finite difference model. Two different distortions, one due to a nonuniform thermal field given in terms of a few terms of the Zernike series and the other consisting of Zernike polynomials themselves, were considered in his study. As many as 100 actuators were used to bring down the initial *rms* surface error by 2 orders of magnitude. Bushnell found that mirrors with a very large diameter-to-thickness ratio and radius of curvature-to-thickness ratio are difficult to control.

Hansen *et al.* [98] presented an integrated active mirror system with 41 actuators in which a $4m$ diameter $0.02m$ thick spherical mirror was controlled in normal position, tangential slope and radial slope. In their analytical study employing a finite element model, the actuator system was evaluated to control deformations due to a thermal gradient through the thickness, uniform thermal soak of the entire system, gravity loads and optical aberrations like defocus and astigmatism. Hansen *et al.* [98] also found that thick mirrors are easier to control than thin mirrors. They also came to interesting conclusions that deformations due to bending loads like gravity or axial thermal gradient and deformations into shapes of nondevelopable surfaces (defocus) are difficult to control, whereas deformations due to membrane loads like a uniform rise in temperature and deformations into shapes of a developable surface (astigmatism) are easy to control.

Masaki *et al.* [99] performed shape control experiments using a 0.62 $m$ diameter 0.021 $m$ thick spherical mirror. They expressed the mirror deformations in the form of fundamental Zernike modes (astigmatism, coma and spherical aberration) in terms of the first 24 normal modes of the mirror and controlled only 7 or 12 out of the 24 observed modes using 9 force control actuators. The initial *rms* figure errors of the order of a few hundred nanometers could be reduced to about 18 $nm$ when 7 modes were controlled. When 12 modes were controlled the residual *rms* error was about 72 $nm$.

In the majority of the aforementioned works, the surface deformations were controlled by applying forces at discrete locations on the rear surface of the mirror. A major drawback of using such discrete devices is the requirement of a rigid and consequently heavy support structure which is undesirable for space applications. An alternative to this approach is to use piezoelectric actuators which can be very lightweight and do not require a heavy backup structure. Kuo and Bruno [100] investigated the problem of determining the optimal locations of piezoelectric actuators to control surface distortions of a one meter hexagonal flat panel using a modified simulated annealing technique. They used two types of distortions, one a linear combination of first the 3 normal modes and another a linear combination of first the 5 normal modes, both having a maximum deformation of 5 microns in each mode. The optimization was performed several times using different starting configurations to determine the optimal configuration. They found that strips placed in the radial directions appeared in almost every run. Hence a configuration with actuators placed along 6 radial lines resulting in 24 actuators was used to control both types of distortions. Using such a configuration, the $rms$ error in the first case was reduced to 0.0305 microns and in the second case to 0.3529 microns. As can be seen from the results obtained by Kuo and Bruno [100], the configuration of radially located piezoelectric actuators does not seem to be very effective in controlling complex surface distortions of the mirror segment.

In a subsequent study, Kuo [101] used a similar configuration with 6 radial groups of 5 actuators in each group to excite the first 3 natural modes of vibration of the panel and experimentally verified the numerical results obtained using the NASTRAN program. Using the same configuration, Kuo [102] performed experiments on a 0.5 $m$ diameter, 0.025 $m$ thick curved hexagonal mirror segment, demonstrating that by applying different voltages to the six groups of actuators, the mirror could be deformed into shapes that are similar to the first 8 Zernike polynomials.

Though the numerical and experimental work done by Kuo and Bruno [100] and Kuo [101],[102] demonstrate the use of piezoelectric actuators to control the surface distortions of a mirror segment, the results presented do not give an indication of the effectiveness of the configuration of radially located actuators in controlling complex surface distortions of the mirror segment.

In the present work, control of thermal deformations of a 0.5 $m$ hexagonal curved mirror, 0.012 $m$ thick, with a radius of curvature of 10 $m$, using discrete and distributed actuators is presented. The mirror segment used is part of a multisegmented primary mirror of a next generation space telescope proposed by Jakubowski *et al.* [65]. A finite element model is used to represent the mirror-actuator system. In order to study the effectiveness of the discrete and distributed actuators, a comparative study is conducted using two different models of the mirror-actuator system. In Model-1 the mirror is mounted on kinematic supports and controlled by piezoelectric strips that are bonded to the rear surface of the mirror. Two sets of strip configurations are studied. One with radially placed strips similar to that employed by Kuo and Bruno [100] and the other with evenly distributed strips. In Model-2 the mirror is mounted on force actuators which are used to support the mirror as well as control the surface deformations of the mirror. The optimal values of the forces that are to be applied at the actuator control points and the voltages to be applied across the piezoelectric strips are determined by minimizing the *rms* surface figure error. A study is also conducted to compare the performance of evenly distributed strips to that of strips placed at near optimal locations obtained using heuristic integer programming. Details of the analysis and the results are presented in the following sections.

## 4.2 Finite Element Model

The mirror is modeled using an assembly of flat triangular shell elements described in Chapter 2. The piezoelectric strip is also modeled using the same flat triangular shell element, but as a separate layer of isotropic material bonded to the lower surface of the mirror. The force actuator is modeled using a 2-node beam element (Hughes [105]). The beam element has bending rigidity in 2 orthogonal planes normal to its longitudinal axis, extensional rigidity along its longitudinal axis and torsional rigidity about its longitudinal axis giving a total of 6 degrees of freedom per node (3 translations and 3 rotations). Shear deformations are also included in the beam formulation. One end of the actuator or the beam element is constrained in all degrees of freedom to simulate the rigid backup structure and the other end is connected to the mirror where the control force is applied. Thermal deformations of the force actuators have not been considered in this study. Also the thermo-elastic coupling in the mirror and the force actuators and the piezo-thermo-elastic coupling in the piezoelectric strips have been neglected.

To demonstrate the correctness of the finite element formulation, an example of a Graphite/Epoxy square plate and a piezoelectric bimorph cantilever beam are presented. Several examples of plates and shells under mechanical and thermal loads have already been presented in Chapter 3 and hence are not reproduced here.

*Graphite/Epoxy laminate under an electric field:* The plate is made of 8 layers ($[0/90/0/90]_s$) of graphite/epoxy material and a 9th layer of piezoelectric polymer material, polyvinylidene fluoride (PVDF) twice as thick as the other 8 layers. The plate is simply supported (BC1 of Chapter 3) on two opposite edges and clamped on the other two edges. A constant voltage ($E_z\ V/m$) is applied across the PVDF layer. The properties of the graphite/epoxy laminate (Jonnalagadda *et al.* [103]) are $E_1 = 181\ GPa$, $E_2 = 10.3\ GPa$, $G_{12} = 7.17\ GPa$, $\nu_{12} = 0.28$, $\alpha_1 = 0.02\text{x}10^{-6}/^oC$, $\alpha_2 = 22.5\text{x}10^{-6}/^oC$ and $\alpha_{12} = 0$. Material properties for the PVDF layer (Jonnalagadda *et al.* [103]) are $E_1 = E_2 = 2\ GPa$, $G_{12} = 0.752\ GPa$, $\nu_{12} = 0.33$,

$d_{31} = d_{32} = 23e^{-12}m/V$ and $d_{33} = 33e^{-12}m/V$, where $d_{31}$ and $d_{32}$ are the piezoelectric strain coefficients which correspond to the in-plane strains that are induced due to a constant electric field applied in the transverse direction. Note that the coefficient $d_{33}$ corresponds to the strain in the transverse direction and does not appear in the plane stress relations. The author understands that it has been used by Jonnalagadda *et al.* [103] only to non-dimensionalize the mid-deflection. The convergence of the non-dimensionalized center plate deflection is given in Table 4.1 along with the results of Jonnalagadda *et al* [103] and are in good agreement.

*Piezoelectric bimorph cantilever beam:* The beam (0.1 $m$ x 0.005 $m$ x .001 $m$) is made of two layers of PVDF material with opposite polarity. A constant voltage of 1000 V/m is applied across the thickness. The material properties are the same as those used in the previous example, except that the Poisson ratio used in this case is zero. A 1x20 mesh (40 elements and 42 nodes) was used to model the beam. The average of the transverse deflection at the nodes along the two edges of the beam, at 5 locations along the beam, are presented in Table 4.2 along with the analytical solution and finite element results (obtained using 10 solid isoparametric elements, 5 per layer) given by Tzou and Tseng [104]. The present results agree well with the analytical solution given by Tzou and Tseng. The finite element results of Tzou and Tseng based on an isoparametric solid element formulation are stiffer compared to the analytical solution or the present results.

The mirror-actuator model was verified using an example of an L-frame fixed at the 2 ends and subject to concentrated forces $P_x, P_y, P_z$ at point A (Fig 4.1) along the X, Y, Z axes, respectively (Fig. 4.1), and a moment $M_y$ at point A, about the Y-axis. The horizontal member (member-1) of the L-frame was modeled using the flat shell elements with a Poisson's ratio of zero and the vertical member (member-2) was modeled using the beam element. The results were compared with those obtained using Castigliano's principle, those obtained by modeling the horizontal member using the B33 2-node Euler-Bernoulli beam element and the vertical member using the B31 2-node Timoshenko beam element of the commercial finite element package ABAQUS and those obtained by modeling the horizontal member using the 3-node flat shell element STRI3 of ABAQUS and the vertical member using the B33 element. The STRI3 element of ABAQUS is a combination of the DKT plate bending element and the Constant Strain Triangular (CST) element. The combination of STRI3 and B33 was used mainly to compare the in-plane deformations, as those obtained using

Castigliano's principle or the beam elements (B33 and B31) are not expected to agree with those obtained by modeling the horizontal member using the shell elements. The results are presented in Table 4.3, where $u_x, u_y$ and $u_z$ are the displacements along the X, Y and Z axes, respectively. The present results are in good agreement with the rest of the results presented in Table 4.3, demonstrating the validity of the present mirror-actuator model.

## 4.3 Control Algorithm

The surface deformations of the mirror segment are corrected by applying control inputs to the force actuators and the piezoelectric strips which act upon the rear surface of the mirror. In the present study, control input for the force actuator is the concentrated force that is to be applied normal to the rear surface of the mirror at the grid points where the force actuator is attached to the mirror. In the case of the piezoelectric strips, the control input is the voltage to be applied across the thickness of the strips, which induces a distributed strain in the strips and hence in the mirror, assuming that the strips are perfectly bonded to the mirror. Since the number and locations of the force actuators and piezoelectric strips are predetermined, the shape control problem involves the determination of the optimum values of actuator forces or the voltages with which a maximum possible correction can be obtained.

Consider a mirror approximated by $m$ nodal points using the finite element model. Let $\psi$ denote the deformed shape or the transverse displacements and $u$ the correction to the transverse displacement applied using $n$ force actuators or piezoelectric strips. In this study the deformed shape $\psi$ is assumed to be known. The deformed shape or the mirror figure error can be estimated using the Shack-Hartmann wavefront analyzer [99]. For details the user is directed to Ref. [99] and the references therein. It suffices to mention here that the wavefront analyzer estimates the deformed surface of the mirror by measuring the light emitted from the mirror. From the measurements made, the mirror surface is expressed in terms of Zernike polynomials using a suitable curve fit and thus the mirror figure error at any location is available as a linear combination of the Zernike polynomials. Though the Zernike polynomials do not correlate to the mechanical characteristics of the mirror like the natural mode shapes, they have been widely used in the existing literature to represent the shape of the mirror. Masaki *et al.* [99] have showed that the lower Zernike modes are similar to the natural modes of a spherical mirror and hence the mirror deformations can be expanded in terms of the lower Zernike modes instead of the natural modes.

The correction $u_i$ at any nodal point is given by

$$u_i \;=\; \sum_{j=1}^{n} \alpha_{ij} f_j \tag{4.1}$$

where $f_j$ is the force applied at the $jth$ actuator location or the voltage applied across the $jth$ piezoelectric strip and $\alpha_{ij}$ is an influence coefficient defined as the deformation caused at node $i$ due to a unit force applied at the $jth$ actuator alone or a unit voltage applied across the $jth$ piezoelectric strip alone. It is assumed that the material of the mirror, force actuators and the piezoelectric strips is linear-elastic and isotropic. Since the deformations considered in this study are of the order of a few micrometers, the geometric and material nonlinearities are less significant and hence the superposition used in Eq. (4.1) is justified.

A matrix of influence coefficients of size $m$x$n$ is obtained from the finite element model by applying a unit load at each node where the actuator is attached to the mirror or by applying a unit voltage across each of the piezoelectric strips, one at a time. The correction $u_i$ thus obtained, when applied against the deformed structure, tends to nullify the deformations. In order that the best possible correction is obtained, the deviation from the desired shape should be made minimum at every point on the structure. Since the structure is modeled as a set of finite number of nodal points, it is required that the deviation at these nodal points be minimum. A measure of the overall deviation or the *rms* figure error is given by

$$E \;=\; \sqrt{\frac{1}{m}\;\sum_{i=1}^{m} (\psi_i \;+\; u_i)^2} \tag{4.2}$$

Substituting Eq. 4.1 in Eq. 4.2, the *rms* error can be expressed in terms of the unknowns $f_j$ as follows:

$$E \;=\; \sqrt{\frac{1}{m}\;\sum_{i=1}^{m} (\psi_i \;+\; \sum_{j=1}^{n} \alpha_{ij} f_j)^2} \tag{4.3}$$

Setting $\partial E / \partial f_k \; = 0$ gives

$$\sum_{i=1}^{m} (\psi_i \;+\; \sum_{j=1}^{n} \alpha_{ij} f_j) \alpha_{ik} \;=\; 0 \quad k = 1, 2 \ldots . n \tag{4.4}$$

Eq. 4.4 is of the form $[A]\{f\} = \{b\}$, where $A_{kj} = \sum_{i=1}^{m} \alpha_{ij}\alpha_{ik}$, $b_k = -\sum_{i=1}^{m} \psi_i \alpha_{ik}$. The solution of this set of equations, obtained using the standard $LDL^T$ direct factorization, gives the values of forces to be applied at $n$ actuator locations or the voltages to be applied across $n$ piezoelectric strips for which the best possible correction can be obtained. Since the material is assumed as linear-elastic, the control inputs thus obtained are those that cause the undeformed mirror to deform to the shape given by $\psi$. The control inputs thus obtained will have to be applied in the opposite direction, on the deformed mirror, in order to obtain the necessary correction.

The control algorithm was validated by using the deformed shape due to arbitrary loads applied at a few nodal points and that due to arbitrary voltages applied across a few piezoelectric strips. The optimal values of the forces and the voltages obtained using the control algorithm were exactly the same as those used to generate the deformed shape.

## 4.4 Results and Discussion

The aforementioned algorithm is applied to control the thermal deformations of a spherical mirror segment with a hexagonal base. The geometry and material properties of the mirror, piezoelectric strip (Ha *et al.* [106]) and force actuator are given in Table 4.4. The temperature distribution at the lower surface of the mirror is assumed to be in the form of a linear combination of the first few terms of the Zernike series (Pearson and Stepp, [107]) expressed in terms of Cartesian coordinates $x, y$ with the origin at the center of the mirror. The Cartesian coordinates used to express the temperature distributions are normalized such that they are in the range [-1,1]. The temperature distributions that are considered in this study are given in Table 4.5, where the constant $C$ is used to scale the temperature distributions such that the upper, light-reflecting surface is at a lower temperature than the lower surface with a constant temperature difference $\Delta T_z^o$ C, and the maximum temperature difference between any two grid points across the lower surface of the mirror is $\Delta T_{xy}^o$ C.

The finite element mesh for Model-1 (Fig. 4.2) consists of 864 flat shell elements and 469 grid points. The mirror in Model-1 is supported at the 6 vertices: 1, 13, 223, 247, 457 and 469. The translational degrees of freedom are constrained at the supports. It is preferable to support the mirror on all six vertices than three vertices 120 degrees apart. This is because the edge deformations in the former case resemble those of a simply supported beam and are easier to correct than the cantilever type deformations along the edges in the latter case. The thermal deformations are controlled using piezoelectric strips bonded to the lower surface of the mirror. Two sets of configurations of the strips are considered, one with 30 radially placed strips (Fig. 4.3) similar to the configuration used by Kuo and Bruno [100] and the other with 121 evenly distributed strips (Fig. 4.3). It was observed that better control could be achieved by adding strips near the periphery to a set of 79 evenly distributed strips (Fig. 4.3) resulting in a set of 121 evenly distributed strips as shown in Fig. 4.3. Since the piezoelectric strips are very light and flexible, a large number of such strips can be used without drastically increasing the overall weight or stiffness of the mirror unlike the conventional force control actuators. The configuration with 121 strips as shown in Fig. 4.3 consists of 37 hexagonal strips and 84 semi-hexagonal strips. Each hexagonal strip has a side of 0.04166 $m$. The optimal locations are determined from a starting configuration of 193 strips (Fig. 4.3) consisting of 91 hexagonal strips and 102 semi-hexagonal strips. The heuristic algorithm used to determine the (near) optimal locations is described later in this section.

In the case of radially placed and evenly distributed strips, the influence coefficients are determined by applying a unit voltage across each strip, one at a time, in the presence of all other strips. In order to determine the optimal locations of the strips, an approach similar to that followed by Kuo and Bruno [100] is used. The influence coefficients are first determined by neglecting the stiffness of the strips in computing the global stiffness matrix. If the stiffness of the strips is included in the global stiffness matrix for determining the influence coefficients, each set of influence coefficients would correspond to a different global stiffness matrix and hence the linear combination of the sets of influence coefficients thus obtained will not correspond to any one stiffness matrix. In other words, the influence coefficients are determined by applying a unit voltage across each of the strips, one at a time, in the absence of the rest of the strips.

The optimal locations of the strips are obtained using the Dlorenzo algorithm given by Haftka and Adelman [108]. This algorithm has been chosen as it does not require any initial guess of the locations as in other optimization techniques like simulated annealing [100]. More exhaustive integer programming methods are available in the literature (Haftka and Adelman [108]), but they are computationally much more expensive than the Dlorenzo algorithm and they also have a certain degree of uncertainty due to the requirement of initial guess locations.

The Dlorenzo algorithm starts with an initial configuration of 193 strips as shown in

Fig. 4.3. The steps followed in the algorithm are as follows: 1. Remove each one of the strips from the initial configuration of $n$ strips (n=193), one at a time, and determine the $rms$ error due to $n$ configurations of $n-1$ strips. 2. Rank the strips in ascending order of the $rms$ error. 3. Remove the strip which results in the least $rms$ error, to obtain a new configuration of $n-1$ strips. 4. Repeat steps 1-3 until the desired number (30 or 121) of strips is reached. The configuration thus obtained is called the optimal configuration in the subsequent sections though it is certainly not the best possible configuration.

The thermal deformations of Model-1 are computed by neglecting the stiffness of the strips. The $rms$ and absolute values of the transverse deformation of Model-1 without the strips and with 30 and 121 strips are given in Table 4.6 for $\Delta T_z$=0.2 $^o$ C and $\Delta T_{xy}$=0.5 $^o$ C. As can be seen from Table 4.6, there is not much difference in the $rms$ and absolute maximum deformations of the mirror without the strips and with 30 and 121 strips. This can be attributed mainly to the fact that the thickness and the stiffness of the strips are much lower than those of the mirror. Hence neglecting the stiffness of the strips in determining the optimal locations is not expected to give erroneous results. Moreover, as the deformed shape of the mirror without the strips did not vary significantly from that in the presence of the strips, the optimal locations obtained as mentioned above could be used to control the deformed shape in the presence of the strips. After determining the optimal locations as mentioned above, the influence coefficients are computed now by including the stiffness of the strips as done in the case of radial and evenly distributed strips.

The corrected $rms$ figure error and the maximum residual deformations for Model-1 using 30 radially placed strips and 30 optimally placed strips for $\Delta T_z$=0.2 $^o$ C and $\Delta T_{xy}$=0.5 $^o$ C are given in Table 4.7. The optimal voltages to be applied to 30 strips varied from -558 V to 389 V in the case of radially placed strips, and in the case of optimally placed strips the voltages varied from -1312 V to 853 V. The negative sign indicates that the voltage is applied in the direction opposite to the direction of polarization of the piezoelectric material. The corrected $rms$ figure error and the maximum residual deformations for Model-1 using 121 evenly placed strips and 121 optimally placed strips for $\Delta T_z$=0.2 $^o$ C and $\Delta T_{xy}$=0.5 $^o$ C are given in Table 4.8. The optimal voltages to be applied to 121 strips varied from -983 V to 547 V in the case of evenly placed strips, and in the case of optimally placed strips the voltages varied from -1159 V to 1242V. The optimal locations of 30 and 121 strips are shown in Figures 4.4 and 4.5, respectively.

The surface distortions could not be reduced much using 30 radially placed strips. The poor performance of 30 radially placed strips can be attributed to the fact that the influence of the strips is restricted to a certain area, unlike the case of evenly distributed strips. Even using 30 (near) optimally placed strips, the percentage reduction in the *rms* figure error or the maximum residual deformation seems insufficient in the case of complex deformations T2 and T3 (Table 4.7). The performance of 121 evenly distributed strips (Table 4.8 ) is quite close to that of 121 (near) optimally placed strips. The amount of correction obtained in the case of asymmetric thermal fields T2, T3 and T4 indicate that the performance of 121 evenly distributed strips is not biased towards symmetric deformations or symmetric support conditions. The corrected *rms* values given in Table 4.8 for 121 evenly distributed strips range from 81 *nm* to 97 *nm*. The *rms* figure error of the surface distortions of the mirror segment of the next generation space telescope (Jakubowski [65]) should be within 1/20th of the operating wavelength (0.5 $\mu m$) in order to achieve satisfactory optical performance. By restricting $\Delta T_z$ to 0.025 $^o$ C and $\Delta T_{xy}$ to 0.4 $^o$ C, the initial *rms* figure errors ranging from about 0.5 to 2.1 $\mu m$ could be reduced to within 29 *nm*, using 121 evenly distributed strips (Table 4.9). The optimum voltages applied to 121 evenly distributed strips in this case range from -290 V to 238 V (-1.16 MV/m to 0.95 MV/m).

The finite element mesh for Model-2 consists of 864 flat shell elements and 61 beam elements. The mirror is mounted on 61 force actuators (Fig. 4.6) which are used to support the mirror as well as to control the surface deformations of the mirror. The actuators are placed with an equal inter-actuator distance of 0.125 *m*. One end of the actuators or beam elements is constrained in all 6 degrees of freedom and the other end is attached to the mirror. The Young's modulus of the actuators is assumed to be 1/100 of that of the mirror. The uncorrected and corrected *rms* and maximum absolute values of the transverse deformations of Model-2, in $\mu m$, due to different temperature distributions for $\Delta T_z$=0.2 $^o$ C and $\Delta T_{xy}$=0.5 $^o$ C are given in Table 4.10. The optimum actuator forces applied to actuators in this case varied from -34 N to 20.4 N. The uncorrected and corrected *rms* values for $\Delta T_z$=0.025 $^o$ C and $\Delta T_{xy}$=0.4$^o$ C, are given in Table 4.11. The optimum actuator forces applied to actuators in this case varied from -6.4 N to 9 N.

Since the actuators are used for both support and control, changing the location of the actuators will result in different support configurations and hence different thermal deformations. In other words, the problem does not remain the same by changing the locations of the actuators. So no attempt is made to determine the optimal locations.

The thermal deformations in the case of Model-2 are smaller than those of Model-1 due to the obvious reason that the mirror is more constrained in Model-2 than in Model-1. Except for T1, the corrected *rms* figure errors obtained using 61 force actuators are quite close to those obtained using 121 piezoelectric actuators for $\Delta T_z$=0.2$^o$ C and $\Delta T_{xy}$=0.5$^o$ C. The thermal deformation due to the temperature distribution T1 resembles that of defocus, which can be corrected using a focal plane correction system (Masaki [99]) without using force actuators or piezoelectric strips. When $\Delta T_z$ is reduced to 0.025 $^o$ C and $\Delta T_{xy}$ to 0.4 $^o$ C, the percentage reduction in the *rms* error obtained using 61 force actuators is quite close to that obtained using 121 piezoelectric strips, for all four temperature distributions. The corrected *rms* in the case of the force actuators (Table 4.11) is much lower as the uncorrected *rms* is also much lower than those in the case of the piezoelectric strips.

## 4.5 Summary

Both the force actuators and the piezoelectric strips were equally effective in controlling the surface deformations of the mirror. The performance of 121 evenly distributed strips was quite comparable to that of 121 optimally placed strips. Mounting the mirror on a large number of force actuators (Model-2) appeared to be more advantageous than supporting the mirror on six kinematic supports (Model-1) at the vertices, since the mirror deformations in the former case were much lower than those in the latter, but a disadvantage of using the force actuators is the increase in the overall weight of the structure, which is undesirable for space applications. Since the piezoelectric strips are lightweight, a large number of such strips can be used to control the surface distortions of the mirror without imposing a weight penalty. Piezoelectric strips can also be used to correct both developable and non-developable surfaces since they, unlike the force actuators, can be used to impart both membrane and bending strains on the mirror.

In the actual mirror, the piezoelectric strips cannot be relocated as they will be bonded to the rear surface of the mirror. Moreover, the optimal locations determined for one type of disturbance may not be optimal for other disturbances. Correcting the mirror deformations using a set of strips with predetermined locations thus seems to be more practical than trying to find the optimal locations. Controlling the mirror deformations using a large number of evenly placed piezoelectric strips seems to be a viable solution, as such a configuration can impart control to almost every part of the mirror and hence can be used to control arbitrary deformations.

Since the piezoelectric strips act over a finite area of the mirror and the force actuators only act discretely, the mirror surface corrected using the former is expected to be smoother than that corrected using the latter. The quality of the mirror surface should be assessed in order to determine if the mirror surface is smooth enough to obtain the required operational efficiency. The *rms* figure error may not be a true measure of surface smoothness. Hence alternative measures to assess the surface smoothness of the mirror have to be determined.

It may not be possible to generate in space the kind of voltages, as determined in this study, that are to be applied to the piezoelectric strips. Hence there is a need for piezoelectric materials with much higher strain constants. A parametric study can also be conducted to determine the optimum values of the stiffness and the dimensions of the mirror and the piezoelectric strips which will result in the least thermal deformations and voltages to be applied across the strips. The feasibility of using a large number of piezoelectric strips on a mirror segment should also be examined, since the use of a large number of strips could result in a very complex electronic circuitry. In summary, the piezoelectric strips appear to be promising candidates for static shape control of flexible structures in space, opening several avenues for further research in order to determine the feasibility of using a large number of such strips for practical problems.

Table 4.1: Convergence of non-dimensionalized mid-deflection of a graphite/epoxy laminate excited by a uniform electric field.

| Grid Size quarter plate | $100W(h/b)/(bd_{33}E_z)$ |
|---|---|
| 2x2 | 0.14042 |
| 4x4 | 0.13996 |
| 6x6 | 0.13962 |
| 8x8 | 0.13945 |
| 10x10 | 0.13936 |
| 12x12 | 0.13933 |
| 14x14 | 0.13927 |
| 16x16 | 0.13925 |
| 18x18 | 0.13924 |
| Jonnalagadda *et al*(1994)<br>4x4 mesh (quarter plate)<br>9-node Lagrangian elements | 0.1396 |

Table 4.2: Transverse deflection (x$10^7$) in $m$ of a piezoelectric bimorph cantilever beam under uniform electric field, at different locations.

| Location | 2 $cm$ | 4 $cm$ | 6 $cm$ | 8 $cm$ | 10 $cm$ |
|---|---|---|---|---|---|
| This study (1x20 mesh) | .1376 | .5516 | 1.2416 | 2.2076 | 3.4496 |
| Tzou and Tseng (1990) FEM | .124 | .508 | 1.16 | 2.10 | 3.30 |
| Tzou and Tseng (1990) Theory | .138 | .552 | 1.24 | 2.21 | 3.45 |

Table 4.3: Deflection in $\mu m$, at point A, of the L-frame

| | $P_x = 100N$ | $P_y = 100N$ | $P_z = 100N$ | $M_y = 100N$ |
|---|---|---|---|---|
| Present | $u_x = .291$<br>$u_y = 0$<br>$u_z = 0$ | $u_x = 0$<br>$u_y = 37.63$<br>$u_z = 0$ | $u_x = 0$<br>$u_y = 0$<br>$u_z = 33.8$ | $u_x = 0.0257$<br>$u_y = 0$<br>$u_z = -50.6$ |
| Theory | $u_x = .284$<br>$u_y = 0$<br>$u_z = 0$ | | $u_x = 0$<br>$u_y = 0$<br>$u_z = 33.8$ | |
| B33+B31 | $u_x = .284$<br>$u_y = 0$<br>$u_z = 0$ | | $u_x = 0$<br>$u_y = 0$<br>$u_z = 33.8$ | |
| STRI3+B33 | $u_x = .291$<br>$u_y = 0$<br>$u_z = 0$ | $u_x = 0$<br>$u_y = 37.59$<br>$u_z = 0$ | $u_x = 0$<br>$u_y = 0$<br>$u_z = 33.8$ | $u_x = 0.0267$<br>$u_y = 0$<br>$u_z = -50.6$ |

Table 4.4: Properties and geometry of the mirror, piezoelectric strip and force actuator.

| Property/geometry | Mirror (Beryllium) | Piezoelectric strip | Force actuator |
|---|---|---|---|
| Young's modulus | 293 $GPa$ | 63 $GPa$ | 2.93 $GPa$ |
| Poisson's Ratio | 0.1 | 0.3 | 0.1 |
| Coefficient of thermal expansion | 11.5E-6/$^0C$ | 0.9E-6/$^0C$ | |
| Thickness | 0.012 $m$ | 0.25E-3 $m$ | |
| Radius of curvature | 10 $m$ | | |
| Side of the Hexagonal Base | 0.5 $m$ | | |
| $d_{31}$, $d_{32}$ | | 254E-12 m/V | |
| Diameter | | | 0.008 $m$ |
| Length | | | 0.05 $m$ |

Table 4.5: Temperature distribution at the lower surface of the mirror.

| | |
|---|---|
| T1 | $C[2(x^2+y^2)-1]$ |
| T2 | $C[(x+y)(3x^2+3y^2-2)]$ |
| T3 | $C[\sum_{i=1}^{i=9} K_i Z_i]$ |
| | $K_i' s$ from Table 2 (back surface) of Ref. 21 |
| T4 | $C[x+y+2xy]$ |

Table 4.6: Uncorrected *rms* and maximum absolute values of the transverse deformations of Model-1, in $\mu m$, due to different temperature distributions ($\Delta T_z = 0.2^o C, \Delta T_{xy} = 0.5^o C$).

| T(x,y) | without strips | | with 30 strips | | with 121 strips | |
|---|---|---|---|---|---|---|
| | *rms* | abs. | *rms* | abs. | *rms* | abs. |
| T1 | 4.85 | 9.65 | 5.01 | 9.89 | 5.00 | 9.88 |
| T2 | 3.00 | 5.27 | 3.14 | 5.49 | 3.11 | 5.47 |
| T3 | 1.89 | 4.91 | 1.89 | 4.87 | 1.87 | 4.81 |
| T4 | 3.28 | 5.68 | 3.39 | 5.89 | 3.37 | 5.86 |

Table 4.7: Corrected *rms* and maximum absolute residual values of the transverse deformations of Model-1, in $\mu m$, due to different temperature distributions, using 30 piezoelectric strips ($\Delta T_z = 0.2^o C, \Delta T_{xy} = 0.5^o C$).

| T(x,y) | 30 radially placed strips | | 30 optimally placed strips | |
|---|---|---|---|---|
| | *rms* | abs. | *rms* | abs. |
| T1 | 0.556 (11.5 %) | 1.868 (19.3 %) | 0.201 ( 4.1 %) | 0.686 (7.1 %) |
| T2 | 0.749 (24.9 %) | 2.698 (51.2 %) | 0.220 ( 7.3 %) | 0.884 (16.8 %) |
| T3 | 0.795 (42.0 %) | 3.822 (77.8 %) | 0.199 (10.5 %) | 0.883 (17.9 %) |
| T4 | 0.924 (28.1 %) | 3.578 (62.9 %) | 0.217 ( 6.6 %) | 0.840 (14.9 %) |

Table 4.8: Corrected *rms* and maximum absolute residual values of the transverse deformations of of Model-1, in $\mu m$, due to different temperature distributions, using 121 piezoelectric strips ($\Delta T_z = 0.2^o C, \Delta T_{xy} = 0.5^o C$).

| T(x,y) | 121 evenly distributed strips | | 121 optimally placed strips | |
|---|---|---|---|---|
| | *rms* | abs. | *rms* | abs. |
| T1 | 0.081 (1.7 %) | 0.256 (2.7 %) | 0.058 (1.2 %) | 0.197 (2.0 %) |
| T2 | 0.093 (3.1 %) | 0.255 (4.9 %) | 0.075 (2.5 %) | 0.248 (4.7 %) |
| T3 | 0.088 (4.6 %) | 0.307 (6.3 %) | 0.070 (3.7 %) | 0.246 (5.0 %) |
| T4 | 0.098 (3.0 %) | 0.309 (5.4 %) | 0.079 (2.4 %) | 0.223 (3.9 %) |

Table 4.9: Uncorrected and corrected *rms* values of the transverse deformations of Model-1, in $\mu m$, due to different temperature distributions, using 121 evenly distributed strips for $\Delta T_z$=0.025$^o$ C and $\Delta T_{xy}$=0.4$^o$ C.

| T(x,y) | Uncorrected *rms* | Corrected *rms* |
|---|---|---|
| T1 | 1.971 | 0.0239 (1.2 %) |
| T2 | 0.536 | 0.0147 (2.7 %) |
| T3 | 2.125 | 0.0278 (1.3 %) |
| T4 | 1.195 | 0.0285 (2.4 %) |

Table 4.10: Uncorrected and corrected $rms$ and maximum absolute values of the transverse deformations of Model-2, in $\mu m$, due to different temperature distributions, using 61 force actuators ($\Delta T_z = 0.2^o C, \Delta T_{xy} = 0.5^o C$).

| T(x,y) | Uncorrected | | Corrected | |
|---|---|---|---|---|
| | $rms$ | abs. | $rms$ | abs. |
| T1 | 0.5228 | 1.1997 | 0.0444 (8.5 %) | 0.0954 (7.9 %) |
| T2 | 0.9456 | 2.4391 | 0.0414 (4.4 %) | 0.0946 (3.8 %) |
| T3 | 1.1800 | 2.8037 | 0.0407 (3.4 %) | 0.0942 (3.4 %) |
| T4 | 0.9212 | 2.1236 | 0.0413 (4.5 %) | 0.0915 (4.3 %) |

Table 4.11: Uncorrected and corrected $rms$ values of the transverse deformations of Model-2, in $\mu m$, due to different temperature distributions, using 61 force actuators ($\Delta T_z = 0.025^o C, \Delta T_{xy} = 0.4^o C$).

| T(x,y) | Uncorrected $rms$ | Corrected $rms$ |
|---|---|---|
| T1 | 0.5119 | 0.0078 (1.5 %) |
| T2 | 0.2062 | 0.0054 (2.6 %) |
| T3 | 0.3802 | 0.0050 (1.3 %) |
| T4 | 0.1153 | 0.0052 (4.5 %) |

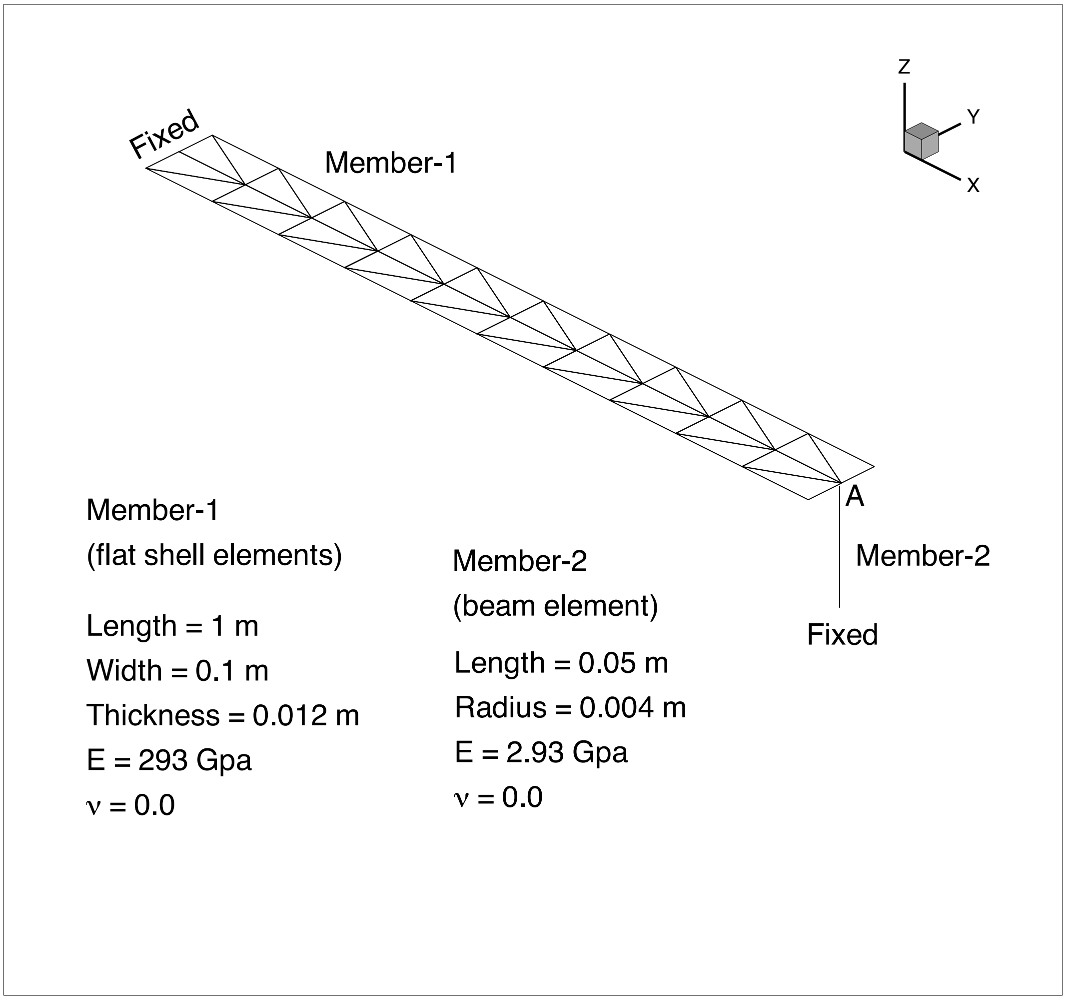

Figure 4.1: Geometry and material properties of the L-frame

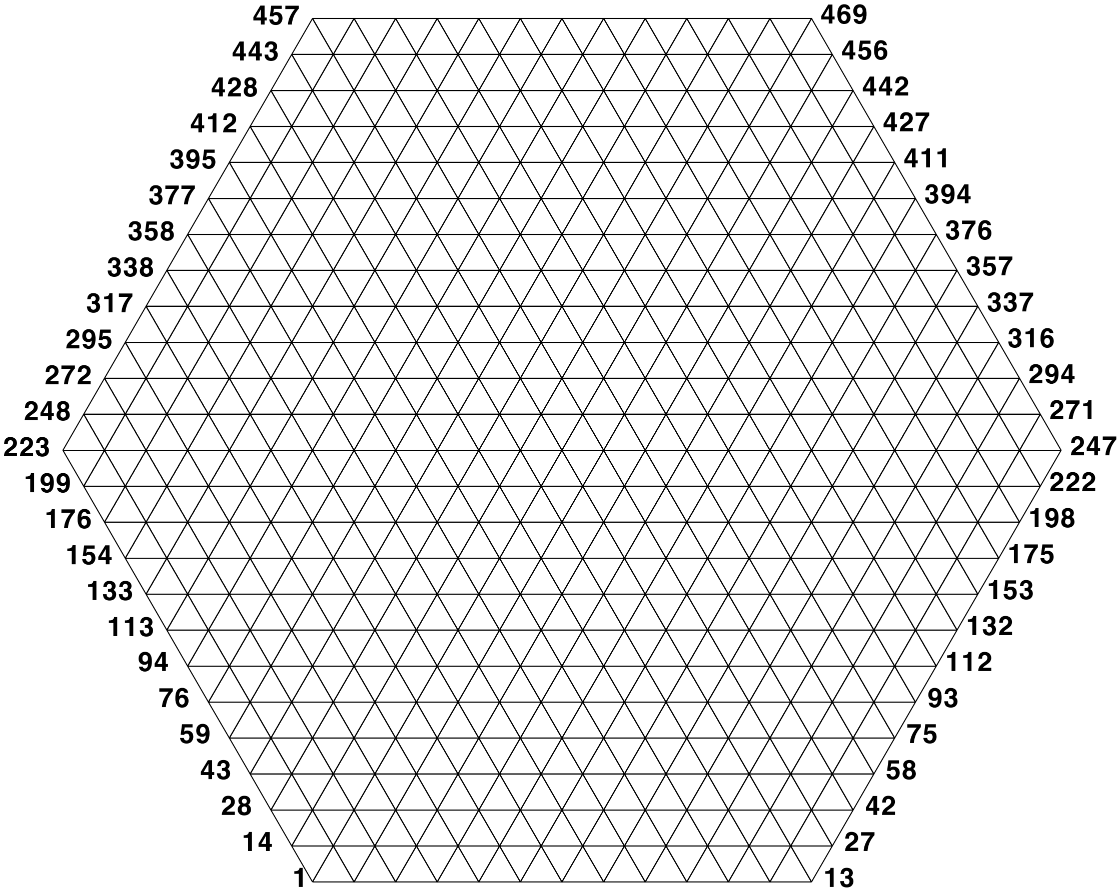

Figure 4.2: Finite element mesh for Model-1.

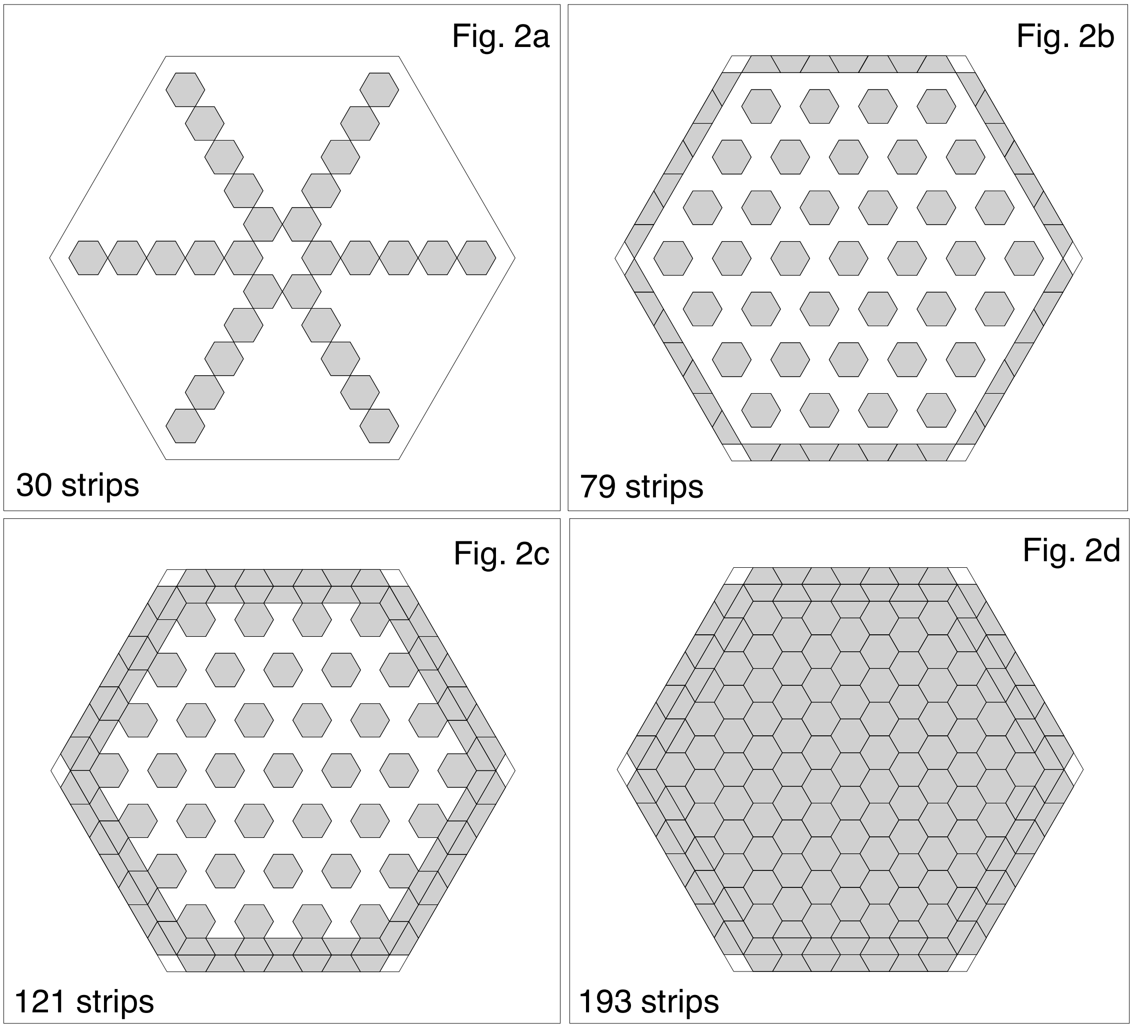

Figure 4.3: Piezoelectric strip configurations.

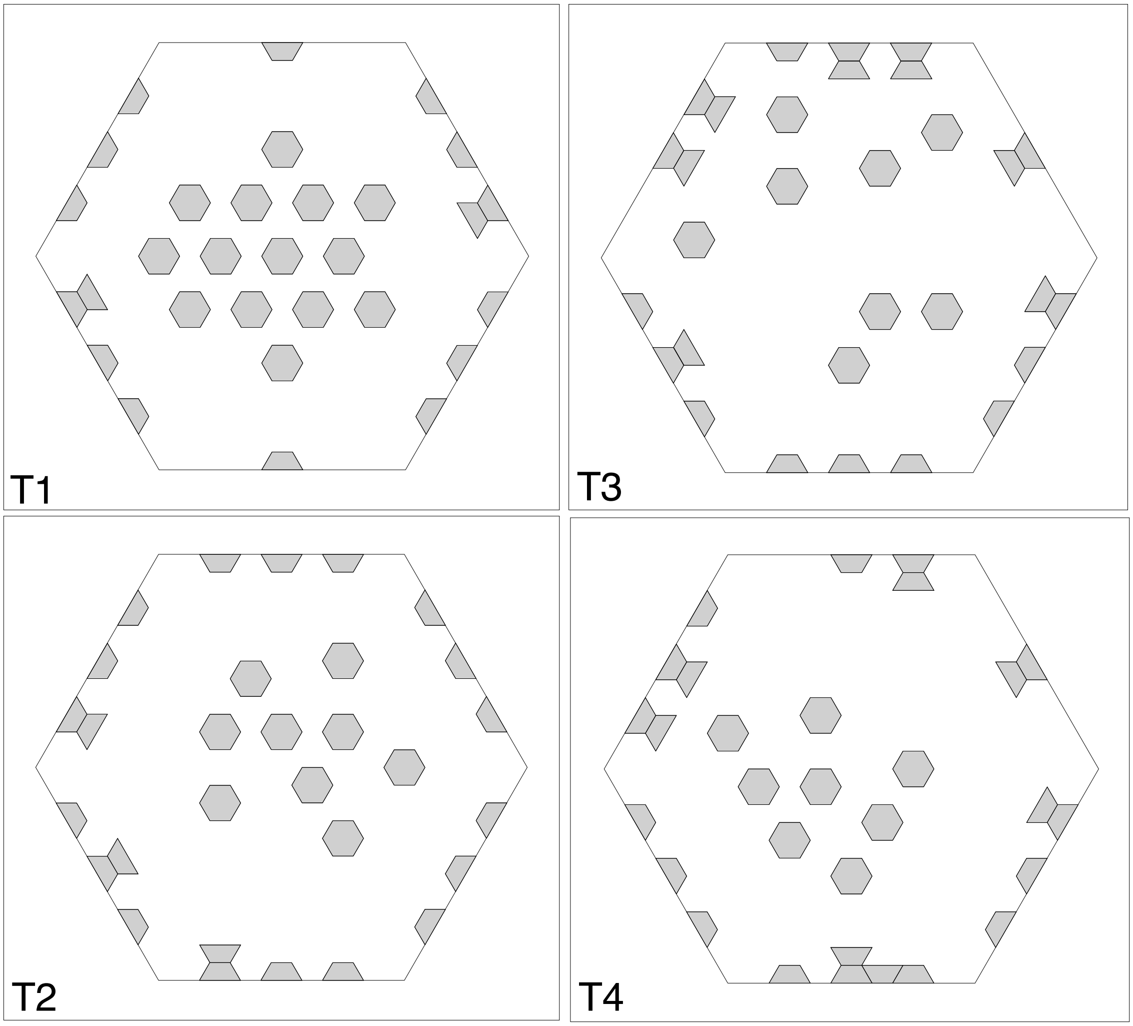

Figure 4.4: Optimal locations of 30 strips.

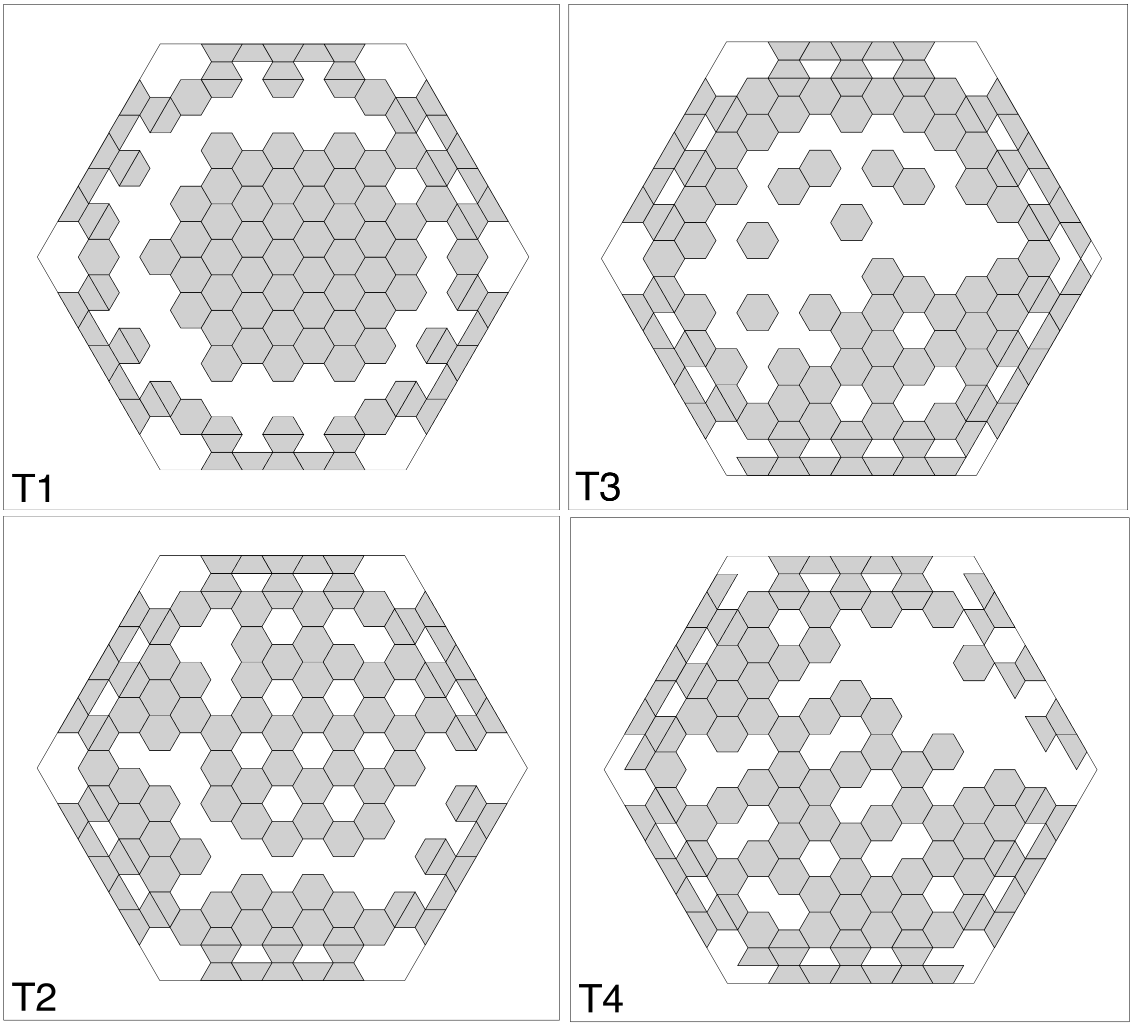

Figure 4.5: Optimal locations of 121 strips.

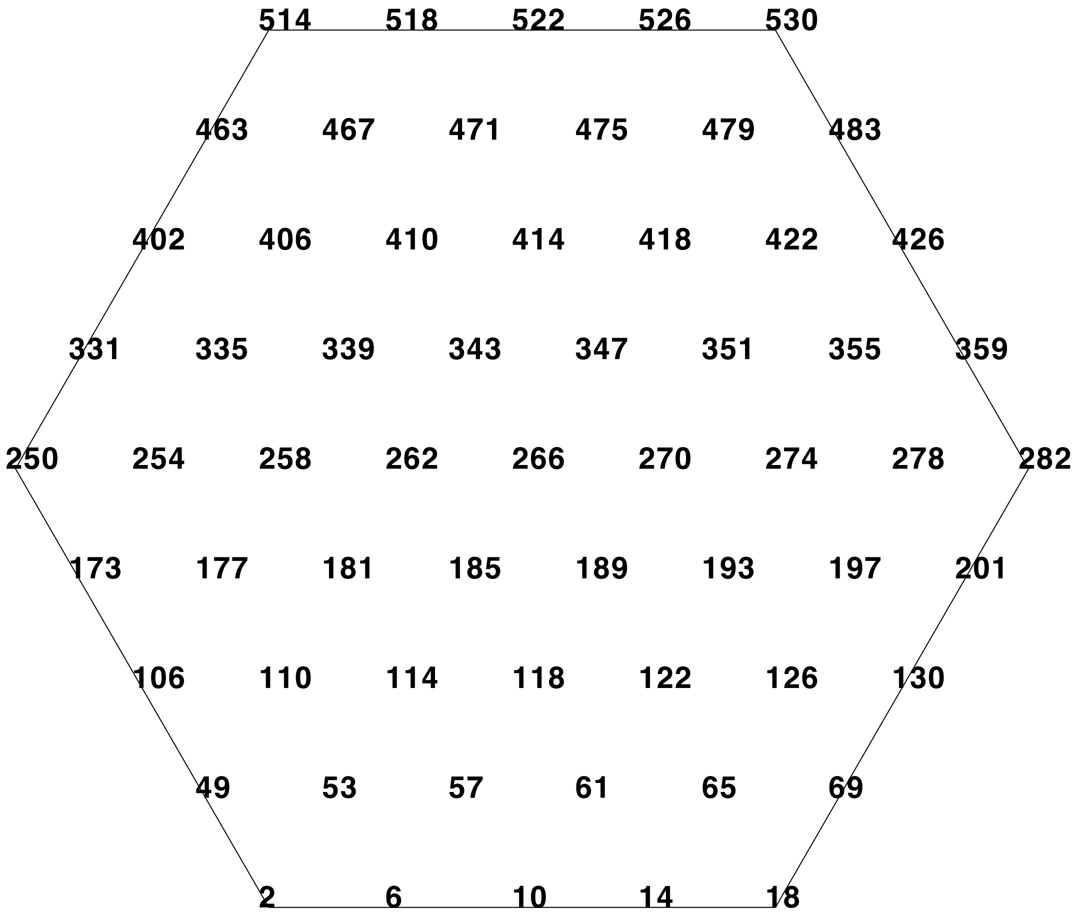

Figure 4.6: Locations of 61 force actuators.

# Chapter 5

# Analysis of Inflatable Structures

The second application for which the flat shell element described in Chapter 2 is intended to be used is the analysis of a large inflatable structure as shown in Fig. 1.1. Such a structure is being considered by the US Army to be used as a transportable tent to house vehicles and personnel. The updated Lagrangian formulation of the flat shell element described in Chapter 2 has been primarily developed to analyze large inflatable structures, as such structures are expected to undergo large deformations under the action of environmental loads like wind and snow loads. The tent structure is made up of arches which are stiffened by inflation, and membranes which are connected to the arches and held under tension. Before attempting to analyze the tent structure, a single arch under mechanical and pressure loads was analyzed, in order to verify the accuracy of the present flat shell formulation in predicting the nonlinear response of such large flexible structures. The results of this analysis are presented below.

## 5.1 Analysis of a Thin Circular Arch

*Thin circular arch under a concentrated apex load:* The geometry and the material properties used are given in Fig. 5.1. One quadrant of the arch under a concentrated apex load was analyzed. In Fig. 5.1, the results of the convergence study, performed using the present element, are presented. As can be seen from Fig. 5.1, the present results are pretty much converged for mesh sizes 25x80 and beyond. The results obtained using the present element, STRI3, S4R5 and S4R, using a 25x100 mesh, are presented in Fig. 5.2. As can be seen from Fig. 5.2, both STRI3 and S4R5 fail to give a stable solution, even using a fine mesh (25x100). The present element or S4R did not show such behavior and the agreement between the two is quite comparable. As can be seen from Fig. 5.2, the arch undergoes large deformation only in the region around the apex. Hence a finer grid could have been used only around the apex. Such grid stretching was not done, as the main aim of the analysis was to assess the accuracy of the formulation.

*Thin circular arch under nonuniform pressure:* The geometry and the material properties used are given in Fig. 5.3. Two types of pressure distributions were considered, one symmetric (Fig. 5.3) and another unsymmetric (Fig. 5.5). The same geometry and material properties were used for both types of pressure distributions. The pressure load is assumed to be space attached, or in other words the magnitude of the pressure distribution along the length of the arch is treated as a function of the current/deformed configuration of the arch. The magnitude around any cross section is assumed to be uniform. The analysis was performed with the pressure stiffness matrix included in the system tangent stiffness matrix, since it is clear from the example of the cantilever beam presented in Chapter 3 that the rate of convergence of the solution is greatly enhanced if the pressure stiffness matrix is included. In Fig. 5.3, the results of the convergence study for the symmetric pressure distribution are shown. The convergence is quite rapid, unlike the case of the concentrated load. The present results obtained using a fairly coarse mesh (20x40) appear to be a reasonably good estimate of the converged solution, even in the regime of large rotations. The present results, obtained using the arc-length control method, are compared with those obtained using the S4R and STRI3 elements using the same solution procedure and convergence criterion, in Figs. 5.4 and 5.5 for the two types of pressure distributions.

In the case of the symmetric pressure distribution, the analysis was performed until the two diametrically opposite points of the cross section at the apex met each other. In the case of the unsymmetric pressure distribution, the analysis was terminated at point B (Fig. 5.5) since the convergence was too slow even in the case of the curved shell element (S4R) probably due to severe nonlinearities and large deformations.

As can be seen from Figs. 5.4 and 5.5, the present results are in good agreement with those of S4R. The results obtained using STRI3 do not agree well with the present results and those obtained using S4R, especially in the case of the unsymmetric pressure distribution (Fig. 5.3). Poor performance of the STRI3 element can also be noticed in the case of the thin circular arch under concentrated apex load (Fig. 5.1) and in the case of nonlinear response of some shell problems presented in Chapter 3. The present flat shell formulation, which is based on the assumption that the incremental rotations are moderate, seems more reliable and requires fewer load steps compared to STRI3 which is based on a large rotation theory similar to that proposed by Simo and Fox [53]. It is not clear why a large number of load steps are required in the case of STRI3 in spite of the fact that the formulation is based on the large rotation theory. The reason for the better performance of the present flat shell element could be attributed to the use of a better membrane representation than that used in the case of STRI3.

After having validated the present flat shell element for a wide variety of problems and gaining sufficient confidence in using the element to obtain the nonlinear response of large flexible structures, the element is currently being used for the nonlinear analysis of the tent structure, under wind and snow loads. The wind load is being modeled as a non-uniform pressure load and the snow load as lumped concentrated loads. Preliminary results of the analysis of the tent structure are presented below.

## 5.2 Analysis of a Tent Structure

A symmetric model of the tent structure which represents a repeated combination of arches and membranes was first analyzed in order to gain insight into the behavior of the structure under the action of wind and snow loads. The material properties used are the same as those used in the previous examples involving a single arch.

Shown in Fig. 5.6 are the results of the analysis of the tent structure under a wind load, with a distribution as shown. One half of the arch and the membrane with symmertric boundary conditions was analysed using a 20x20x120 mesh, with 20 divisions along one half of the cross section of the arch (AF in Fig. 5.6), 20 along the width of the membrane (AB in Fig. 5.6) and 120 divisions along the length of the arch/membrane (AD or BC in Fig. 5.6). The point of attachment of the membrane to the arch is shown in Fig. 5.6. The arch was first inflated to 100 *psi* and then the wind load was applied. The wind load was applied to the entire membrane and portion of the arch not covered by the membrane (AG in Fig. 5.6). The wind load was modeled as a nonuniform external pressure, with the direction normal to the deformed congifuration. As expected, the tent undergoes large deformations near the area where the wind load is like external pressure and also sways to the right due to the suction on the rest of the tent.

Shown in Fig. 5.7 are the results of the analysis of the tent structure under a snow load. A quarter model of the tent was analyzed using a 20x18x60 mesh. The geometry and the material properties used are the same as those used in the case of the wind load. The snow load was assumed to act over a sector $22.5^o$ on either side from the apex, on the area projected onto the XY-plane. As in the case of the wind load, the arch was inflated to 100 *psi* before applying the snow load. The apex deflection due to the initial inflation in the case of the half and quarter tent models are slightly different, probably due to the symmetry conditions along CDE in Fig. 5.7, which were not enforced in the half tent model (Fig. 5.6).

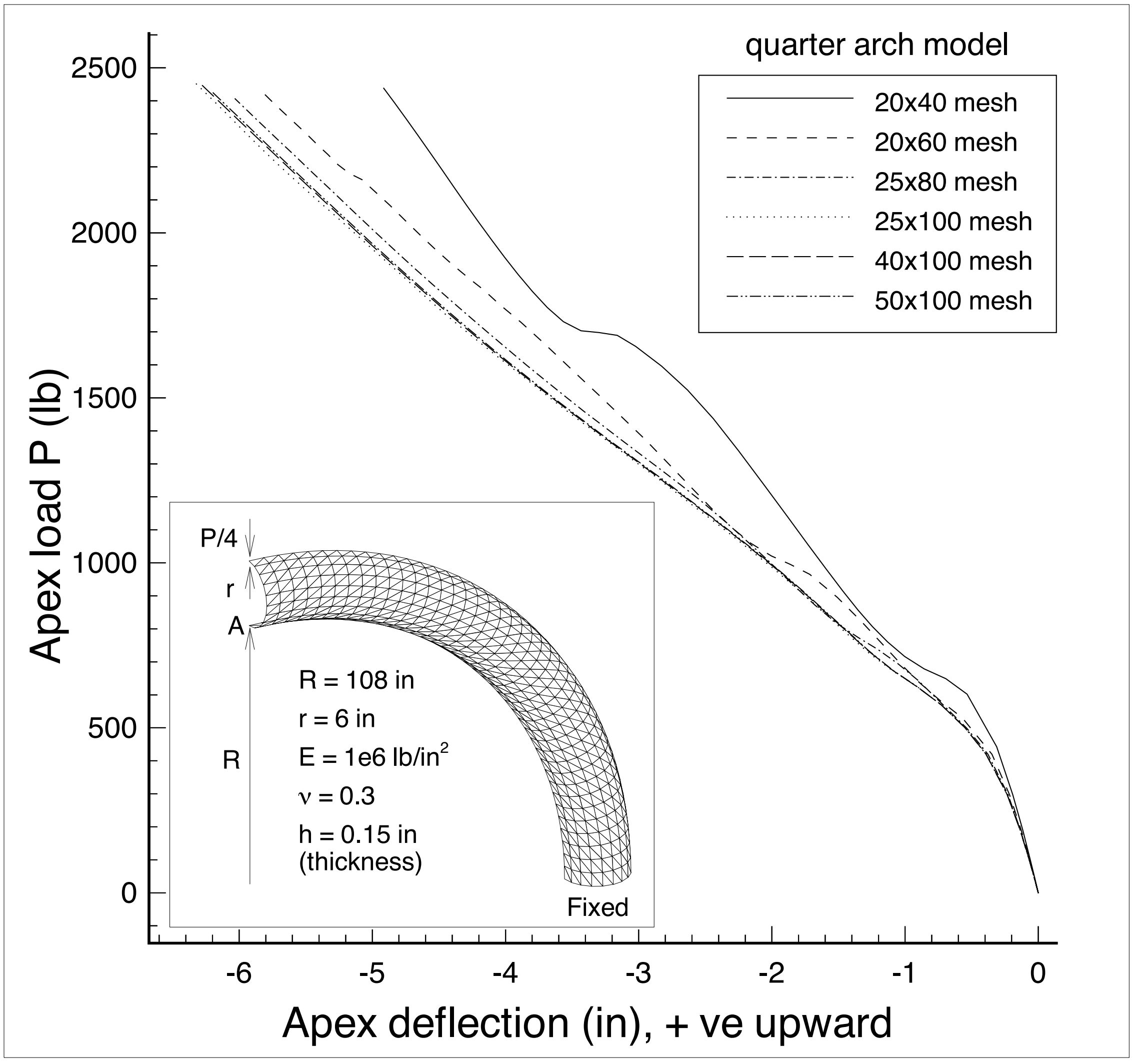

Figure 5.1: Convergence of the deflection at point A, of a thin circular arch under a concentrated apex load P

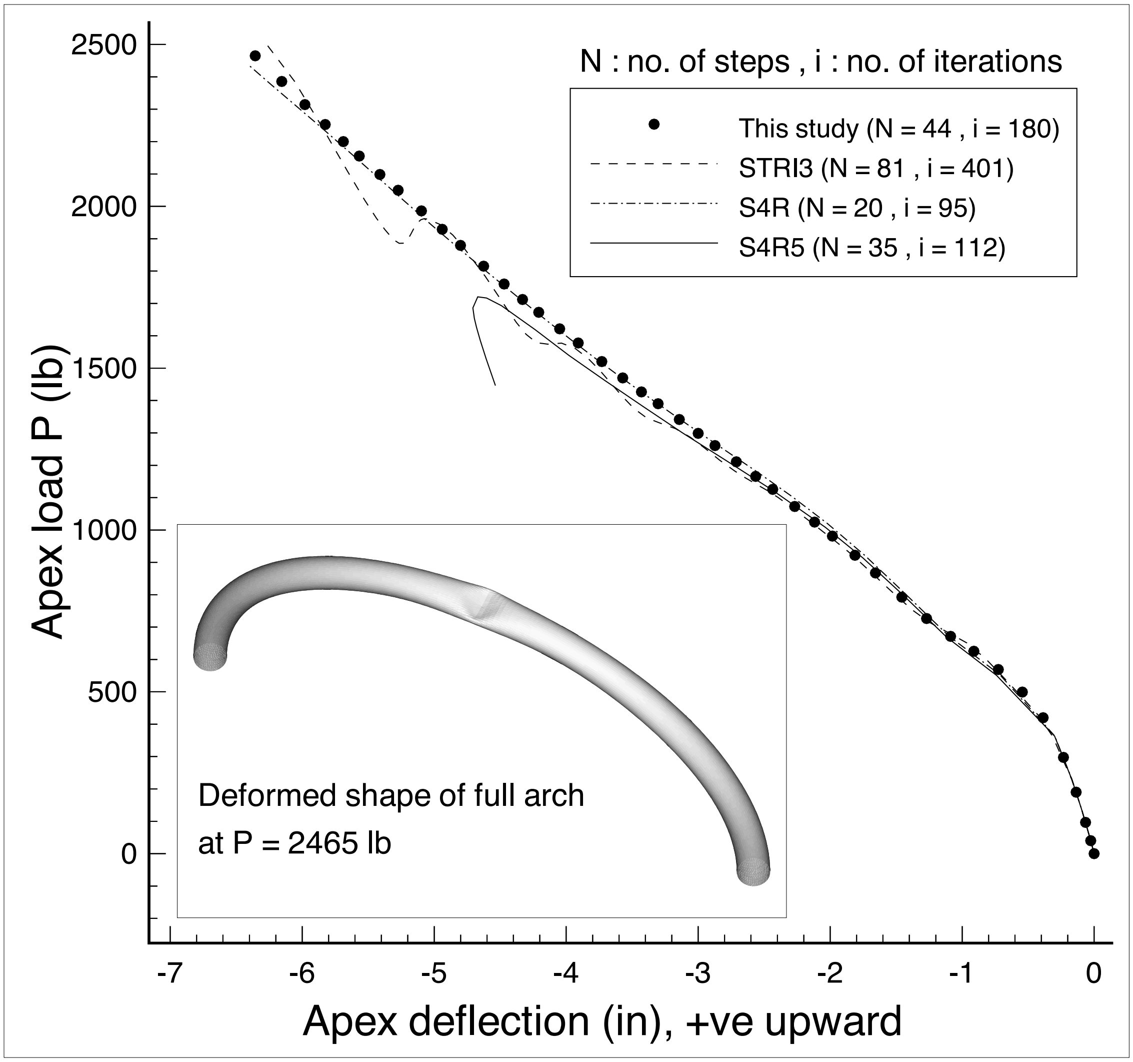

Figure 5.2: Deflection at point A, of a thin circular arch under concentrated apex load P

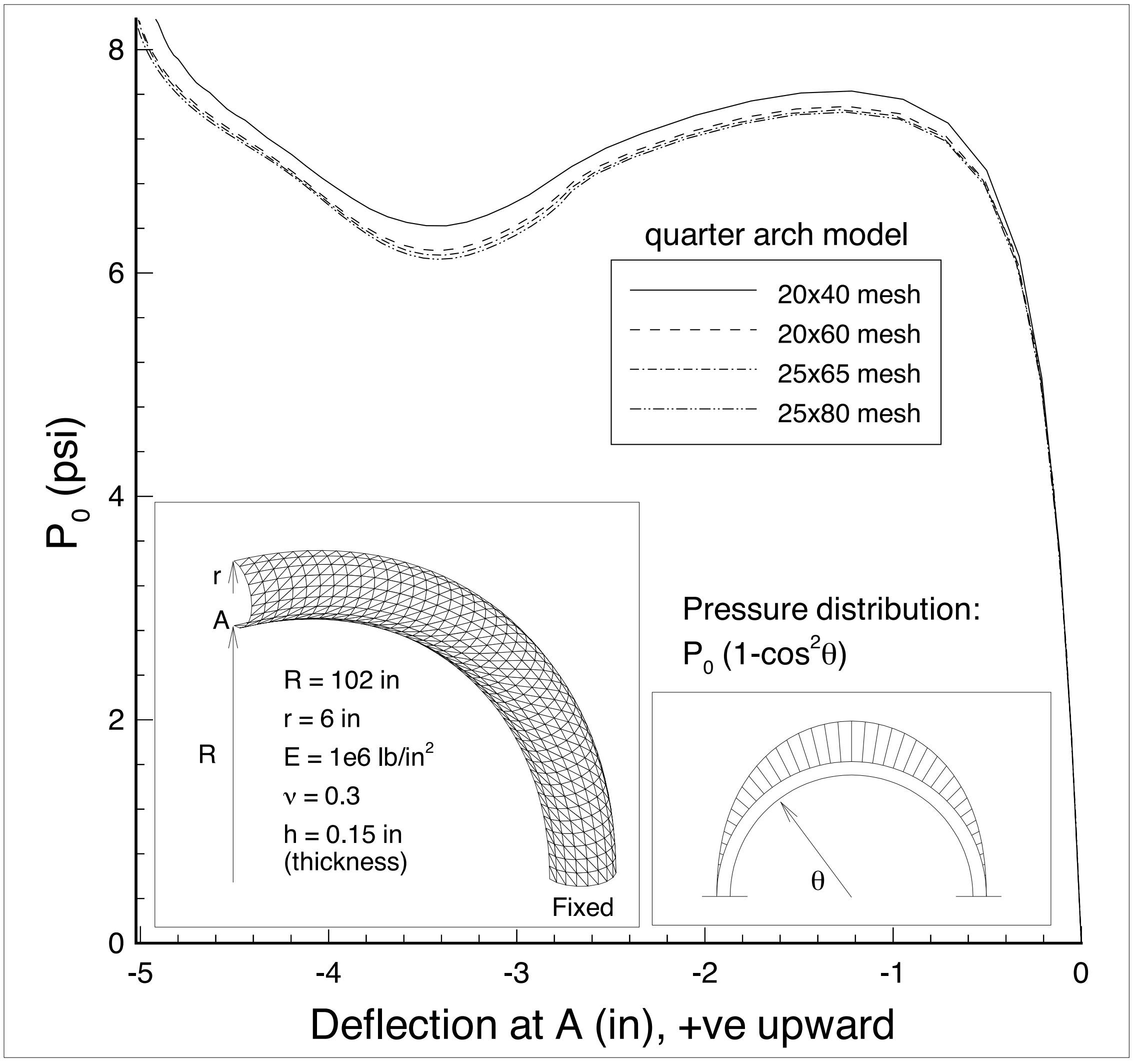

Figure 5.3: Convergence of the deflection at point A, of a thin circular arch under a symmetric nonuniform external pressure

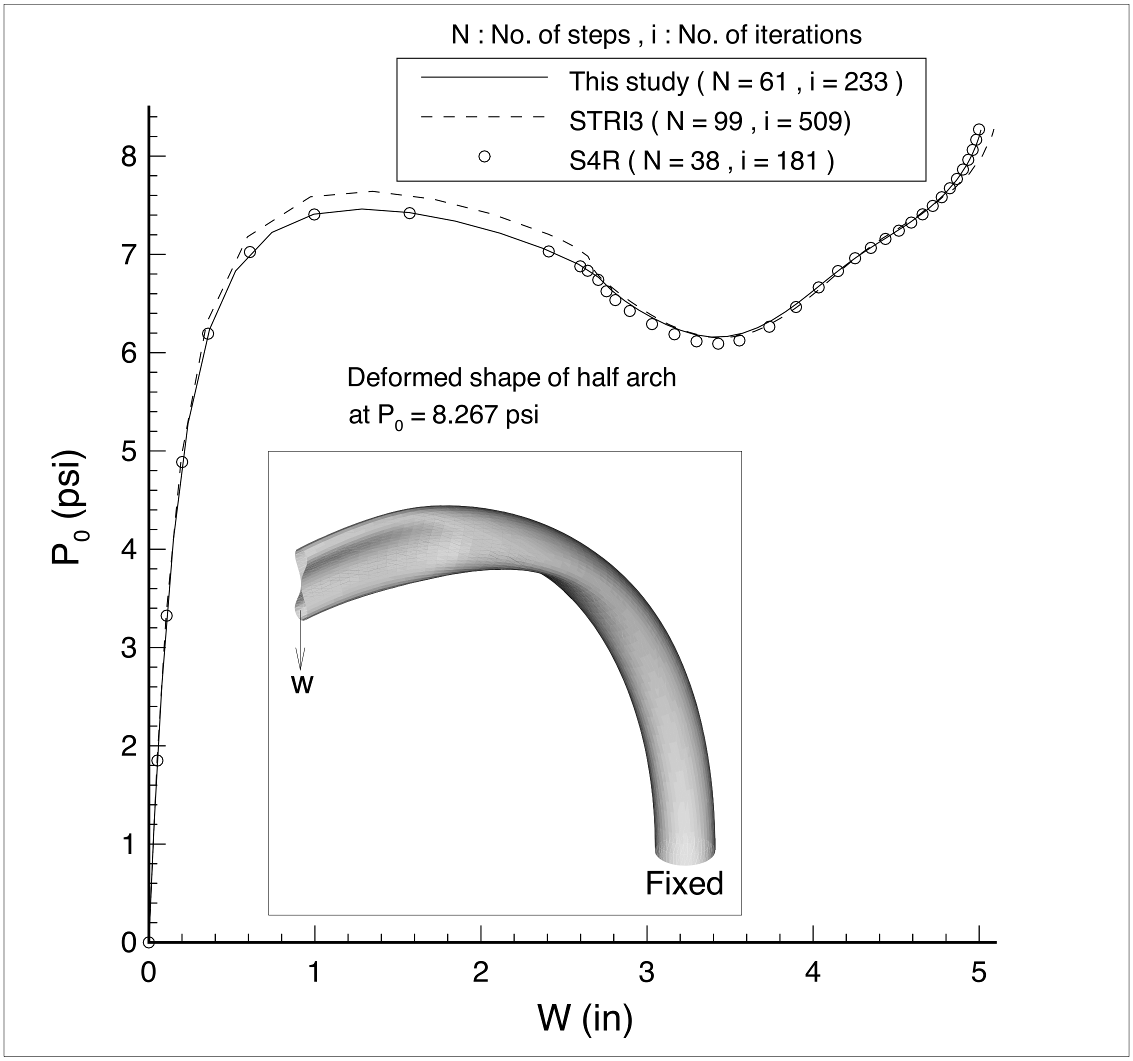

Figure 5.4: Deflection at point A, of a thin circular arch under symmetric non-uniform external pressure (quarter arch model, 25x65 mesh, 3250 elements, 10296 d.o.f.)

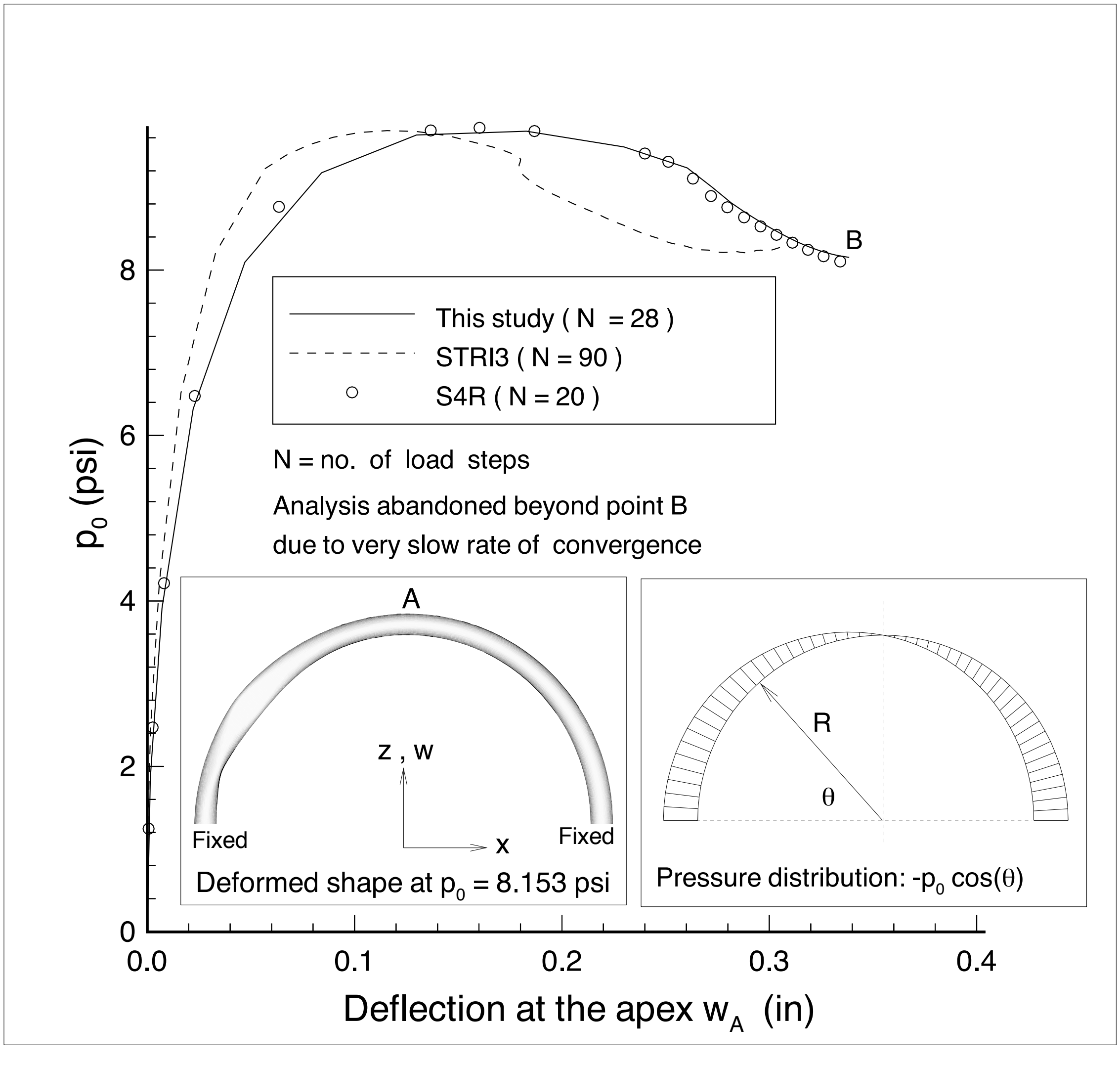

Figure 5.5: Deflection at point A, of a thin circular arch under unsymmetric nonuniform pressure (half arch model, 25x150 mesh, 7500 elements, 23556 dof)

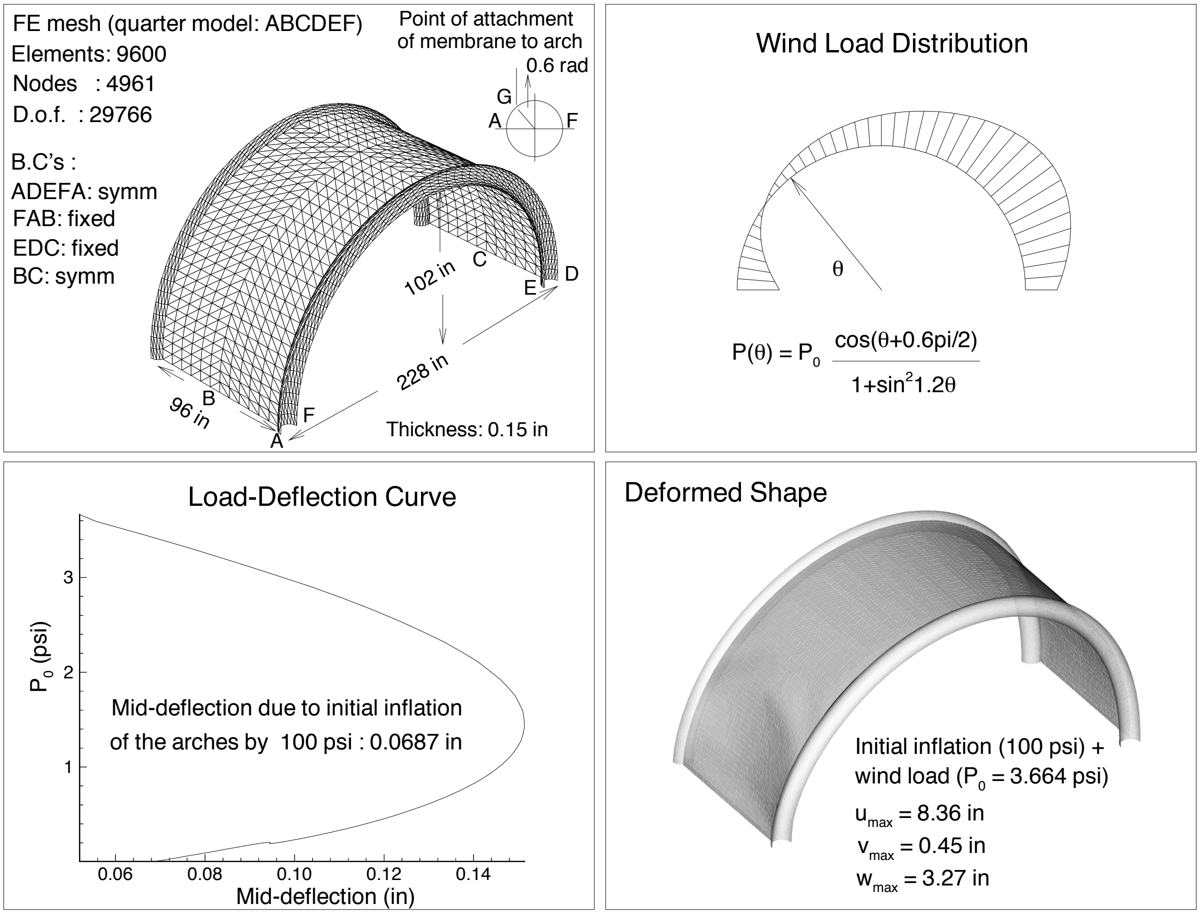

Figure 5.6: Analysis of a tent structure under a wind load

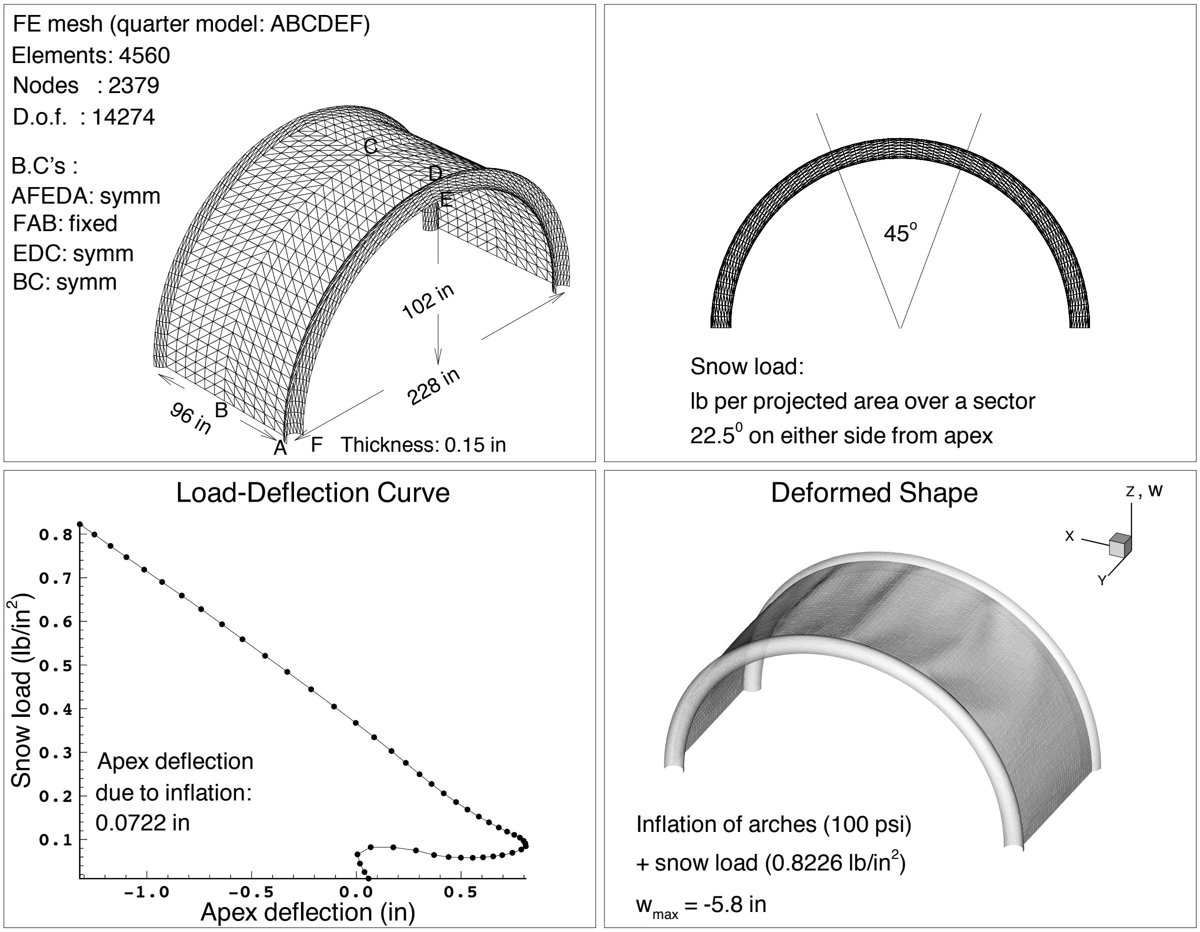

Figure 5.7: Analysis of a tent structure under a snow load

# Conclusions

Finite element analysis of general shells using a three-noded flat triangular shell element was presented. The flat shell element is a combination of the Discrete Kirchhoff Theory (DKT) plate bending element and a membrane element similar to the Allman element, but derived from the Linear Strain Triangular (LST) element. The DKT element has three degrees of freedom per node, a transverse displacement and two out-of-plane rotations. The Allman element also has three degrees of freedom per node, two in-plane displacements and an in-plane rotation. Though this combination has been employed in the literature for linear static analysis of laminated plates, the results presented are not adequate to ascertain that the element would perform well in the case of static and dynamic analysis of general shells. In the present research, the element was first thoroughly tested for linear static analysis of laminated plates and shells and , after having validated its accuracy, the element has been extended for free vibration, thermal, and geometrically nonlinear analysis.

The major drawback of the DKT plate bending element is that the transverse displacement is not explicitly defined within the interior of the element. Hence obtaining the consistent mass matrix or the derivatives of the trasnverse displacement that are required for forming the geometric stiffness matrix is not straightforward. This problem can alleviated by using a lumped mass matrix, but the analysis is expensive, especially if a large number of modes are to be extracted, due to slow rate of convergence. In the present research, free vibration analysis was performed both by using lumped and so-called consistent mass matrices, in order to compare the performace of the two methods. A fourth-order polynomial, borrowed from an existing element, was used to compute the mass terms corresponding to the transverse displacement. The same shape functions that were used to compute the stiffness matrix of the LST element were used to compute the mass terms corresponding to the in-plane displacements. The rotary inertias were also included in the consistent mass matrix, unlike the lumped mass matrix. In the case of the thermal analysis, the temperature variation was assumed to vary linearly along the thickness of the element and the variation in the plane of the element was assumed to be linear in the standard area coordinates. The geometrically nonlinear analysis was performed using an updated Lagrangian formulation employing Green strain and PK2 stress measures. A linear displacement field was used for the transverse displacement in order to compute the derivatives of the transverse displacement that are required to compute the geometric stiffness or the initial stress matrix.

Several numerical examples were solved to demonstrate the accuracy of the formulation for both small and large rotation analysis of laminated plates and shells. The results were compared with those available in the existing literature and those obtained using the STRI3, S4R5 and S4R elements of the commercial finite element package ABAQUS. The present results agreed well with those available in the existing literature, wherever applicable, for both linear and nonlinear analysis. In the case of nonlinear analysis, the agreement between the present results and S4R was better than that with STRI3 or S4R5. The STRI3 element showed poor performance and some convergence problems, and both STRI3 and S4R exhibited overly soft behavior for some nonlinear problems. The present element or S4R did not not show such behavior. The present flat shell formulation which is based on the assumption that the incremental rotations are moderate, appeared to be more reliable and required fewer load steps compared to STRI3 which is based on a large rotation theory. It is not clear why a large number of load steps are required in the case of STRI3 in spite of the fact that the formulation is based on the large rotation theory. The reason for the better performance of the present flat shell element could be attributed to the use of a better membrane representation than that used in the case of STRI3.

A large number of elements were required to obtain convergence towards the exact solution or finite element results available in the existing literature. When a flat shell element is used for the analysis of general shells, a finer mesh is mandatory in order to obtain a closer approximation to the curved structure. In the case of problems involving large rotations, more steps were required for the analysis using the present element than required by the S4R element or elements in the existing literature based on a large rotation theory. Though a finer mesh and large number of load steps are required, the analysis is not expected to be computationally expensive, due to the extreme simplicity of the formulation. A comparison of the CPU time required for the analysis using the present element and those of ABAQUS (STRI3, S4R and S4R5) has not been presented. This is due to the fact that the present results were obtained using a code entirely developed by the author, whereas the code used in the commercial software ABAQUS must have been well tuned for optimal performance. However, comparing the number of load steps required by the present element and STRI3, it can be concluded that the analysis using the present flat shell element would certainly be faster than that using the STRI3 element, provided a similar computational environment is used for both. The computational time can be drastically reduced by taking proper care in developing the code like avoiding redundant computations, using data stored in contiguous memory locations, using an efficient solver, etc. The computational time can be further reduced by using a parallel code. The entire process of generation of element stiffness matrices, assembly of the global stiffness matrix and the solution of the system of equations can be performed in parallell on several processors, thereby reducing the overall time required for the computation.

The present formulation does not suffer from in-plane rotational singularity, spurious zero energy modes or shear locking and hence the formulation is less complicated compared to the flat shell formulations which suffer these problems, since additional efforts are required to alleviate such problems, often making the formulation complex. The simplicity and reliability of the present formulation, combined with the availability of high speed parallel computers, renders it a promising candidate for economic and yet accurate analysis of large flexible thin structures. The present element was employed for two main applications involving large flexible structures.

The first application is the control of thermal deformations of a spherical mirror segment. The feasibility of controlling the surface distortions of the mirror due to arbitrary thermal fields, using discrete and distributed actuators, was studied. This kind of study was required for the design of a multi-segmented primary mirror of a next generation space telescope. To determine the effectiveness of the actuators in controlling the thermal deformations of the mirror segment, a comparative study was conducted using 2 different models of the mirror-actuator system: (1) the mirror mounted on kinematic supports and controlled by piezoelectric strips bonded to the rear surface of the mirror and (2) the mirror mounted on force actuators which are used to support the mirror as well as to control the surface deformations of the mirror. The mirror was modeled using the flat shell elements, the piezoelectric strips were also modeled using the flat shell elements, but as a separate layer of isotropic material and the force actuator was modeled using a beam element. Performance of evenly distributed strips with that of strips placed at near optimal locations obtained using heuristic integer programming was also compared. Since the force actuators are used for both support and control, the problem does not remain the same by changing the locations of the actuators. So no attempt was made to determine the optimal locations of the force actuators. Results were presented for surface distortions of the mirror segment due to various temperature distributions given in the form of linear combinations of the first few Zernike polynomials. Both the force actuators and the piezoelectric strips were found to be equally effective in controlling the surface deformations of the mirror. The performance of a set of evenly placed piezoelectric strips was found to be quite compatable to that of strips placed at near-optimal locations.

A major drawback of the force actuators is the increase in the overall weight of the system, which is undesirable for space applications. On the other hand, the piezoelectric strips are very lightweight and hence a large number of such strips can be used to control the surface distortions of the mirror, without imposing a weight penalty. In the actual mirror, the piezoelectric strips cannot be relocated as they will be bonded to the rear surface of the mirror. Moreover, the optimal locations determined for one type of disturbance may not be optimal for other disturbances. Correcting the mirror deformations using a set of strips with predetermined locations thus seems to be more practical than trying to find the optimal locations. Controlling the mirror deformations using a large number of evenly placed piezoelectric strips seems to be a viable solution as such a configuration can impart control to almost every part of the mirror and hence can be used to control arbitrary deformations. In summary, the piezoelectric strips appear to be promising candidates for static shape control of flexible structures in space, opening several avenues for further research in order to determine the feasibility of using a large number of such strips for practical problems.

The second application for which the flat shell element was intended to be used is the analysis of an inflatable structure. Such a structure is being considered by the US Army to be used as a transportable tent to house Army vehicles and personnel. The tent structure is made up of membranes suported by arches stiffened by internal pressure. The updated Lagrangian formulation of the flat shell element has been developed primarily for the nonlinear analysis of the tent structure since such a structure is expected to undergo large deformations and rotations under the action of environmental loads like the wind/pressure and snow loads. Since the direction of the pressure load is assumed to be normal to the current configuration of the structure, its direction changes as the structure undergoes deformation. This is called the follower action. As a result of the follower action, the pressure load is a function of the displacements and contributes to the tangent stiffness matrix in the case of geometrically nonlinear analysis. The thermal load also contributes to the system tengent stiffness matrix. In the case of the thermal load, this contribution is similar to the initial stress matrix and hence no additional effort is required to compute this contribution. In the case of the pressure load, this contribution called the pressure stiffness is in general unsymmetric and its determination is not straightforward. In the present research, the deformation dependent pressure load and the pressure stiffness matrix were systematically derived using the principle of virtual work. The contribution of the rotational degrees of freedom was neglected in determining the pressure load and the pressure stiffness matrix. Since most of the deformation of the element is comprised of rigid body motions, a linear displacement field was used to compute the pressure load and the pressure stiffness matrix. The updated Lagrangian formulation of the flat shell element, including the follower effects as mentioned above was validated using standard examples in the existing literature on deformation dependent pressure loads. Before attempting to analyze the tent structure using the present element, analysis of a single circular arch under nonuniform pressure loads was performed. The results were compared with those obtained using the STRI3 and S4R elements of ABAQUS. The present results showed excellent agreement with those of S4R, whereas the STRI3 did not agree well with the present results or those obtained using S4R.

After having thoroughly validated the present flat shell formulation for a wide variety of problems and gaining confidence in using the element to obtain the nonlinear response of large thin flexible structures, the element is currently being used for nonlinear analysis of the tent structure under wind and snow loads. The wind load is being modeled as a non-uniform pressure load and the snow load as lumped concentrated loads.

# Bibliography

[1] Meek, J. L. and Tan, H. S., "A Faceted Shell Element With Loof Nodes". *International Journal for Numerical Methods in Engineering*, Vol. 23, pp. 49-67, 1986.

[2] Yang, T. Y., "*Finite Element Structural Analysis*", Prentice-Hall, 1986.

[3] Allman, D. J., "A Compatible Triangular Element Including Vertex Rotations For Plane Elasticity Analysis", *Computers and Structures*, Vol. 19, pp. 1-8, 1984.

[4] Allman, D. J., "Evaluation of the Constant Strain Triangle with Drilling Rotations", *International Journal for Numerical Methods in Engineering*, Vol. 26, pp. 2645-2655, 1988.

[5] Cook, R. D., "On The Allman Triangle and Related Quadrilateral Element", *Computers and Structures*, Vol. 22, pp. 1065-1067, 1986.

[6] Bergan, P. G. and Fellipa, C. A. "A Triangular Membrane Element With Rotational Degrees of Freedom", *Computer Methods in Applied Mechanics and Engineering*, Vol. 50, pp. 24-69, 1984.

[7] Bergan, P. G. and Nygard, M. K.,"Finite Elements With Increased Freedom in Choosing Shape Functions", *International Journal for Numerical Methods in Engineering*, Vol. 20, pp. 643-664, 1985.

[8] Zienkiewicz, O. C. and Taylor, R. L., "*The Finite Element Method*", 4th edition, Vol. 1, McGraw-Hill, 1989.

[9] Bazeley, G. P., Cheung, Y. K., Irons, B. M. and Zienkiewicz, O. C., "Triangular Elements in Plate Bending, Conforming and Nonconforming Solutions", *Proc. 1st Conf.*

*on Matrix Methods in Structural Mechanics*, pp. 547-576, AFFDLTR-CC-80, Wright-Patterson AF Base, Ohio, 1966.

[10] Carpenter, N., Stolarski, H. and Belytschko, T., " A Flat Triangular Shell Element With Improved Membrane Interpolation", *Communications in Applied Numerical Methods*, Vol. 1, pp. 161-168, 1985.

[11] Fish, J. and Belytschko, T., "Stabilized Rapidly Convergent 18-Degrees of Freedom Flat Shell Triangular Element", *International Journal for Numerical Methods in Engineering*, Vol. 33, pp. 149-162, 1992.

[12] Cook, R. D., "Some Options For Plane Triangular Elements With Rotational Degrees of Freedom", *Finite Elements in Analysis and Design*, Vol. 6, pp. 245-249, 1990.

[13] Zienkiewicz, O. C., "*The Finite Element Method*", 3rd edition, McGraw-Hill, London, 1977.

[14] MacNeal, R. H. and Harder, R. L., "Refined Four-Noded Membrane Element with Rotational Degrees of Freedom", *Computers and Structures*, Vol. 28, pp. 75-84, 1988.

[15] Cook, R. D., "Modified Formulations for Nine-D.O.F. Plane Triangles That Include Vertex Rotations", *International Journal for Numerical Methods in Engineering*, Vol. 31, pp. 825-835, 1991.

[16] Batoz, J. L., Bathe, K. J. and Ho, L. W., "A Study of Three Noded Triangular Plate Bending Elements", *International Journal for Numerical Methods in Engineering*, Vol. 15, pp. 1771-1812, 1980.

[17] Cook, R. D., "A Plane Hybrid Element With Rotational DOF and Adjustable Stiffness", *International Journal for Numerical Methods in Engineering*, Vol. 24, pp. 1499-1508, 1987.

[18] Allman, D. J., "A Quadrilateral Finite Element Including Vertex Rotations for Plane Elasticity Analysis", *International Journal for Numerical Methods in Engineering*, Vol. 26, pp. 717-730, 1987.

[19] Yunus, S. M., Saigal, S. and Cook, R. D., “On Improved Hybrid Finite Element with Rotational Degrees of Freedom”, *International Journal for Numerical Methods in Engineering*, Vol. 28, pp. 785-800, 1989.

[20] Cazzani, A. and Atluri, S. N., “Four-noded Mixed Elements Using Unsymmetric Stresses for Linear Analysis of Membranes”, *Computational Mechanics*, Vol. 11, pp. 229-251, 1993.

[21] Hughes, T. R. J. and Brezzi, F., “On Drilling Degrees of Freedom”, *Computer Methods in Applied Mechanics and Engineering*, Vol. 72, pp. 105-121, 1989.

[22] Ibrahimbegovic, A., “A Novel Membrane Finite Element With an Enhanced Displacement Interpolation”, *Finite Elements in Analysis and Design*, Vol. 7, pp. 167-179, 1990.

[23] Iura, M and Atluri, S. N, “Formulation of a Membrane Finite Element With Drilling Degrees of Freedom”, *Computational Mechanics*, Vol. 9, pp. 417-428, 1992.

[24] Alvin, K., Horacio M. de la Fuente, Hhaugen. B. and Fellipa, C. A., “ Membrane Triangles With Corner Drilling Freedoms - I. EFF Element”, *Finite Elements in Analysis and Design*, Vol. 12, pp. 163-187, 1992.

[25] Fellipa, C. A. and Militello, C.,“ Membrane Triangles With Corner Drilling Freedoms - II. ANDES Element”, *Finite Elements in Analysis and Design*, Vol. 12, pp. 189-201, 1992.

[26] Fellipa, C. A. and Alexander, S., “ Membrane Triangles With Corner Drilling Freedoms - III. Implementation and Performance Evaluation”,*Finite Elements in Analysis and Design*, Vol. 12, pp. 203-239, 1992.

[27] Morley, L. S. D., The Constant-Moment Plate Bending Element”, *Journal of Strain Analysis*, Vol. 6, pp. 20-24, 1971.

[28] Hrabok, M. M. and Hrudey, T. M.,“A Review and Catalogue of Plate Bending Finite Elements“, *Computers and Structures*, Vol. 19, pp. 479-495, 1984.

[29] Jeyachandrabose, C. and Kirkhope, J.,“An Alternative Explicit Formulation for the DKT Plate Bending Element“, *International Journal for Numerical Methods in Engineering*, Vol. 21, pp. 1289-1293, 1985.

[30] Jeyachadrabose, C. and Kirkhope, J.,“Construction of New Efficient Three-node Triangular Thin Plate Bending Elements”, *Computers and Structures*, Vol. 23, pp. 587-603, 1986.

[31] Tessler, A., and Hughes, T. J. R., “A Three-node Mindlin Plate Element With Improved Transverse Shear”, *Computer Methods in Applied Mechanics and Engineering*, Vol. 50, pp. 71-101, 1985.

[32] Meek, J. L. and Tan, H. S., “A Discrete Kirchhoff PLate Bending Element with Loof Nodes”, *Computers and Structures*, Vol. 21, pp. 1197-1212, 1985.

[33] Gopalacharyulu, S., “A Higher Order Conforming Rectangular Plate Element”, *International Journal for Numerical Methods in Engineering*, Vol. 6, pp. 305-308, 1973.

[34] Irons, B. M., “Comment on a Higher Order Conforming Rectangular Plate Element by S. Gopalacharyulu”, *International Journal for Numerical Methods in Engineering*, Vol. 6, pp. 308-309,1973.

[35] Dhatt, G., Marcotte, L., and Matte, Y., “A New Triangular Discrete Kirchhoff Plate Shell Element”, *International Journal for Numerical Methods in Engineering*, Vol. 23, pp. 453-470, 1986.

[36] Felippa, C. A., and Bergan, P. G., “A Triangular Bending Element Based on Energy Orthogonal Free Formulation”, *Computer Methods in Applied Mechanics and Engineering*, Vol. 61, pp. 129-160, 1987.

[37] Specht, B.,“Modified Shape Functions for the Three Node Plate Bending Element Passing the Patch Test”, *International Journal for Numerical Methods in Engineering*, Vol. 26, pp. 705-715, 1988.

[38] Zienkiewicz, O. C., Taylor, R. L., Papadopoulos, P. and Onate, E.,“ Plate Bending Elements With Discrete Constraints: New Triangular Elements”, *Computers and Structures*, Vol. 35, pp. 505-522, 1990.

[39] Bathe, K. J., Ramm, E., and Wilson, E. L., "Finite Element Formulations for Large Deformation Dynamic Analysis", *International Journal for Numerical Methods in Engineering*, Vol. 9,pp. 353-386, 1975.

[40] Argyris, J. H., Dunne, P. C., Malejannakis, G. A., and Schelkle, E., "A Simple Triangular Facet Shell Element With Applications to Linear and Non-linear Equilibrium and Elastic Stability Problems", *Computer Methods in Applied Mechanics and Engineering*, Vol. 10, pp. 371-403, 1977.

[41] Horrigmoe, G., and Bergan, P. G., "Nonlinear Analysis of Free-form Shells by Flat Finite Elements", *Computer Methods in Applied Mechanics and Engineering*, Vol. 16, pp. 11-35, 1978.

[42] Chen, K. K., "A Triangular Plate Finite Element For Large-Displacement Elastic-Plastic Analysis of Automobile Structural Components", *Computers and Structures*, Vol. 10, pp. 203-215, 1979.

[43] Peric, D. and Owen, D. R. J., "The Morley Thin Shell Finite Element For Large Deformations Problems: Simplicity Versus Sophistication", *Proceedings of the International Conference on Nuclear Engineering Computations*, pp. 121-142, Swansea, Pineridge Press, 1991.

[44] Bathe, K. J., and Ho, L. W., "A Simple and Effective Element for Analysis of General Shell Structures", *Computers and Structures*, Vol. 13, pp. 673-681, 1981.

[45] Hsiao, K. M., "Nonlinear Analysis of General Shell Structures by Flat Triangular Shell Element", *Computers and Structures*, Vol. 25, pp. 665-675, 1987.

[46] Peng, X., and Crisfield, M. A., "A Consistent Co-rotational Formulation for Shells Using the Constant Stress/Constant Moment Triangle", *International Journal for Numerical Methods in Engineering*, Vol. 35, pp. 1829-1847, 1992

[47] Meek, J. L., and Tan, H. S., "Instability Analysis of Thin Plates and Arbitrary Shells Using a Faceted Shell Element With Loof Nodes", *Computer Methods in Applied Mechanics and Engineering*, Vol. 57, pp. 143-170, 1986.

[48] Poulsen, P. N, and Damkilde, L., “A Flat Triangular Shell Element With Loof Nodes”,*International Journal for Numerical Methods in Engineering*, Vol. 39, pp. 3867-3887,1996.

[49] Fafard, M., Dhatt, G., and Batoz, J. L., “A New Discrete Kirchhoff Plate/Shell Element With Updated Procedures”, *Computers and Structures*, Vol. 31, pp. 591-606,1989.

[50] Knight Jr, N. F., “The Raasch Challenge for Shell Elements”, *AIAA Journal*, Vol. 35, pp. 375-381,1997.

[51] Madenci, E., and Barut, A., “A Free Formulation-Based Flat Shell Element for Nonlinear Analysis of Thin Composite Structures, *International Journal for Numerical Methods in Engineering*, Vol. 37, pp. 3825-3842, 1994.

[52] Oral, S., and Barut, A., “A Shear-Flexible Facet Shell Element For Large Deflection and Instability Analysis”, *Computer Methods in Applied Mechanics and Engineering*, Vol. 93, pp. 415-431, 1991.

[53] Simo, J. C., and Fox., D. D., “On a Stress Resultant Geometrically Exact Shell Model. Part I. Formulation and Optimal Parametrization”, *Computer Methods in Applied Mechanics and Engineering*, Vol. 72, pp. 267-304, 1989.

[54] Parisch, H., “An Investigation of a Finite Rotation Four Node Assumed Strain Shell Element”, *International Journal for Numerical Methods in Engineering*, Vol. 21, pp. 127-150, 1991.

[55] Ibrahimbegovic, A., “Stress Resultant Geometrically Nonlinear Shell Theory with Drilling Rotations - Part I. A Consistent Formulation”, *Computer Methods in Applied Mechanics and Engineering*, Vol. 118, pp. 265-284, 1994.

[56] Surana, K. S., “Geometrically Nonlinear Formulation for the Curved Shell Elements”, *International Journal for Numerical Methods in Engineering*, Vol. 19, pp. 581-615, 1983.

[57] Brank, B., Peric, D., and Damjanic, B., “On Implementation of Non-linear Four Node Shell Element for Thin Multilayered Elastic Shells”, *Computational Mechanics*, Vol. 16, pp. 341-358, 1995.

[58] Onate, E., Zarate, F., and Flores, F., "A Simple Triangular Element for Thick and Thin Plate and Shell Analysis", *International Journal for Numerical Methods in Engineering*, Vol. 37, pp. 2569-2582, 1994.

[59] Chen, H. C., "Evaluation of Allman Triangular Membrane Element Used in General Shell Analysis", *Computers and Structures*, Vol. 43, pp. 881-887, 1992.

[60] Ertas, A., Krafcik, J. T., and Ekwaro-Osire, S., "Performance of an Anisotropic Allman/DKT 3-Node Thin Triangular Flat Shell Element", *Composites Engineering*, Vol. 2, pp. 269-280, 1992.

[61] Kapania, R. K., and Mohan, P., "Static, Free Vibration and Thermal Analysis of Composite Plates and Shells Using a Flat Triangular Shell Element", *Computational Mechanics*, Vol. 17, pp. 343-357, 1996.

[62] Mohan, P. and Kapania, R. K., "Updated Lagrangian Formulation of a Flat Triangular Element for Thin Laminated Shells", accepted for publication in the *AIAA Journal*.

[63] Mohan, P. and Kapania, R. K., "Analysis of General Shell Under Deformation Dependent Pressure Loads Using a Flat Triangular Shell Element", submitted for possible presentation at the 39th SDM conference.

[64] Kapania, R. K., Mohan, P. and Jakubowski, A., "Control of Thermal Deformation of a Spherical Mirror Segment", accepted for publication in the *AIAA Journal of Spacecraft and Rockets*, also presented at the 6th AIAA/NASA/USAF Multidisciplinary Analysis and Optimization Symposium, Bellevue, WA, 1996, (AIAA paper 96-4154).

[65] Jakubowski, A. K., Mohan, P., Kapania, R. K, Crissafulli, P., and Hammerand, D., "8-m UV/Visible/IR Space Telescope,*Proceedings of SPIE-The International Society for Optical Engineering*, Vol. 2478, pp. 20-34, 1995.

[66] Hibbitt, H. D., "Some Follower Forces and Load Stiffness", *International Journal for Numerical Methods in Engineering*, Vol. 14, pp. 937-941, 1979.

[67] Loganathan, K., Chang, S. C. and Abel, J. F., "Finite Element Representation and Pressure Stiffness in Shell Stability Analysis", *International Journal for Numerical Methods in Engineering*, Vol. 14, pp. 1413-1429, 1979.

[68] Schweizerhof, K. and Ramm, E., “Displacement Dependent Pressure Loads in Nonlinear Finite Element Analysis”, *Computers and Structures*, Vol. 18, pp. 1099-1114, 1984.

[69] Yuan, K. Y., and Liang, C. C., “Nonlinear Analysis of an Axisymmetric Shell Using Three Noded Degenerated Isoparametric Shell Elements”, *Computers and Structures*, Vol. 32, pp. 1225-1239, 1989.

[70] Iwata, K., Tsukimori, K. and Kubo, F., “Buckling Analysis of Shell Structures Under Pressure Loads Using Symmetric Load Stiffness Matrix”, *Proceedings of the ASME, Pressure Vessels and Piping Conference*, Vol. 175, pp.105-109, 1989.

[71] Malvern, L. E., *Introduction to the Mechanics of a Continuous Medium*, Prentice-Hall Inc., 1969.

[72] Gruttmann, F. and Taylor, R. L., “Theory and Finite Element Formulation of Rubberlike Membrane Shells Using Principal Stretches”, *International Journal for Numerical Methods in Engineering*, Vol. 35, pp. 1111-1126, 1992.

[73] Christensen, E. R.,“Effect of Pressure Stiffness on the Dynamics of Solid Rocket Motors”, *Journal of Guidance, Control and Dynamics*, Vol. 17, pp. 63-68, 1994.

[74] Subramanian, G. and Bose, C.J.,“Convenient Generation of Stiffness Matrices for the Family of Plane Triangular Elements”, *Computers and Structures*, Vol. 15, pp. 85-89, 1982.

[75] Jeyachandrabose, C. and Kirkhope, J., “An Alternative Explicit Formulation for the DKT Plate Bending Element”, *International Journal for Numerical Methods in Engineering*, Vol. 21, pp. 1289-1293. 1985

[76] Kleiber, M., *Incremental Finite Element Modeling in Non-linear Solid Mechanics*, J. Wiley, New York, 1989.

[77] Zienkiewicz, O. C. and Taylor, R. L., *The Finite Element Method*, 4th edition, Vol. 2, McGraw-Hill, NY, 1989.

[78] Crisfield, M. A., “A Fast Incremental/Iterative Solution Procedure that Handles Snap-Through”, *Computers and Structures*, Vol. 13, 1981, pp. 55-62.

[79] Bathe, K. J., *Finite Element Procedures in Engineering Analysis*, Prentice Hall, Inc., 1982.

[80] Bathe, K. J., Ramm, E. and Wilson, E. L., "Finite Element Formulations for Large Deformation Dynamic Analysis", *International Journal for Numerical Methods in Engineering*, Vol. 9, 1975, pp. 353-386.

[81] Phan, N. D. and Reddy, J. N., "Analysis of Laminated Composite Plates Using A Higher Order Shear Deformation Theory", *International Journal for Numerical Methods in Engineering*, vol. 21, pp. 2201-2219, 1985.

[82] Whitney, J. M. and Leissa, A. W., "Analysis of Anisotropic Heterogeneous Plates", *Journal of Applied Mechanics*, Vol. 36, pp. 261-266, 1969.

[83] Macneal, R. H. and Harder, R. L., "A Proposed Standard Set of Problems to Test Finite Element Accuracy", *Finite Elements in Analysis and Design*, Vol. 1, pp. 3-20, 1985.

[84] Reddy, J. N., "Exact Solutions of Moderately Thick Laminated She;;", *Journal of Engineering Mechanics Division of the ASCE*, Vol. 110, pp. 794-807, 1984.

[85] Kapania, R. K. and Singhvi, S., "Free Vibration Analysis of Generally Laminated Tapered Skew Plates : Enhancing Analysis Techniques For Composite Materials" ASME NDE-Vol. 10, pp. 159-168, 1991.

[86] Wu, C. H ; Tauchert, T. R. (1980): Thermoelastic Analysis of Laminated Plates. 1: Symmetric Specially Orthotropic Laminates. J. Thermal Stresses. 3, 247-259

[87] Wu, C. H and Tauchert, T. R, "Thermoelastic Analysis of Laminated Plates. 2: Antisymmetric Cross-ply and Angle-ply Laminates", *Journal of Thermal Stresses* vol. 3, pp. 365-378, 1980.

[88] Buechter, N. and Ramm, E., "Shell Theory Versus Degeneration - A Comparision in Large Rotation Finite Element Analysis", *International Journal for Numerical Methods in Engineering*, Vol. 34, 1992, pp. 39-59.

[89] Meyers, C. A. and Hyer, M. W., "Thermally-Induced, Geometrically Nonlinear Response of Symmetrically Laminated Composite Plates", *Composites Engineering*, Vol. 2, 1992, pp. 3-20.

[90] Seide, P. and Jamjoon, T. M. M., “Large Deformation of Circular Rings Under Nonuniform Pressure”, *Journal of Applied Mechanics*, Vol. 41, 1974, pp. 192-196.

[91] Robertson, H. J., Crane, R. and Hemstreet, H. S., “Active Optics System for Spaceborne Telescopes”, $NASA\ CR - 66297$, Oct. 1966.

[92] Robertson, H. J., “Development of an Active Optics Concept Using a Thin Deformable Mirror”, $NASA\ CR - 1593$, 1970.

[93] Creedon, J. F., and Lindgren, A. G., “Control of the Optical Surface of a Thin Deformable Primary Mirror with Application to an Orbiting Astronomical Observatory”, *Automatica*, Vol. 6, pp. 643-660, 1970.

[94] Howell, W. E. and Creedon, J. F., “A Technique for Designing Active Control Systems”, $NASA\ TND - 7090$, January, 1973.

[95] Ostroff, J. A., “Evaluation of Control Laws and Actuator Locations for Control Systems Applicable to Deformable Astronomical Telescope Mirrors”, $NASA\ TND - 7276$, October 1973.

[96] Scott, R. M., “New Technique for Controlling Optical Mirror Shapes”, *Optical Engineering*, Vol. 14, pp. 112-115, 1975.

[97] Bushnell, D., “Control of Surface Configurations of Nonuniformly Heated Shells”, $AIAA\ Journal$, Vol.17, pp. 78-84, 1979.

[98] Hansen, J. G. R., Richard, R. M. and Shannon, R. R., “Deformable Primary Mirror for a Space Telescope”, *Applied Optics*, Vol. 21, pp. 2620-2630, 1982.

[99] Masaki, T., Noboru, I., Keizo, M., Atsushi S., Masanori, I., Yasumasa, Y., Takeshi, N. and Wataru, T., “Shape Control Experiments with a Functional Model for Large Optical Reflectors”, First Joint U.S/Japan Conference on Adaptive Structures, Maui, Hawaii, November 13-15, 1990.

[100] Kuo, C. P., “Optimal Actuator Placement on an Active Reflector Using a Modified Simulated Annealing Technique”, First Joint U.S/Japan Conference on Adaptive Structures, Maui, Hawaii, November 13-15, 1990.

[101] Kuo, C. P., "Adaptive Optics - One Meter Deformable Composite Mirror", AIAA Paper, 91-0907-CP, presented at the 32nd AIAA Structures, Structural Dynamics and Materials Conference, Baltimore, MD, April 8-10, 1991.

[102] Kuo, C. P., "Optical Tests of an Intelligently Deformable Mirror for Space Telescope Technology", Proceedings of the SPIE - The International Society for Optical Engineering, Vol. 2040 1993, pp. 631-646.

[103] Jonnalagadda, K. D., Blandford, G. E. and Tauchert, T. R., "Piezothermoelastic Composite Plate Analysis Using First-order Shear Deformation Theory" *Computers and Structures*, Vol. 51, 1994, pp. 79-89.

[104] Tzou, H. S. and Tseng, C. I., "Distributed Dynamic Identification and Controls of Flexible Shells", AIAA paper, 90-1089, 31st AIAA Structures, Structural Dynamics and Materials Conference, Long Beach , CA, April 1990, pp. 2265-2273.

[105] Hughes, O. F., *Ship Structures Design - A Rationally Based Computer Aided Optimization Approach*, The Society of Naval Architects and Marine Engineers, New Jersey, 1988.

[106] Ha, S. K., Keilers, C. and Chang, F. K., "Finite Element Analysis of Composite Structures Containing Distributed Piezoceramic Sensors and Actuators", *AIAA Journal*, Vol. 30, pp. 772-780, 1992.

[107] Pearson, E. and Stepp, L., "Response of Large Optical Mirrors to Thermal Distributions", SPIE Vol. 748, Structural Mechanics of Optical Systems II (1987), pp. 215-228.

[108] Haftka, R. T. and Adelman, H. M., "Selection of Actuator Locations for Static Shape Control of Large Space Structures by Heuristic Integer Programming", *Computers and Structures*, Vol. 20, pp. 572-582, 1985.

# VITAE

Mohan was born in Bangalore in India. He received his bachelors degree in Mechanical Engineering from the Birla Institute of Technology and Science, India and his masters degree in Aerospace Engineering from the Indian Institute of Technology, Madras, India, specializing in computational structural mechanics. After his masters, he spent a year at IIT, Madras as a project associate, working on computational fluid dynamics. He joined the PhD program in Aerospace Engineering at Virginia Tech in January 1994 and for the last four years or so has been working on developing a flat shell element. His areas of interest are the finite element method, smart structures and inflatable structures. After his PhD he is planning to start a challenging career in computational structural mechanics.